THERMAL CONDUCTIVITY OF SOLID ARGON

Dissertation for the Degree of Ph. D.
MICHIGAN STATE UNIVERSITY
DAVID KENT CHRISTEN
1974

LIBRARY
Michigan State
University

This is to certify that the

thesis entitled

Thermal Conductivity

of

Solid Argon

presented by

David Kent Christen

has been accepted towards fulfillment
of the requirements for

Ph. D. degree in Physics

Jerrold L. Pollack
Major professor

Date May 16, 1974

O-7639

BINDING BY
HOAG & SONS'
BOOK BINDERY INC.
LIBRARY BINDERS
SPRINGPORT, MICHIGAN

ABSTRACT

THERMAL CONDUCTIVITY OF SOLID ARGON

BY

David Kent Christen

A cryogenic apparatus was designed and constructed to form large-grained, essentially free-standing samples of crystalline Argon. Subsequent in situ measurements of the thermal conductivity $\kappa(T)$ were made by a linear flow method, covering a temperature range from the triple point, 83.8 K, to liquid He temperatures. The low temperature data were highly reproducible within a single run, while the high temperature data were reproducible among different runs. The data were of sufficient density to enable quantitative analysis in terms of present theory for heat transport in insulating solids at low temperatures. In particular, we have performed first principles calculations of the anharmonic crystal force contribution to the thermal resistivity. These calculations are based upon best known interatomic potentials, including three-body corrections. They utilize a computer simulation of lattice wave interactions, as described by first order perturbation theory. The results of these calculations indicate that observed deviations from the T^{-1} temperature dependence expected of $\kappa(T)$ at high temperatures can be quantitatively explained in terms of the effects of thermal expansion on the lattice vibrational frequencies. Furthermore, $\kappa(T)$ is found to be a sensitive function of the exact functional form of the interatomic potential energy. At low temperatures, where we fit our experimental data with a relaxation time model, we discovered indications of a lattice wave scattering mechanism which, at present, is not predicted by simple models of phonon scattering by lattice defects. Manifestations

G80746

of this anomalous mechanism were evident in the data from two separate Ar samples.

THERMAL CONDUCTIVITY OF SOLID ARGON

By

David Kent Christen

A DISSERTATION

Submitted to

Michigan State University

in partial fulfillment of the requirements

for the degree of

DOCTOR OF PHILOSOPHY

Department of Physics

1974

To Sandy

ACKNOWLEDGMENTS

I would like to express my deep appreciation to Professor G.L. Pollack, who suggested this problem, for his diligent support and supervision throughout the course of this research. I would also like to thank Jon Opsal and Tom Milbrodt for the many helpful discussions and suggestions regarding the experiment.

I am indebted also to Professors T.A. Kaplan and J. Hetherington, and to Dr. W.W. Repko for valuable advise relating to the theoretical calculations, and to Mr. Michael Ford for many helpful suggestions in designing the apparatus.

Special thanks go to my wife, Sandy, for her patience and support throughout, and to Ms. Nancy Wragg for her persistent dedication to the typing of the manuscript.

Finally, I would like to acknowledge the financial support of the United States Atomic Energy Commission.

TABLE OF CONTENTS

Appendices Page

LIST OF TABLES

LIST OF FIGURES

I. INTRODUCTION

A. General Properties of Rare Gas Solids

The chemically inert gas Argon was first identified by Sir William Ramsay in 1894, resulting in the discovery of an entirely new group of elements in the periodic table. By the turn of the century the so-called rare gases Helium, Neon, Argon, Krypton, and Xenon could be separated into experimental quantities by the fractional distillation of liquid air.[1] Argon is not truely a "rare gas" since it constitutes about 1% of the atmosphere, and today it is readily attainable and relatively inexpensive. The rare gases have many commercial uses, and within the last two decades they have been recognized as valuable materials for fundamental research. When the inert gases are solidified by application of low temperatures, or in the case of He by low temperatures and high pressures, they assume a close-packed crystalline structure. This is a direct consequence of the weak, short-range, and essentially central nature of the van der Waals type interatomic forces. Because of this inherent simplicity, solidified rare gases serve as real prototype solids for which the theorist may develop microscopic descriptions of bulk properties. Unfortunately, the very nature of these solids which makes them more amenable to theoretical description results in certain physical properties which are experimentally troublesome.

Direct evidences of weak interatomic forces are a low melting temperature, high vapor and sublimation pressures, and a large ratio of

heat of fusion to heat of vaporization. This last property is a consequence of the fact that there must be a relatively large change in the total crystal energy upon melting, owing to the short-range molecular force.[2]

On solidifying a sample for experimental use, one must be concerned with some further properties. Due to the shallow potential well in which the atoms are bound, the probability of stray nucleation of crystallites is large. Thus it is difficult to obtain large, single crystals. Activation energies for various types of crystal defects are small, and the thermal expansivity very large, compounding the problem of maintaining a strain free sample. If an experimenter is to physically manipulate a solid sample, he must also contend with a soft, easily deformed specimen at low temperatures.[3,4] The rare gas solids are electrically nonconducting and optically transparent because they have closed electron subshells.

In spite of these properties, and because of them, there has been much investigation into the crystallization process of these solids, particularly Argon, and extensive study of the crystal character as a function of various growth parameters.[5-12]

B. Motivation for Heat Transport Study

At the time this research was begun, the well reviewed[2,4,13] collection of data for various rare-gas solid state properties revealed several deficiencies. In particular, the temperature dependent thermal conductivity had been measured by only three groups, with somewhat different and rather confusing results.

Thermal conductivity, $\kappa(T)$, is defined by,

$$\vec{Q} = -\kappa(T)\ \nabla T. \qquad (1)$$

In this expression $\vec{Q}$ is the energy flux associated with the thermal gradient ∇T.

White and Woods[14] made measurements for solid Ar, Kr, and Ne above 2 K. In the high T region, where their data were sparse, they observed $\kappa(T) \propto 1/T$. This T dependence was in disagreement with the later results of Krupskii and Manzhellii,[15] who observed a more rapid decline in $\kappa(T)$ with increasing T. Furthermore, White and Woods' data were much smaller at low temperatures than theory would predict. Bernè et al.[16] conducted a series of low temperature experiments for solid Ar which were as much as an order of magnitude larger. Unfortunately, their results were not well reproducible. Even in the same run, measured values sometimes differed by a factor of two.

From a knowledge of $\kappa(T)$, one can derive valuable information regarding the nature of atomic vibrations. The rate at and manner in which energy is transported from the hot to the cold end of a dielectric solid is determined solely by the way in which the lattice vibrational waves interact with one another, and with impurities, various types of defects, and the sample boundaries. In various temperature ranges, usually taken relative to the Debye temperature, it is often true that $\kappa(T)$ displays a T dependence indicative of a particular type of lattic wave scattering mechanism. Thus, $\kappa(T)$ is a sensitive indicator of interatomic force anharmonicity, as well as crystal perfection and purity.

C. Thermal Conductivity

The mechanism for heat conduction in an insulator can be understood in two ways. One way, the singe particle approach, considers a single atom and analyzes its motion as governed by that of all the rest.[17] The other way, which we will employ here, considers the collective normal mode oscillations of the entire solid. These are quantized and regarded as a system of excitations call phonons. In this latter view, if the interatomic forces of a perfect and infinite crystal are purely harmonic (i.e., bilinear in atomic displacements from the equilibrium), then there is no energy transfer between normal mode waves, and energy would flow unattenuated at approximately the speed of sound. A real solid, however, is considered to be a system of interacting phonons of finite lifetime. For this model one may obtain an expression for the thermal conductivity which is analogous to that of a classical gas.[18]

$$\kappa(T) = 1/3\ C_v\ v\ \ell. \qquad (2)$$

Here ℓ is the phonon mean free path, C_v the specific heat at constant volume, and v some average phonon velocity. Although not strictly accurate in general, this simple relation explains some qualitative features of $\kappa(T)$.

For temperatures greater than or comparable to the Debye temperature, the dominant phonon scattering mechanism is the so-called Umklapp type phonon-phonon interaction described by Peierls.[19] This interaction is due entirely to the anharmonic terms which result when one expands the crystal potential in a Taylor series of small atomic displacements from equilibrium. To lowest order, this effect predicts a three-phonon process mean free path proportional to 1/T, with a magnitude determined by the scattering strength.

In the opposite limit, at very low temperatures, phonon-phonon scattering is negligible and the mean free path in a perfect, but finite, sample is determined by its size. In this case, phonons propagate unattenuated to the surface, where they are considered to be absorbed and re-emitted. Therefore, ℓ is temperature independent and $\kappa(T)$ varies as the specific heat, $\kappa(T) \propto T^3$. For samples of lesser quality $\kappa(T)$ may display a T dependence characteristic of some type of strong defect or impurity scattering. If, for such a process, $\ell \propto T^{-n}$, then $\kappa(T) \propto T^{3-n}$. For example, $\ell \propto T^{-1}$ for scattering due to dislocations, in which case $\kappa(T) \propto T^2$.

D. Purpose

In the present thesis, we prepared samples of solid Ar under controlled crystal growth conditions, and made subsequent in situ measurements of $\kappa(T)$ from approximately 2 K to the triple point (83.8 K). Argon was the material chosen to be studied for the following reasons: A triple point temperature of 83.8 K enables one to employ the inexpensive cryogen liquid Nitrogen (boiling point 77.3 K) during the prolonged periods of sample solidifications. The natural Argon gas obtained by fractional distillation of air is relatively inexpensive and very pure (the research grade Ar used for these experiments contained a total impurity content of less than 10ppm). Normal Ar is nearly isotopically pure. The isotope Ar^{40} constitutes 99.6%, the remaining isotopes being Ar^{36} and Ar^{38}. Thus, the concern for mass defect phonon scattering is minimized. The interatomic potential for Ar, corrected for three-body forces, is the best known of all the rare gases, as displayed by its ability to predict accurately several solid state, liquid, gas properties.[21,22]

This provides a more meaningful comparison to current theoretical models for heat transport.

The data obtained from these experiments are compared to results given by various semi-quantitative models for phonon scattering. In addition, we have performed first principles calculations of the three-phonon anharmonic contribution to the thermal resistivity. The normal mode frequencies and anharmonic coupling constants for an fcc lattice are computed using the best known interatomic potential,[21] as well as the well-known Mie--Lennard-Jones 6-12 potential. The results are compared with the present data as well as data which became available during the course of this work.[23]

II. THE EXPERIMENT

A. Cryogenic Apparatus

To facilitate the solid Ar sample preparation and subsequent *in situ* thermal conductivity measurements, a cryogenic apparatus was designed and constructed. This device mounted in a conventional double dewar system to enable cooling by either liquid N_2 or liquid He bath. A non-scale, sectional view of the cryostat sample chamber is shown in Figure 1.

1. Description of Apparatus

The outermost glass-walled exchange gas chamber facilitated a coarse temperature control by means of a variable He gas pressure. The He exchange gas admitted to this chamber served to transport heat from the sample into the surrounding cryogen at a rate which could be somewhat controlled by the gas pressure. Stranded Cu braid, soldered into the upper Cu flange, aided this process by providing a large effective area exposed to the He gas. The exchange gas was admitted directly from a source gas cylinder via a pressure regulator and needle valve. Its pressure was monitored by two Wallace and Tiernan mechanical gauges for pressures above 1 Torr, and by a Veeco thermo-couple gauge for pressures below 1 Torr.

The glass-walled vacuum chamber contained 1 Torr He exchange gas during the crystal growth stages of the experiment, and was evacuated during thermal conductivity measurements. A vacuum of about 10^{-7} Torr, as measured by a cold cathode ionization gauge, could be maintained in

Figure 1: A diagram of the cyrostat sample chamber.

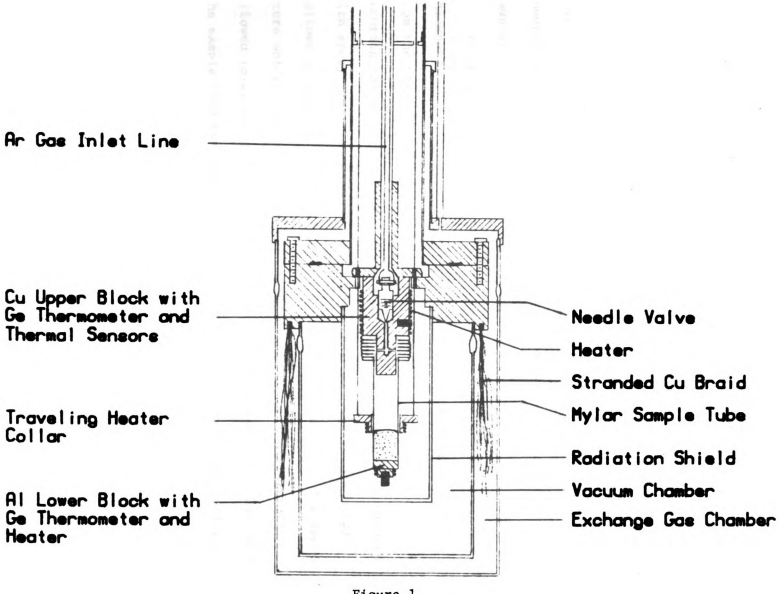
Ar Gas Inlet Line
Cu Upper Block with Ge Thermometer and Thermal Sensors
Traveling Heater Collar
Al Lower Block with Ge Thermometer and Heater
Needle Valve
Heater
Stranded Cu Braid
Mylar Sample Tube
Radiation Shield
Vacuum Chamber
Exchange Gas Chamber

Figure 1

the vacuum chamber by means of a pumping station. This station consisted of an oil diffusion pump with liquid N_2 cold trap, a rotary backing pump, and a rotary roughing pump.

The Cu radiation shield shown in Figure 1 served to prevent excessive radiative transfer of heat from the Ar sample to the bath. Although negligible at all but the highest temperatures, this effect could cause errors in the measured thermal conductivity at temperatures near the Ar melting temperature. The Cu shield contained narrow slits covered with transparent Mylar to facilitate visual examination of the sample.

The Ar sample tube itself was fabricated from sheet Mylar of 0.005" thickness. We formed a cylindrical tube, of diameter approximately 1 cm, from the Mylar sheet by wrapping it around a solid Teflon mandrel, and securing the seam with epoxy. This thin-walled tube was then cemented with epoxy into a small Al block at the lower end, and into a metal bellows at the top. The metal bellows was soldered with the low temperature solder, Cerro-bend, to the upper Cu block. This configuration allowed relative vertical motion between the fixed upper Cu block and the sample tube by means of expansion and contraction of the bellows.

The high purity Ar gas used to condense a crystal was admitted to the sample tube through stainless steel gas-handling lines. A Wallace and Tiernan pressure gauge served to monitor its pressure. The gas source was a steel cylinder equipped with pressure regulator and needle valve for flow control. All gas samples were derived from the same tank of Matheson research grade Argon. Mass spectrometer analyses provided with the source tank indicated a total of less then 10 ppm impurity content, with the principle impurities being O_2--3.0 ppm,

H_2O--3.5 ppm, and N_2--2.0 ppm.

Wherever possible, stainless steel was used in this gas circuit because of the relatively low binding energy of gases to stainless steel.[24] This alleviated the problem of sample contamination from outgassing of adsorbed air. Conventional copper pipes served for all other gas handling lines.

When not in use, the Ar gas circuit was kept either at a slight over pressure, or completely evacuated. Before each run, we alternately evacuated and flushed the system with fresh Ar gas.

2. Temperature Measurement

It was necessary to know precisely the temperature of the Argon sample during crystal solidification and for thermal conductivity measurements. For this purpose, calibrated Scientific Instruments Inc. intrinsic Ge resistance thermometers were imbedded in drilled cavities in the upper and lower blocks, and were firmly secured there with vacuum grease. In addition, uncalibrated Ge and Pt thermal sensors occupied cavities in the upper block. These sensors provided indication of thermal changes for the purpose of temperature control.

A Leeds and Northrup K-5 potentiometer was used to measure the electrical resistance of these thermometers, and thus provide the temperature. A four-lead configuration was used for each thermometer--two leads carried a known excitation current of 100 μamps (for $T \gtrsim 5$ K) or 10 μamps ($T \lesssim 5$ K), and the remaining two leads were run to the potentiometer to measure the resulting potential drop across the thermometer. To compensate for possible thermal e.m.f.'s along the leads, all measurements were repeated with the excitation current reversed, and the two results were averaged. Figure 2 is a schematic representation of this layout, including the circuitry for the lower block heater.

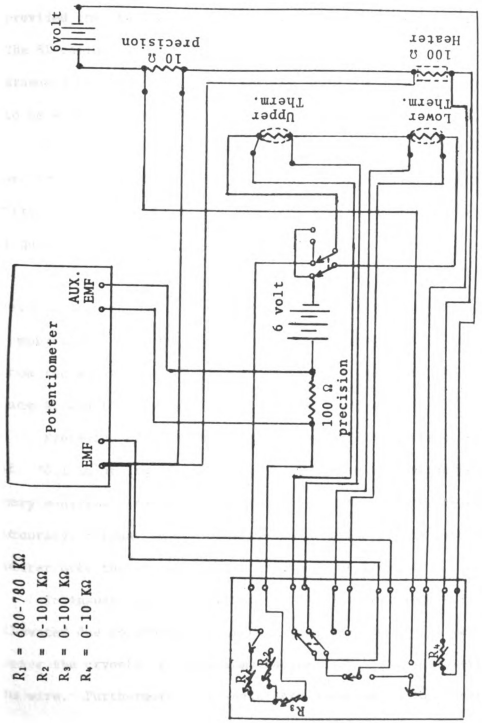

Figure 2: A schematic diagram of the thermometer and lower block heater circuits.

Calibration of the lower Ge thermometer from 1.5 K to 100 K was provided in table form by Scientific Instruments, and that thermometer provided the standard to which we calibrated the upper thermometer. The SI calibration was performed against a secondary N.B.S. Ge standard thermometer. Repeatability after thermal cycling was reputed to be within 0.5 mK.

To facilitate temperature interpolation between the 5 K intervals provided in the SI calibration table, we made least squares splined fits to the calibration data over the entire temperature range. Using a quadratic relation of the form,

$$T^{-1} = a_0 + a_1 \ln R + a_2 (\ln R)^2,$$

sets of constants a_0, a_1, and a_2 were determined for over-lapping temperature intervals of about 15 K. All temperatures were then computed from the above equation by substituting the measured thermometer resistance R, and the appropriate set of constants.

Precision of the temperature determinations varied from a deviation of ± 0.1 mK at liquid He temperatures, where the Ge thermometers are very sensitive, to one of about ± 3.5 mK at 80 K. We estimate the total accuracy, accounting for possible calibration errors, to be $\pm 0.001T$ or better over the entire temperature range of interest.

To insure that the thermometer temperatures were not falsely elevated due to conduction of heat down the electrical leads, which leave the cryostat at room temperature, all leads used were #36 gauge Cu wire. Furthermore, the leads were anchored to the upper block as a heat sink. This was accomplished by wrapping the leads around the upper block many times and coating them with varnish.

3. Temperature Control

During sample solidification (a process which generally extended over a period of about three days) and especially during thermal conductivity measurements, it was necessary to maintain the Ar sample at a fixed temperature. This was accomplished in three related ways: First, by pumping on the cryogenic liquid in the dewar vessel (the bath temperature is determined by its vapor pressure). Second, by judiciously adjusting the He exchange gas pressure in the exchange gas chamber. Third, by the use of a sensitive electronic temperature controller in order to balance heat loss to the bath with joule heat input.

For temperatures in the range 63-77 K, regulation of liquid N_2 vapor pressure provided reasonable stability. This was accomplished very simply by pumping with a mechanical vacuum pump through a manostat type pressure regulator. Bath pressures were monitored by a Hg manometer. In most cases, the manostat could maintain the liquid N_2 bath pressure within ± 0.1 Torr, providing temperature control to ± 0.02 K.

In a similar manner, vapor pressure regulation of a liquid He bath provided temperatures below 4.2 K. At the lowest temperatures, liquid He was condensed directly into the exchange gas chamber, and pumped to as low a pressure as possible by a large capacity mechanical pump.

In the temperature range between 4.2K and 63K, where there is no convenient cryogen, we employed a liquid He bath. With the exchange gas chamber nearly evacuated, the sample temperature was maintained constant by the temperature controller. In all cases, the sample temperature was kept marginally higher than the surrounding, with the electronic device providing the necessary power to offset the thermal losses. This procedure was found to give finest temperature control.

The temperature controller, model 3610, used for this experiment was manufactured by Scientific Instruments. Its principle of operation is straightforward. An internal 1 kHz oscillator drives an ac Wheatstone resistance bridge, one leg of which is either the negative temperature coefficient Ge sensor, or the positive temperature coefficient Pt sensor, which is imbedded in the upper Cu block. During the bridge balance condition (thermal equilibrium), the sensor resistance equals that of the bridge's other leg, which consists of a six decade (0-9999.99Ω) precision variable resistor. If the temperature of the upper block deviates from that desired, the bridge is out of balance, with its output signal being either in or out of phase with the oscillator signal, depending on whether the temperature deviation of the sensor is above or below the set point value. This out-of-balance signal is then amplified and phase analyzed relative to the oscillator signal. The difference in phase is used to produce a dc voltage which is amplified to control the power output to the external heater wire wound onto the upper block. Thus the power restoring the block to thermal equilibrium is proportional to the deviation from the set point. Slight modification of the bridge circuit and output stage were made for our application.

In practice, short term control of about ±0.01 K was maintained during crystal growth, with overnight stability to within ±0.1 K. During low temperature measurements, attended use of the controller resulted in deviations of less than ±1 mK.

B. Sample Preparation

1. Crystal Growth Technique

The technique used to crystallize an Ar sample was similar to that employed by other workers.[7,10,11] Argon gas is condensed to the liquid phase, and then slowly solidified by preferentially cooling below the triple point. The procedure is a modified Bridgman technique, i.e. the sample directionally solidifies from the bottom to the top. This technique was chosen because it has been verified that large grain sizes are obtained in this way, as opposed to direct solidification from the vapor, for example.[5,7]

The evacuated Mylar sample tube was maintained at about 84 K, just above the Ar triple point temperature, 83.8 K, by using: 1 Torr He exchange gas in the vacuum chamber, several Torr in the exchange gas chamber, 1 atm. of gaseous He in the inner dewar, and liquid N_2 in the outer dewar. Even though all the temperature control occurs at the upper Cu block, essentially no thermal gradients were present along the sample tube. This was due to the presence of the stabilizing He exchange gas and the fact that the good thermally conducting Cu shield defined essentially a thermal equipotential.

Argon gas was then admitted to the sample tube via the stainless steel inlet line and the capillary channel through the upper block. At a pressure of about 600 Torr (Ar triple point pressure = 516.8 Torr), the Ar would freely condense to the liquid. This process was continued for about fifteen minutes until the sample tube was full of liquid Ar at 84 K.

At this stage, the needle valve in the upper block was closed, and preparation made to employ the moveable heater collar shown in Figure 1.

The collar's i.d. was slightly larger than the tube, and it was wound with 100 Ω of #36 gauge CuNi heater wire. The collar was suspended from above by two cotton threads which served to hoist it vertically at a fixed rate. This rate was determined by a 2 rpm synchronous motor in conjunction with a gear box of adjustable ratio. The driving mechanism was situated on a platform outside and above the cryostat.

In the next stage of sample preparation, the collar was positioned 2-3 mm above the top of the lower block and supplied with a heat input of about 10 mwatt. The temperature controller set point was then slowly decreased until solid began to form on the lower block. A solid layer slowly grew to a thickness of about 0.5 mm, at which level the liquid Ar was locally maintained at a temperature above 83.8 K by the heater collar. Curiously, solid did not form for quite a distance above the collar, even though the upper block and surroundings were below the triple point. We surmised this phenomenon must have been due to warm exchange gas convection currents rising upwards from the collar.

In this static situation, the seed of solid Ar on the lower block was allowed to anneal for a period of 12-24 hrs. at a temperature just below the triple point. In this manner, presumably the larger crystallites would grow to absorb the smaller ones, until a lowest energy configuration would result. Then a single crystal orientation would be present at the solid-liquid interface.

To initiate crystal growth from the existing seed, the motor drive was activated and the heater collar hoisted at the rate of 0.7 mm/hr. The liquid-solid interface would slightly trail the bottom of the collar, with the solid surface slightly convex. Besides totally determining the rate of growth, the heater collar served another important purpose.

Since the thermal conductivity of Mylar (or almost any substance which could conceivably be used as a sample tube) is larger than that of solid Ar near its triple point, the heat of fusion could be conducted away more rapidly through the sample tube walls than through the existing solid. Thus, crystallites would tend to nucleate on the sample tube walls, creating new grains and a polycrystalline sample. Under these conditions, one would observe the solid surface to be concave toward the liquid. This problem is compounded by the fact that the nucleation probability for Ar is relatively larger than that of other substances. See Appendix A. By keeping the walls of the Mylar sample tube slightly warm in the vicinity of the interface, the heater collar alleviated this problem.

The slow growth rate of 0.7 mm/hr. was a practical consideration based upon previous study. It has been found, for example, that grain size is roughly inversely proportional to growth rate.[6] Apparently, a significant amount of surface migration and annealing can occur at rates this slow, and this is some indication that the crystal impurity content is substantially reduced by the zone refining effect of slow directional solidification.[28]

The solidification procedure was continued for the length of the sample tube, about 3 cm. As the solid neared the upper end it was necessary to stop the heater collar and condense more liquid, since at that stage the liquid level was below the bottom of the upper block. This drop in liquid level had occurred continuously during the growth process, and could be related quantitatively to the difference in liquid and solid density; ($\rho_s / \rho_\ell \simeq 1.15$). The remaining liquid Ar was then slowly frozen into contact with the upper block, and the entire sample left to anneal over night at about 82-83 K.

During this entire solidification process, all vacuum pumps and unnecessary mechanical devices were shut down to reduce vibrations, and avoid their possibly deleterious effects upon sample quality.

There has been some indication that a metastable hcp crystal structure can occur in solid Argon, especially when the impurity content is high or the growth rate fast.[6,25] In fact, the simplest and most straightforward interatomic potential functions theoretically predict hcp to be the slightly more energetically favorable structure, despite X-ray confirmation of an fcc lattice.[7] One can simply check for the possibility of hcp domains by testing for optical birefringence. This test was made for several samples using a white light source and two polarizing filters. In all cases, the samples were observed to produce sharp extinctions at 90^{o} crossed filter positions only, implying optical isotropy and hence a cubic structure.

2. Sample Manipulation

With the Ar completely solidified and at 80-82 K, we opened the upper block needle valve and reduced the Ar supply pressure slightly in order to sublime away the excess solid condensed in the inlet lines and in the convolutions of the bellows. This was effected by intermittently reducing the supply gas pressure to about 10 Torr below the equilibrium vapor pressure. By visual examination, it was apparent when solid would begin to disappear from around the sides of the portion of the upper block which protruded into the sample tube. At that time, the sublimation process was stopped, and the needle valve again closed.

At that stage, one of three approaches was taken: (i) Thermal conductivity measurements were initiated and conducted only over the Liquid N_2 temperature range from about 83-64 K. (ii) The crystal was

"sacrificed" in order to study its grain size by large scale sublimation of its surface. (iii) Tedious and careful cool-down procedures were begun to enable low temperature thermal conductivity measurements on essentially free-standing samples.

Procedures (ii) and (iii) are described presently, while (i) will be detailed in section C.

It has been recognized that many gross crystal characteristics, in particular grain size and number, can be studied, without resort to X-ray examination, by the method of thermal etching. Rare gas solids are particularly well-suited for this technique because of their large sublimation pressures. In this process, atoms which are on highly disordered sights tend to evaporate preferentially due to their relatively weaker binding energy. In addition, grain boundary self-diffusion activation energies are typically a factor of two less than those for the bulk, so that rapid mass diffusion along the boundaries and onto the adjoining crystal surfaces occurs. This creates a lower surface free energy at the expense of mass within the grain boundaries.[29] The resulting mass defective regions then appear as etch lines on the sample surface.

At temperatures about 82 K the equilibrium sublimation pressure of solid Ar is well above half an atmosphere. By slowly reducing the pressure over the solid Ar sample by about 10 Torr, we could effect a rather rapid sublimation process which revealed the resulting etch lines described above.

At first the solid could be seen to detach itself from the Mylar growing tube progressively from top to bottom. Once detached, further sublimating resulted in the etch patterns. In all cases the observed

grains were quite large, with from three to seven grains apparently comprising the entire sample. This estimate could be made fairly reliably since the grain boundary lines could often be visibly followed completely around the sample due to its optical transparency. On two separate occasions, we successively removed layer after layer of solid by extended sublimation. In this way the grain boundaries were traced in their progression through the solid. Extremely rapid pumping resulted in several other types of surface features which have been extensively studied and documented.[5,6] In particular, surface decoration "rosettes" appeared upon very rapid sublimation, and propagated into the solid, forming gross defects. Macroscopic void-like defects of a similar nature also could be produced by sudden and rapid cooling. The two effects are probably related since rapid pumping over the sample must cool the surface quickly due to the heat of sublimation; thus the strains produced in both cases are of a common origin.

To utilize a sample for low temperature thermal conductivity studies, it was necessary to slowly cool the solid from its triple point to liquid He temperatures. Ideally this must be done without inducing unnecessary elastic strain, and without permitting the ends of the crystal to lose intimate contact with the upper and lower blocks, which served as the heat source and sink during thermal conductivity measurements. Unfortunately, solid Ar undergoes a volume contraction of almost 9% when cooled to liquid He temperatures (this is about nine times that of Cu, for example, when cooled from room temperatures). Since the Mylar sample tube contracts at less than half this rate, one expects that the Ar would contract in length about 1 mm more than the Mylar during cool-down. This, coupled with the fact that solid Ar is rather plastic near

its triple point, poses the additional problem of plastic deformation due to the constraints of the sample tube. To alleviate this latter problem, we attempted to keep the sample slightly separated from the growing tube by a sublimation process similar to that described in the previous section.

The metal bellows, which were positioned such as to allow relative vertical motion between the sample tube and the upper block, served the important function of preventing separation of the Ar sample from either the upper or lower blocks. This was accomplished in the following way: The number of convolutions was chosen such that the bellows possessed a characteristic spring rate. This rate was such that an internal pressure of magnitude approximately equal to the triple point Ar vapor pressure resulted in bellows expansion of at least 1 mm. Thus, the solid initially was formed under conditions of bellows expansion. With decreasing temperature, the rate of solid Ar thermal contraction is slower than that of the vapor pressure drop (which is, in fact, exponential). Therefore, there was always some net spring tension applied to the surface of the Ar sample due to the bellows. Some detailed features regarding the effect on the sample of this aspect of the cool-down procedure are given in Appendix B.

With the sample pre-cooled to 78 K, we began the cool-down procedure by transferring liquid He into the inner dewar immediately after evacuating the exchange gas chamber to a pressure of only a few microns. With liquid He in the inner dewar, the He exchange gas chamber pressure was undetectable (less than 1 micron), owing to cooling and to adsorption of the cold chamber walls. Nevertheless, enough thermal contact was present to necessitate power input from the temperature controller. The

He gas pressure of 1 Torr which was present in the vacuum chamber before the transfer, dropped to a value of about 100 microns with the He bath present. We observed the lower block temperature to slowly decrease to about 0.2 K below that of the upper block, indicating the presence of a small temperature gradient along the sample length. This gradient, which was due to the large temperature differential from sample to bath, could be removed by supplying a small current to the lower heater, or by reducing the He gas pressure in the vacuum chamber; however, a slight gradient proved to be desirable since it discouraged vapor phase mass migration to the upper block and bellows dead volume.

Cooling from this point on could be achieved in principle by a steady reduction in the temperature controller set point. During the earlier stages of this research, this operation was carried out manually. It soon became apparent, however, that this procedure was prohibitively tedious, and we were plagued by thermal instabilities which developed as the liquid He bath level fell. These instabilities were due to changing thermal loads induced by desorption of He gas from the chamber walls. In addition, upon re-transferring liquid He, we would unavoidably warm the sample somewhat by the initial flow of warm He gas from the transfer tube. The Ar sample would not tolerate these rapid temperature fluctuations, as was immediately apparent by a generally cloudy appearance, and ultimately by a very low value of the measured thermal conductivity, indicative of a highly defected solid.

For the most part, these problems were remedied by modifying the apparatus geometry, and by carefully pre-cooling the He transfer tube before each transfer. In addition, we automated the cool-down procedure by devising a motor driven potentiometer which would decrease the

temperature controller set point at a predetermined rate. The same synchronous motor and gear assembly used for crystal growth was made to drive a 0-25Ω ten-turn precision potentiometer which we shunted across the control arm of the temperature controller bridge internally. In this way, precise cooling rates of about 1 K/hr. could be steadily maintained.

The cooling rate of 1 K/hr. was representative of what we found to be a practical upper limit in order not to severly strain the sample due to differential thermal contraction. In the course of this work, it became apparent that a reasonable criterion for the strain condition of the sample was its optical clarity. Several specimens became milky in appearance at temperatures from 30-50 K, and in all these cases displayed low thermal conductivity values at liquid He temperatures. In spite of our attempts, we were unable to obtain a sample that did not possess at least some surface defects at low temperatures. Visual inspection of these solids indicated, however, that the visible defects were confined to the surface, and were probably due to strains produced by surface bridging to, and subsequent contraction from, the specimen tube wall.

C. Thermal Conductivity Measurement

To conduct thermal conductivity measurements on a solid Ar sample, we first evacuated the vacuum chamber to as low a pressure as possible, while retaining only enough He exchange gas in the exchange gas chamber to facilitate accurate temperature control. At liquid He temperatures the vacuum chamber pressure was typically $1X10^{-7}$ Torr, and at Liquid N_2 temperatures it was about $2\text{-}3X10^{-7}$ Torr.

Measurements were made by first allowing the lower end of the sample to thermally equilibrate with the temperature-controlled upper end.

Barring inherent heat leaks to or from the lower block, the sample temperature would eventually become constant. We then recorded the temperature of the lower block. Maintaining the upper block at the same fixed temperature, a known rate of joule heat was put into the 100Ω lower block heater. This heater possessed a four-lead configuration so we could make electrically unperturbed measurements of the voltage drop across it by means of the L & N K-5 potentiometer. The heater current was measured by making a potentiometric measurement of the voltage across a precision 10Ω resistor wired in series with the heater (See Figure 2). Knowing both the voltage across and current through the heater, we could accurately compute the heat input, $\dot{Q} = I \cdot V$, to the lower end of the sample. After a sufficient time, a condition of steady state heat flow was reached whereby the lower end of the sample was at some temperature ΔT higher than that of the upper end. Measuring the new lower block temperature, we could then compute the thermal conductivity, which is given by,

$$\kappa(T) = \dot{Q}\ (L/A)/\Delta T. \qquad (3)$$

In Equation 3, L/A is a geometric factor equal to the ratio of length to the cross-sectional area of the sample.

The sample length L was measured optically with a Wild cathetometer, while the cross-sectional area A was taken to be that of the Mylar sample tube, appropriately corrected for thermal contraction. We calculated the temperature differential ΔT using the analytical representation of the calibration table described in section A.2.

It should be noted that the technique described above for determining the thermal gradient requires precise calibration of only one thermometer--the one mounted in the lower block. Temperature sensors

in the upper block need only indicate thermal changes, in order to facilitate keeping the upper block temperature constant during the course of the two-step measurement procedure.

For fixed sample geometry, the size of the temperature differential ΔT is, of course, determined by the thermal conductivity $\kappa(T)$ and the rate of heat input $\dot{Q}$. If one applies only a small rate of heat, the errors in the measurement of ΔT will be correspondingly larger since this quantity is itself a small difference between two relatively large numbers (i.e. the difference between the initial and final absolute temperatures of the lower block). On the other hand, a large $\dot{Q}$ and ΔT, which can be accurately measured, may cause errors in $\kappa(T)$ in two ways. First, the pointwise, linear nature of Equation 1 may not be valid due to the size of ∇T; in this case, the inclusion of higher order terms in ∇T would be necessary. This problem is of fundamental origin, and will be discussed in Section IV. Second, if $\kappa(T)$ is a rapidly varying function, its variation over the length of the sample can cause errors in the effective value given by Equation 3, which is assumed to be evaluated at the average temperature of the sample. This problem is discussed quantitatively in Appendix C.

In any case, we tested the severity of this problem by determining the thermal conductivity at a given temperature for several different heat rate inputs. We observed no systematic dependence of $\kappa(T)$ on ΔT, and the resulting deviations were within the estimated experimental error.

Some representative values of the temperature gradients used for these studies range from about 3 mK/cm at the lowest temperatures to about 67 mK/cm near the triple point. A possible correction to Equation 3 may be necessary in the value of the heat rate $\dot{Q}$ in order to

compensate for heat transport from the lower block by means other than the Ar sample. Possible sources of such a spurious heat loss might be: (i) Thermal conduction of the walls of the Mylar sample tube. (ii) Conduction of the residual gas in the vacuum chamber. (iii) Radiation from sample to surroundings. (iv) Thermal conduction of the electrical leads from lower to upper block.

A non-trivial contribution from any of these mechanisms would result in a falsely elevated value of the measured thermal conductivity. In the liquid He temperature range, we ascertained that an upper limit to this error was about 0.3%. This result was derived from a direct measurement made during an unsuccessful run in which the Ar sample pulled away from the heat sink. The anomalously small measured thermal conductivity was apparently due to the parallel conductors listed above plus whatever small contribution the sample made. That this is true was verified by an observed fifty fold increase in the thermal conductivity after admitting 5 Torr of He gas to the sample tube.

Approximate calculation indicated that (iv) about could necessitate a correction of at least 10% in the high T range, while the other three effects were found to be negligible. It was difficult to measure this stray conductance directly, however, because of the extremely long thermal relaxation time at high temperatures. Our procedure, therefore, was to measure the time dependence of the thermal relaxation and from it infer the contribution of the lead conductance. We give a description of the principle and technique in Appendix D.

III. EXPERIMENTAL RESULTS

A. Data

In all, thermal conductivity measurements were carried out on seven separate solid Ar samples. The data obtained were highly reproducible within a single run, as was verified by sweeping through the temperature range 2-10 K several times with each sample used for low T measurements. This procedure was feasible at low temperatures since thermal relaxation times were short, and measurements could be made within a matter of minutes.

The experimental data are given in Table 1, and in Figure 3 we present a plot of our unsmoothed data, illustrating the temperature dependence of the thermal conductivity for the seven Ar samples. Figures 4 and 5 are similar graphs, including the results of other workers.[14-16,23,48] The data of Krupskii and Manzhelii (K-M),[15] shown in smoothed form, were obtained using an experimental geometry and growth technique similar to ours. Their specimens were probably very polycrystalline, however, since they had no provision for inhibiting stray nucleation on the glass growing tube walls during crystallization. Furthermore, at the lower temperatures they relied upon He gas within the sample tube to provide heat contact between the sample and the thermal sink or source, since the latter objects were spatially fixed and could not compensate for specimen contraction. This series thermal resistance was not accounted for and could conceivably cause errors in the computed sample thermal conductivity.

TABLE 1

Experimental Thermal Conductivity Data

T(K)	κ(T) (mw/cm K)	T(K)	κ(T) (mw/cm K)
	Runs 2, 3, 4, 5		
65.72	4.51	75.62	3.78
68.26	4.43	80.50	3.00
70.77	4.07	82.42	2.73
		82.40	1.89
	Run 7		
8.07	88.51	9.96	65.93
8.95	77.43	10.90	54.67
9.93	65.45	13.57	34.29
	Run 8		
3.12	28.17	5.17	60.89
3.24	29.58	5.26	58.78
3.25	29.58	5.27	59.19
3.37	31.55	5.35	58.71
3.48	32.92	5.50	59.75
3.53	33.63	5.57	61.01
3.56	34.01	5.58	62.70
3.64	34.72	5.69	62.12
3.84	38.17	5.84	63.99
4.04	41.10	5.85	64.38
4.20	43.92	5.85	62.52
4.23	44.98	5.86	61.11
4.40	49.76	5.98	65.55
4.41	47.09	6.01	64.98
4.50	47.77	6.07	71.78
4.58	49.07	6.08	63.92
4.59	49.87	6.12	65.58
4.65	49.34	6.15	63.71
4.72	50.56	6.27	63.94
4.72	48.62	6.41	64.49
4.76	52.24	6.55	65.74
4.81	56.02	6.56	64.27
4.87	53.07	6.60	64.13
4.87	53.08	6.69	64.21

TABLE 1 (cont'd)

T(K)	κ(T) (mw/cm K)	T(K)	κ(T) (mw/cm K)
	Run 8		
4.88	52.43	6.81	63.89
4.94	56.90	6.82	63.65
4.99	56.25	6.84	64.82
5.00	54.75	6.96	63.09
5.13	57.82	7.06	63.70
7.12	63.31	11.27	39.12
7.21	62.81	12.13	34.90
7.51	60.76	15.08	31.60
7.91	57.97	16.92	23.68
7.93	57.37	20.16	18.32
8.03	60.87	24.69	15.19
9.05	52.35	44.35	6.92
9.61	47.78	65.43	4.23
10.17	44.10	77.74	2.99
		81.93	2.28
	Run 10		
2.12	19.83	5.68	73.69
2.22	20.90	5.98	75.79
2.49	23.91	6.00	75.74
2.62	27.43	6.02	76.58
2.85	30.15	6.31	75.06
3.03	33.82	6.72	72.57
3.33	37.23	7.33	69.32
3.95	50.30	7.51	68.08
4.49	57.79	8.86	53.99
4.92	63.81	10.82	43.95
5.21	70.64	13.41	31.03

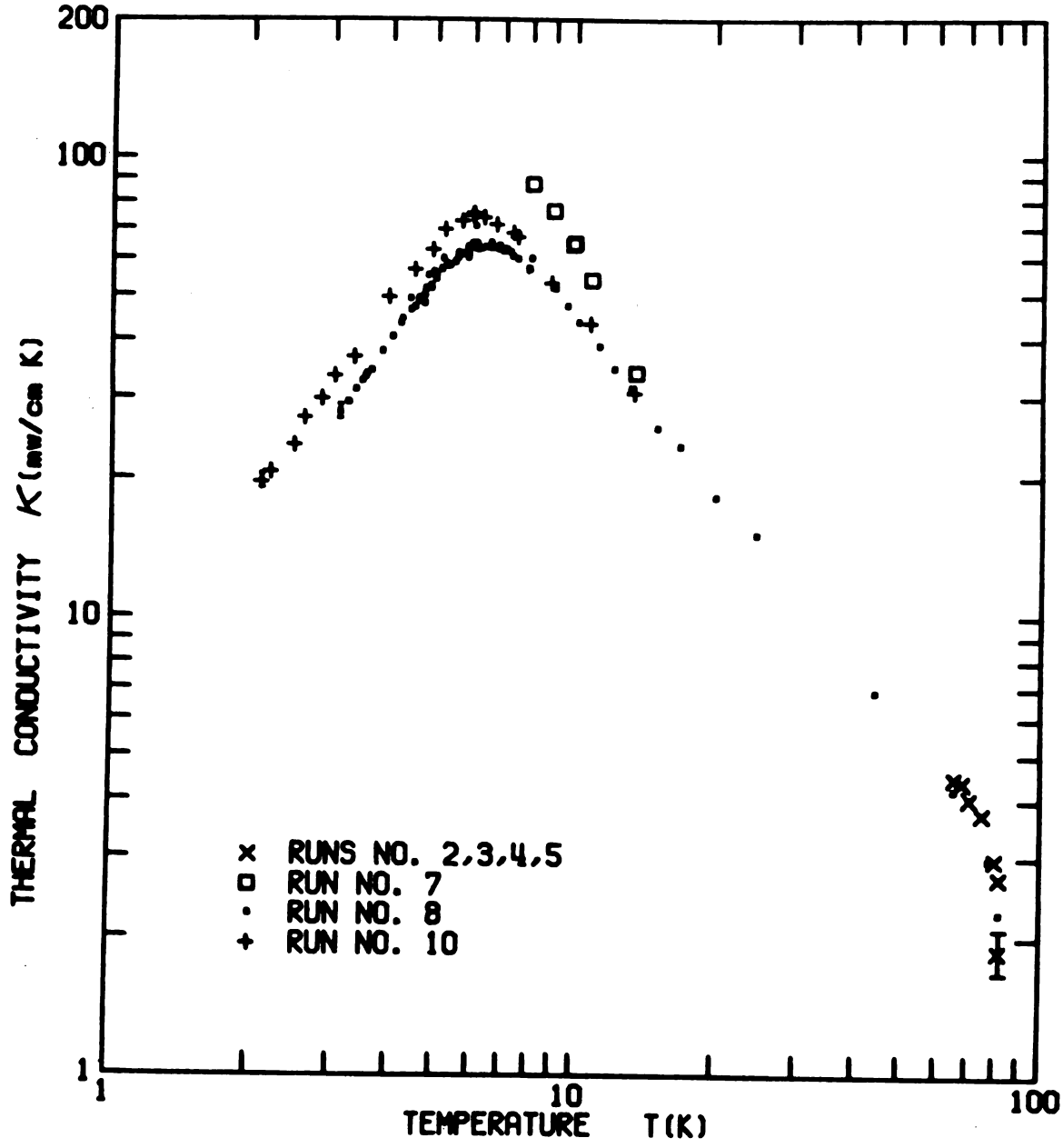

Figure 3: A plot of $\kappa(T)$ vs T for the present data.

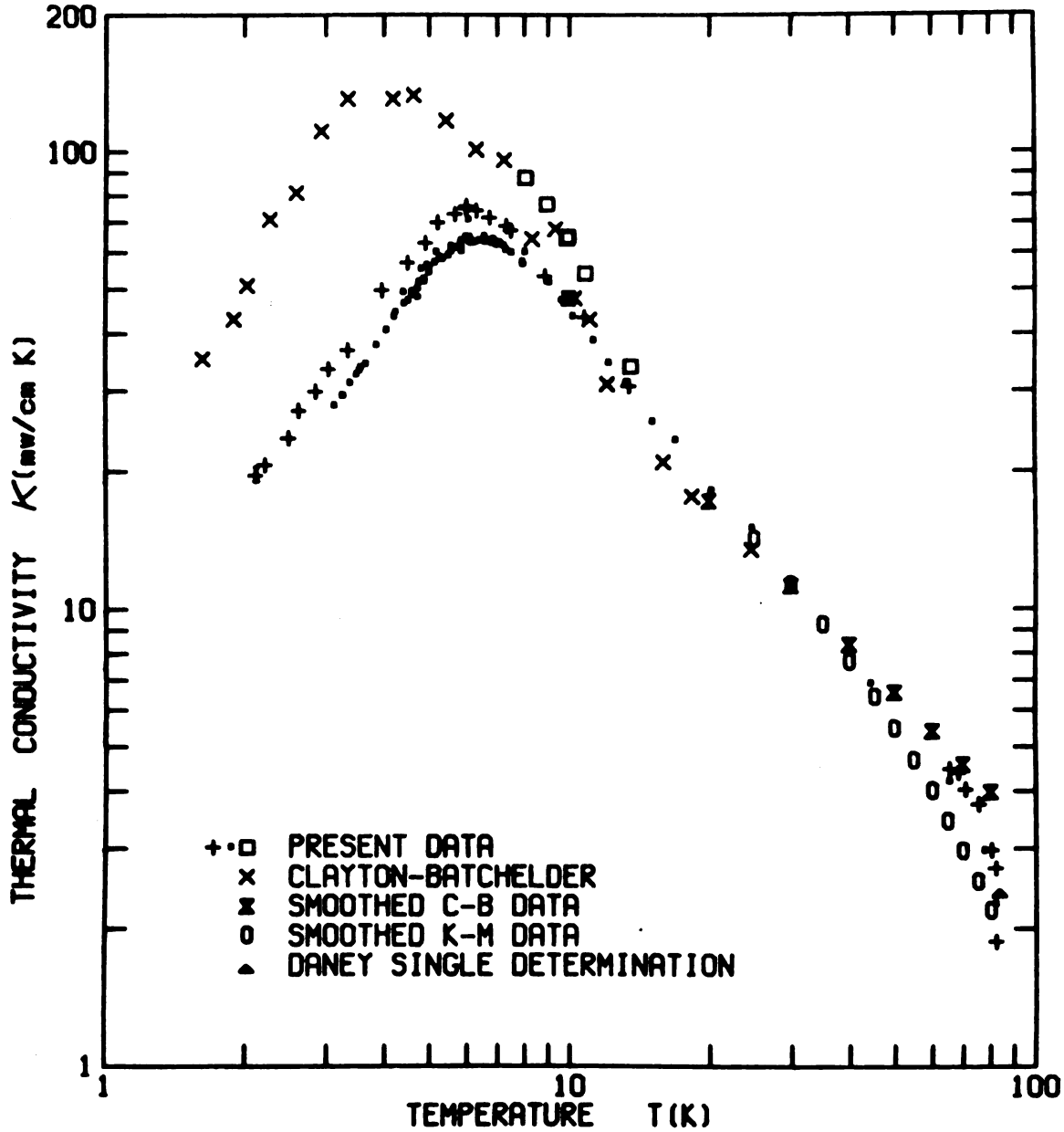

Figure 4: A plot of $\kappa(T)$ bs T including the results of Clayton and Batchelder, Krupskii and Manzhelii, and Daney.

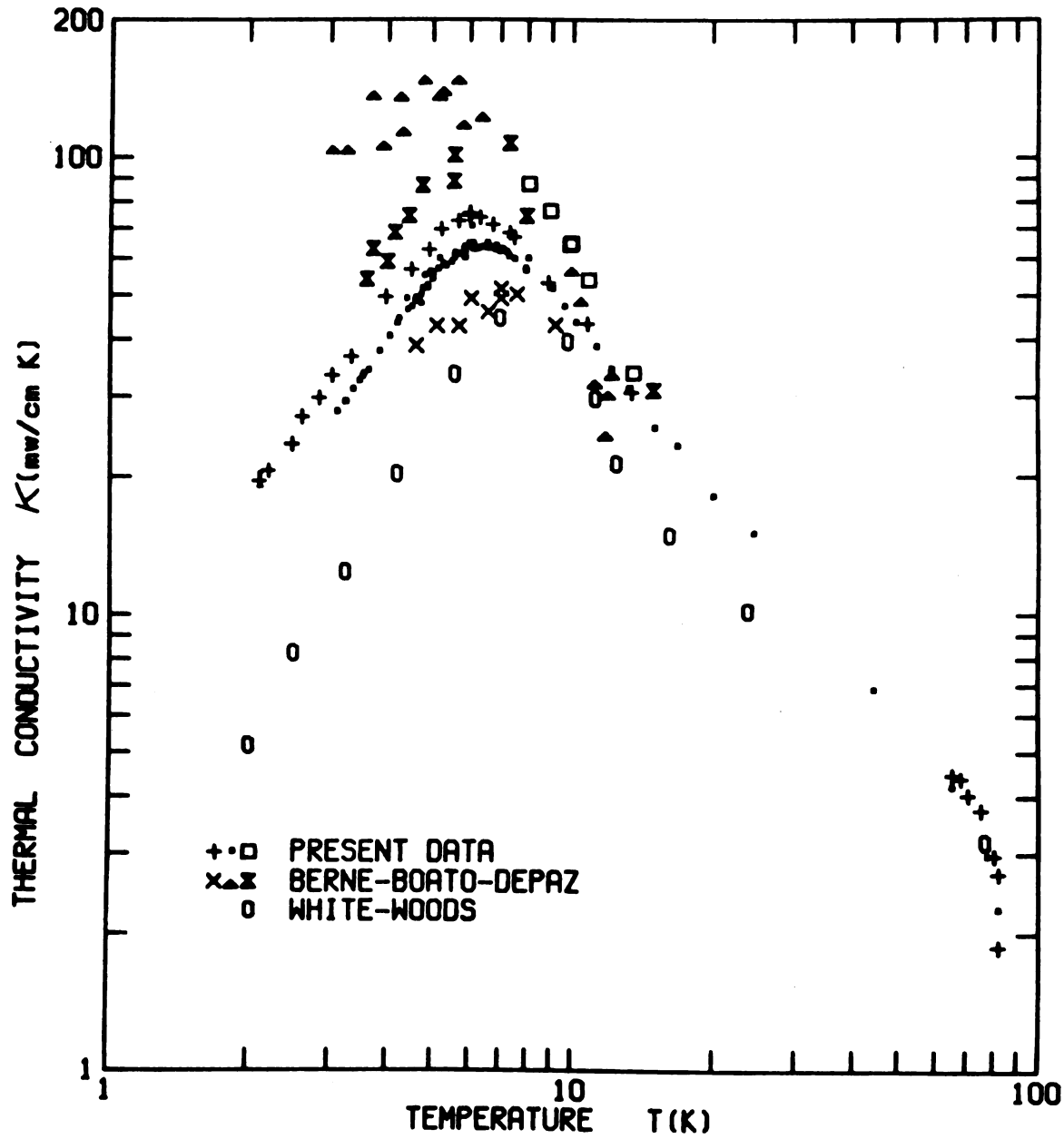

Figure 5: A plot of $\kappa(T)$ vs T including the results of Bernè, Boato, and Depaz, and White and Woods.

The data of White and Woods (W-W)[14] came from polycrystalline samples contained in a metal specimen tube. It is acknowledged by W-W that their samples were probably in a highly disordered state at the lower temperatures due to the constraints of the metal tube and their relatively rapid cooling rates.

The recent work of Clayton and Batchelder (C-B)[23] was carried out on solid Ar samples grown under conditions of high pressure. In this way, their measurements, employing a radial heat flow method, could be made on samples of essentially constant molar volume, and thus the volumetric dependence of $\kappa(T)$ examined. To facilitate comparison without data, we have included from their results the data from a sample whose molar volume was 22.53 ml, approximately that of free-standing Ar at 0^{o} K.

The data of Bernè, Boato, and Depaz (B-B-D)[16] is from the three polycrystalline samples for which they obtained the best reproducibility. Their experimental procedure involved extracting the sample from its specimen tube and attaching spring loaded clamps connected to the cold point and two gas thermometers. Thus measurements were made only at low temperatures, where the vapor pressure is negligible. One specimen they examined exhibited a much larger thermal conductivity (about 600 mw/cm K), than shown on Figure 5, but measurements made at the same temperature sometimes differed by a factor of two, a phenomenon which B-B-D attributed to problems of thermal contact.

The single determination of Daney[48] is included since it was obtained under equilibrium conditions at the triple point by relating the freezing rate of solid from the melt to the thermal conductivity, other necessary parameters being known.

B. Errors

1. High Temperature

The error bar shown in the high temperature range of Figure 2 is representative of what we estimate to be a maximum experimental error of 10-12%. The major contribution to this error is an uncertainty as large as 7% in the temperature differential ΔT.

In Chapter II Section A.2 we noted that the precision of temperatures measured with the Ge thermometer was limited to about ±3.5 mK at temperatures much above 60 K, due to the loss of sensitivity with increasing temperature. Since the difference between two temperature measurements determines ΔT, then a possible error of about ±7 mK can result.

In addition, in Appendix D we described quantitatively the problem of very long thermal relaxation times at high temperatures. For example, before conversion from a Cu to an Al lower block, we were experiencing thermal equilibration times of about 12 hr. at 80 K, thus requiring about 24 hr. for the acquisition of a single datum. After the conversion, this time was cut to about 6 hr.; however, it remained difficult to maintain the upper block temperature constant to better than 0.01 K during these extended periods. Although one would expect this latter error to somewhat average out during the course of a measurement, the compounded effects of these two types of temperature measurement errors place an upper limit on the deviation in ΔT at about ±17 mK. With the magnitude of ΔT of about 250 mK in this temperature range, its resulting maximum fractional error is 6-7%.

Uncertainties in the value of the geometrical factor L/A can also cause errors in the computed $\kappa(T)$. Since the length L was measured directly with a cathetometer, the error in this quantity is no more than

0.3%. The value of A, however, was assumed to be the cross-sectional area within the Mylar sample tube. At room temperature this volume is 0.915 cm^2, as determined by the size of the Teflon mandrel on which the tube was formed. At 84 K, its value is expected to have decreased by about 2% owing to the thermal contraction of Mylar, while at yet lower temperatures one has to correct A by employing the thermal expansivity of solid Ar. As a result, we estimate the error in A to be ± 2% over the entire temperature range.

A final source of error at high temperatures involves the accuracy to which we determine the conductance K_{cond} of spurious parallel heat conductors. We estimate this accuracy to be within ±3%. This estimate is based upon knowledge of the properties of the lower block and the goodness of fit of the data described in Appendix D.

The errors cited above propagate in $\kappa(T)$ to yield a maximum possible fractional error given by the expression,

$$\Delta\kappa/\kappa = \pm \left\{ \left|\Delta L/L\right| + \left|\Delta A/A\right| + \left| \frac{\Delta(\Delta T)/\Delta T}{(1 - \Delta T\, K_{cond}/\dot{Q})} \right| \right.$$

$$\left. + \left| \frac{\Delta K_{cond}/K_{cond}}{(\dot{Q}/\Delta T\, K_{cond} - 1)} \right| \right\} \qquad (4)$$

Evaluating Equation 4, one obtains, $\Delta\kappa / \kappa \simeq \pm 11\%$ at the highest temperatures.

2. Low Temperature

At low temperatures, at and below the peak in $\kappa(T)$, the control and accuracy of temperatures are much better, resulting in errors in the temperature differential ΔT, $\Delta(\Delta T)/\Delta T \simeq 0.2$ mK/20 mK $\simeq$ 1%. The geometrical errors are about the same as those described in the previous section, while the effect of spurious parallel heat conductors is negligible.

From Equation 4 we find that the maximum error in the low temperature $\kappa(T)$ is $\Delta\kappa/\kappa \simeq 3.5\%$.

Another source of error at low temperatures might be due to a non-negligible thermal boundary resistance between the Ar sample and the thermal sink or source. If such an effect existed, it would cause a temperature differential across the interface between the sample and block, and would thus result in an apparent suppression in the measured thermal conductivity. The possible sources of this phenomenon are: (i) Mismatch in the acoustic impedances of the sample and block (Kapitza Resistance). (ii) Some sort of disorder in the sample near its ends, resulting in a much lower thermal conductivity in that region. (iii) A purely geometrical effect whereby the effective surface area of the sample in contact with the block is greatly reduced (perhaps by contraction, etc.).

The transport of heat across metal-insulator interfaces at low temperatures has been studied for the case where the insulator is Mylar.[36] Expecting that these results can apply within an order of magnitude to solid Ar, we find that the acoustic mismatch effect (i) is completely negligible at the lowest temperatures studied (i.e. the thermal boundary resistance $R_B \simeq 10^{-3}/T^3$ (K/mw) $<<$ $R_{Ar} = (L/A)/\kappa$). Effects (ii) and (iii), however, remain possible sources of error.

An empirical method of assessing the severity of these types of errors is straightforward. Assuming that the thermal contact resistance remains essentially constant from one run to the next, one can simply determine $\kappa(T)$ for samples with different geometrical factors (L/A). The Ar sample thermal resistance R_{Ar} will be the larger fraction of the total resistance for the case of the larger (L/A). Thus, for a given geometry the apparent measured thermal conductivity $\kappa(T)_{app} = \dot{Q}\,(L/A)/\Delta T$

is related to the real sample thermal conductivity $\kappa(T)$ according to,

$$1/\kappa(T)_{app} = 1/\kappa(T) + R_c/(L/A). \quad (5)$$

Thus, for constant R_C, the sample with the larger (L/A) should display a larger apparent thermal conductivity.

This analysis can be applied to runs #10 and #8, for which $(L/A)_{10} = 2.63$ and $(L/A)_8 = 3.5$. The lower geometrical factor for run #10 was obtained simply by shortening the sample tube consistent with other experimental requirements. A quick glance at Figure 3 shows that the observed effect is contrary to Equation 5. Therefore, if the boundary resistance is present, its magnitude either decreased drastically from run #8 to #10, or there are other more predominant effects which influence $\kappa(T)$ from run to run. We believe the latter to be true, since we observed a marked dependence of $\kappa(T)$ on the strain state of the sample, which is extremely sensitive to factors involving sample manipulation. Thus, whatever thermal boundary resistance is present is concluded to be of negligible relative magnitude.

C. Remarks

At this point we discuss some general features of the observed temperature dependent thermal conductivity. Various, but not entirely inequivalent, theoretical models have been proposed which predict $\kappa(T) \propto T^{-1}$ for $T \geq \Theta_D$.[37-40] This dependence results from application of first order perturbation theory to the third order anharmonic terms in the crystal Hamiltonian. Such a theory predicts interactions between three phonons (either two combine to produce one, or one splits into two), and the T^{-1} behavior of $\kappa(T)$ is essentially the consequence of high T phonon occupation numbers varying linearly with temperature.

Our data, however, appear to indicate a more precipitous decrease in $\kappa(T)$ with increasing temperature. This observation is in general agreement with the work of Krupskii and Manzhelii,[17] whose endeavors dealt only with the high T dependence of $\kappa(T)$. The K-M data demonstrated a temperature dependence, $1/\kappa = AT + BT^2$ $(A,B > 0)$. These investigators attempted to explain this result in terms of higher order phonon-phonon transitions. It was originally suggested by Pomeranchuck[41] and shown by Ziman,[40] for example, that the application of higher order perturbation theory to higher order anharmonic crystal force terms results in a power series dependence of the thermal resistivity $(W = 1/\kappa)$ on T. In particular, $W \propto T^2$ is indicative of four-phonon processes, as is found by application of first order perturbation theory to the fourth order anharmonic potential, and second order perturbation theory to the third order potential terms. Therefore, K-M proposed that four-phonon processes accounted for the quadratic component in their experimental results.

The high T measurements of Clayton and Batchelder,[23] performed on isochoric samples, displayed only first order temperature dependence. As a result, they reconciled their observations with those of K-M by claiming the quadratic contribution in the results of K-M were due to the effects of thermal expansion of the lattice. According to this explanation, the expansion of the crystal with increasing temperature, due to the cubic anharmonic crystal potential, effectively decreases the Debye temperature. A measure of the effect is the Gruneisen constant $\gamma = -\partial \ell n \Theta_D / \partial \ell n V$, and the resultant fractional change in the thermal conductivity for a given volume change is approximately,

$$\Delta\kappa/\kappa \simeq -(3\gamma + 5/3)\Delta V/V. \qquad (6)$$

With this relation, C-B demonstrated reasonable agreement between their data at 75 K and the appropriately normalized (according to Equation 6) results of K-M, thus refuting the existence of four-phonon contributions. We examine this question more closely in Chapter IV.

As the temperature is lowered, $\kappa(T)$ is seen to rise and then turn over at about 6 K. Were the crystal infinite and perfect, $\kappa(T)$ would continue to rise with decreasing temperatures approximately as $T^n \exp(\Theta_D/bT)$, where the constants n and b are of the order unity.[42] This behavior is explained by the exponential dying out at low temperatures of phonons with wavevectors large enough to participate in the resistive Umklapp-type collisions originally described by Peierls.[37]

Whether this exponential behavior is ever actually observed, as well as the exact position and amplitude of the peak in $\kappa(T)$, are both sensitive functions of the various types of crystal defects which limit the phonon mean free path as the Umklapp phonon-phonon collisions vanish. White and Woods'[14] data indicate the peak in $\kappa(T)$ occurs at $T \simeq 8$ K, about $\Theta_D/10$, whereas our, C-B, and B-B-D results are closer to $\Theta_D/20$. This latter value is more in tune with that of other insulating materials (e.g. Ge, Si, Te, Be, Diamond).[42]

Below the peak, $\kappa(T)$ decreases in accordance with the diminishing number of phonons available to transport energy, and with the nature of the scattering mechanism predominantly limiting the phonon mean free path. At the lowest temperatures, our data indicate $\kappa(T) \lesssim T^2$ (with reservations to be discussed). This functional dependence is in agreement with other researchers[16,24] who have made measurements on solid Ar in this temperature range, although the magnitudes vary widely. According to current theories, $\kappa(T) \propto T^2$ is indicative of phonon scattering due to

the static strain fields surrounding dislocations.[20,43,44] These theories, however, appear to severely underestimate the strength of the scattering, as indicated by studies of the thermal conductivity of deformed alkali halides.[45-47] In Chapter IV we describe some of the above theories in more detail and show they predict rather large dislocation densities when applied to our and existing data.

It should be noted that, while the high T data are fairly reproducible from run to run (and from experimenter to experimenter), the low T data may vary by nearly an order of magnitude. This is, of course, due to the fact that $K(T)$ at low T is extremely sensitive to the history of the sample, i.e. its defect structure, while the high T lattice wave scattering from defects is negligible in comparison to the much more rapid anharmonic phonon-phonon interactions.

IV. THEORY

A. Preliminary Remarks

In order to understand the conduction of thermal energy through an insulating solid, one would prefer to account, in a fundamental way, for the manner in which the vibrating atoms of the lattice interact with one another and with crystal defects, and then somehow relate this knowledge to the macroscopic quantities: the heat flux $\vec{Q}$, the temperature T, and its gradient ∇T. This problem is normally attacked with the use of various semi-empirical models and approximation techniques applied to a Boltzmann equation for the "phonon gas".[19,20,40,50,51] Few workers have endeavored to approach this problem from as fundamental a level as the interatomic potential, although in recent years the digital computer has facilitated the direct application of lattice dynamics and perturbation theory to certain specialized problems.[52-56]

A fundamental theoretical approach to the problem of heat transport in solid Ar is especially fruitful due to the relative simplicity of this solid. Moreover, one need consider only phonon contributions to the energy conduction and may safely neglect several kinds of interactions between electrons and phonons. Most important, though, is that a quantitative test of a given transport theory may be made since it appears there now exists a semi-empirical interatomic potential which accurately predicts many thermodynamic properties of gaseous, liquid, and solid Ar.[21,22,57,58]

In the following, we describe contributions to the thermal resistivity due to mechanisms of anharmonic three-phonon processes, strain field scattering of phonons (point defects and dislocations), and boundary scattering, all within the context of the Peierls-phonon-Boltzmann equation.[37] Although this problem may be approached somewhat more elegantly with the use of linear response theory,[54,59] it is found that when the usual approximations are made, the two approaches are equivalent.[20] For the contribution of three-phonon processes to the thermal resistivity, we employ a technique proposed by Krumhansl.[60] However, this approach is, for our application, found to be equivalent to that of Ziman.[40] This technique uses a numerical method which utilizes the phonon dispersion relations and group velocities obtained in the quasi-harmonic approximation, derived from the familiar Lennard-Jones 6-12 potential,[61] and also derived from the potential of Barker and Bobetic.[21] The latter potential includes the effect of three-body interactions of the triple-dipole type.[62]

These results are then compared to experimental data in an appropriate temperature region. The relaxation time approximation to the solution of the phonon-Boltzmann equation is also discussed [63,64] along with numerical evaluation by this method of the low temperature thermal conductivity.

B. Harmonic Lattice Waves

In the quasi-harmonic approximation, the total lattice potential energy Φ is expanded in a Taylor series of small displacements $\vec{u}_\ell$ about the equilibrium site $\vec{R}_\ell$ of the atom identified by the subscript ℓ. Thus, for atoms at instantaneous positions $\vec{r}_\ell = \vec{R}_\ell + \vec{u}_\ell$, the crystal potential is,

$$\Phi\{\vec{r}_\ell\} = \Phi\{\vec{R}_\ell\} + \sum_{\ell\alpha} \frac{\partial\Phi\{\vec{R}_\ell\}}{\partial R_\ell^\alpha} u_\ell^\alpha + \tfrac{1}{2}\sum_{\ell\ell'}{}' \sum_{\alpha\beta} \frac{\partial^2\Phi}{\partial R_\ell^\alpha \partial R_{\ell'}^\beta} u_\ell^\alpha u_{\ell'}^\beta + \ldots \tag{7}$$

Here, Greek superscripts denote cartesian vector components. In the simplest case, of which solid Ar is an approximate example, $\Phi(\{\vec{r}_\ell\})$ may be expressed as the sum of two-body potentials $\phi(|\vec{r}_{\ell\ell'}|)$ as,

$$\Phi(\{\vec{r}_\ell\}) = \tfrac{1}{2}\sum_{\ell\ell'}{}' \phi(|r_{\ell\ell'}|)$$

where we define $\vec{r}_{\ell\ell'} = \vec{r}_\ell - \vec{r}_{\ell'}$, $\vec{R}_{\ell\ell'} = \vec{R}_\ell - \vec{R}_{\ell'}$, and $\vec{u}_{\ell\ell'} = \vec{u}_\ell - \vec{u}_{\ell'}$ These latter variables, for computational reasons, are the more convenient in which to expand Φ. Thus the second order term in Equation 7 is given by,

$$\Phi^{(2)} = 1/4\sum_{\ell\ell'}{}' \sum_{\alpha\beta} \phi_{\alpha\beta}(R_{\ell\ell'})\ u^\alpha_{\ell\ell'}\ u^\beta_{\ell\ell'} \tag{8}$$

where,

$$\phi_{\alpha\beta}(R_{\ell\ell'}) = \partial^2\phi(R_{\ell\ell'})/\partial R^\alpha_{\ell\ell'}\ R^\beta_{\ell\ell'}\,.$$

In solving for the normal modes of the crystal, the zeroth order term $\Phi^{(0)}$ is just a constant energy shift, while the first order term $\Phi^{(1)}$ has an average value zero (although $\partial\Phi/\partial R_{\ell\ell'}$ is not necessarily zero in the quasi-harmonic approximation). Thus, one solves for the

normal modes of the crystal by applying the theory of Born-von Kármánn[65], to the quasi-harmonic crystal Hamiltonian,

$$H = \sum_{\ell} \frac{P_{\ell}^2}{2m} + 1/4 \sum_{\ell\ell'}' \sum_{\alpha\beta} \phi_{\alpha\beta}(R_{\ell\ell'}) \; u^{\alpha}_{\ell\ell'} u^{\beta}_{\ell\ell'} . \tag{9}$$

Here, $\vec{P}_{\ell} = m\dot{\vec{u}}_{\ell}$ is the momentum of the atom ℓ, and m its mass, assumed to be the same for all atoms of the ideal crystal.

The equations of motion for the atomic displacements at site ℓ are,

$$m\ddot{u}^{\alpha}_{\ell} = - \sum_{\ell\beta} \phi_{\alpha\beta}(R_{\ell\ell'}) \; u^{\beta}_{\ell\ell'}. \tag{10}$$

Due to the translational periodicity of the ideal lattice, if $\ell \to \ell'$ in Equation 10 the solutions must be the same, aside from a possible phase difference depending on the site ℓ. Thus, $u^{\alpha}_{\ell} = e^{\alpha} \exp(i\vec{q}\cdot\vec{R}_{\ell}) \exp(-i\omega t)$. The quantity e^{α} is an amplitude, $\vec{q}$ is a constant vector which is seen to appear as a wavevector, and we have assumed an oscillatory time dependence. The, Equation 10 is,

$$\omega^2 \; e^{\alpha} = 1/m \sum_{\ell'\beta}' \phi_{\alpha\beta}(R_{\ell\ell'}) \; (1 - \exp(-i\vec{q}\cdot\vec{R}_{\ell\ell'})) \; e^{\beta}.$$

Here, the quantity,

$$D_{\alpha\beta}(\underset{\sim}{q}) = 1/m \sum_{\ell'}' \phi_{\alpha\beta}(R_{\ell\ell'}) \; (1 - \exp(-i\vec{q}\cdot\vec{R}_{\ell\ell'})), \tag{11a}$$

is called the dynamical matrix, which is symmetric. The dynamical matrix is real for a crystal with inversion symmetry. So,

$$\omega^2 \; e^{\alpha} = \sum_{\beta} D_{\alpha\beta}(\vec{q}) \; e^{\beta}, \tag{11b}$$

is an eigenvalue equation which can be solved for three frequencies $\omega_{\underset{\sim}{q}s}$ and for the associated real polarization eigenvectors $e_{\underset{\sim}{q}s}$, $s = 1, 2, 3$. By imposing cyclic boundary conditions, and requiring that the total

number of modes of the crystal be 3N, where N= number of atoms in the crystal, one obtains that there are N wavevectors $\underset{\sim}{q}$ of the form,

$$\vec{q} = 2\pi/a_o n_m (n_x, n_y, n_z) \tag{12}$$

In Equation 12, a_o is the lattice constant of the fcc crystal, $n_m = (N/4)^{1/3}$ and n_x, n_y, and n_z are integer constants such that $|n_x|$, $|n_y|$, $|n_z| \leq n_m$ and $|n_x| + |n_y| + |n_z| \leq \frac{3}{2} n_m$. These latter two conditions stipulate that $\vec{q}$ must remain with the first Brillouin zone of the bcc reciprocal lattice of the crystal, since any wavevector outside that region represents lattice waves of wavelength less than a_o and thus is physically meaningless.

By quantizing the above results (i.e. requiring $[\vec{u}_\ell, \vec{p}_\ell] = i\hbar \vec{1}$ one finds the normal mode oscillators of energy $\hbar\omega_{\underset{\sim}{qs}}$ are populated with quantum excitations called phonons. These elementary excitations are considered as plane waves with "pseudo-momentum" $\hbar\underset{\sim}{q}$, propagating independently of one another. If the ideal crystal is at some temperature T, the average number of phonons $N^0_{\underset{\sim}{qs}}$ occupying a given oscillator state of energy $\hbar\omega_{\underset{\sim}{qs}}$ is given by the Bose-Einstein distribution,

$$N^0_q = \left[\exp(\hbar\omega_q / k_B T) - 1\right]^{-1} \tag{13}$$

where k_B is the Boltzmann constant, and $q \equiv \vec{q}, s$.

By canonically transforming to a new set of coordinates a_q and $a^\dagger_q$ such that $[a^\dagger_q, a_{q'}] = \delta_{qq'}$, the situation can be viewed in phonon occupation number space. In this representation, the displacement coordinates of an atom at site ℓ in the crystal are,

$$\vec{u}_\ell = \sqrt{\hbar/2mN} \sum_q \frac{\vec{e}_{\underset{\sim}{q}}}{\sqrt{\omega_q}} \exp(i\vec{q}\cdot\vec{R}_\ell)\ (a_q - a^\dagger_{-q}), \tag{14}$$

and the harmonic Hamiltonian of the crystal given by Equation 9 takes the form,

$$H = \sum_{q} \hbar\omega_q \ (a_q^\dagger a_q + 1/2). \tag{15}$$

The quantity $a_q^\dagger a_q$ is a Hermitian operator in occupation number space, whose eigenvalue is the number of phonons in state q. Thus,

$$a_q^\dagger a_q |N_q> = N_q \ |N_q>. \tag{16}$$

The operators a_q and $a_q^\dagger$ are, themselves, non-Hermitian, and have only off-diagonal matrix elements.

$$a_q |N_q> = \sqrt{N_q} \ |N_q - 1> \ ,$$

$$a_q^\dagger |N_q> = \sqrt{N_q + 1} \ |N_q + 1> \ . \tag{17}$$

C. Transport Equation and Thermal Conductivity

In a perfect, harmonic crystal, where the phonons are true normal mode excitations, once the oscillator states are occupied, no change in the occupation number can occur unless some external force perturbs the system. The phonons move independently with pseudo-momentum $\hbar\vec{q}$ and do not interact with one another. Therefore, if one supplied energy at one end of a perfect crystal, phonons would be created and would propagate uninhibited to the opposite end. Thus, energy would flow with no established temperature gradient, so that a thermal conductivity in this case is undefined. In reality, of course, phonons are not true normal modes due to anharmonicity and breaks in the lattice translational symmetry, so that energy is attenuated and κ is finite. As a result, one can speak of a steady state situation whereby the phonon distribution at any point in the crystal is static under the combined influence of the driving thermal gradient ∇T and the resistive phonon collisions.

Under the influence of only small driving forces, it is assumed the steady state phonon distribution function N_q is only slightly different from the equilibrium Bose-Einstein distribution N_q^0. So, we may write:

$$N_q = N_q^0 + n_q \quad . \tag{18}$$

Here n_q is the deviation from equilibrium. In Equation 18, N_q^0 at any position $\vec{r}$ in the crystal is evaluated for the temperature at that point. In the steady state, energy is flowing at a constant rate from the high to the low temperature end of the solid, and this energy flux is given by,

$$\vec{Q} = 1/\Omega \sum_q N_q \, \hbar\omega_q \, \vec{v}_q = 1/\Omega \sum_q n_q \, \hbar\omega_q \, \vec{v}_q, \tag{19}$$

where $\vec{v}_q$ is the phonon group velocity $\partial\omega_q/\partial\vec{q}$, and Ω is the total volume. There is no contribution to the heat flux from the equilibrium distribution, since it is an even function of $\vec{q}$, as is ω_q, while $\vec{v}_q = -\vec{v}_{-q}$ for a cubic crystal. If n_q is found in terms of the temperature gradient ∇T, then Equation 19 provides an expression for κ. Hardy,[66] as well as Maradudin[67] and Magid[68], has shown that Equation 19 is but an approximation to the true average heat flux, with other contributions coming from non-diagonal terms. These are shown by Hardy to be time dependent oscillatory functions in the classical harmonic approximation, and thus contribute a negligible time-averaged result.

By using the fact that in the steady state the mean number of phonons in any volume element does not change, one can find a transport equation which, in principle, would yield n_q. The time rate of change of N_q is,

$$dN_q/dt = \partial N_q/\partial t + \vec{v}_q \cdot \nabla N_q . \qquad (20)$$

In the steady state $\partial N_q/\partial t = 0$, and dN_q/dt represents the rate of change determined by scattering. The second term on the r.h.s. of Equation 20 is the change in N_q due to thermal diffusion. Then, in the steady state,

$$\vec{v}_q \cdot \nabla T \; \partial N_q/\partial T = \dot{n}_q . \qquad (21)$$

In Equation 21, it is assumed the spatial dependence of N_q is through the temperature $T(\vec{r})$, and, to first order in ∇T, $\partial N_q/\partial T = \partial N_q^0/\partial T$.

It is usually possible to express the collision rate $\dot{n}_q$ in terms of a non-linear operator. This collision operator may, however, be linearized to a good approximation[19] such that $\dot{n}_q = \sum_{q'} G_{qq'} n_{q'}$. In principle, one could then solve Equation 21 for n_q by inverting G, provided it has an inverse.

It has been more often the practice to approximate $\dot{n}_q$ by use of a phenomenological relaxation time τ_q defined by[20]:

$$\dot{n}_q = -n_q/\tau_q . \qquad (22)$$

Here, τ_q is the characteristic time required for a disturbed phonon distribution N_q to relax back to N_q^0 by means of phonon collisions. Much work has been devoted to finding the functional form of τ_q in terms of $\vec{q}, \omega_q$ and T for various types of scattering processes.[20,41,43,44,50,69,73] In general, τ_q will include in some average way the occupations of all other states, although a single mode relaxation time can be defined in terms of the diagonal components of the collision operator, i.e. $\dot{n}_q \simeq G_{qq} n_q \equiv -n_q/\tau_q$; with all other $n_{q'} = 0$.

From Equations 19, 21, and the relaxation approximation Equation 22, one has,

$$\vec{Q} = - 1/\Omega \sum_q \hbar\omega_q \, \partial N_q^0/\partial T \, \tau_q \, \vec{v}_q \, \vec{v}_q \cdot \nabla T.$$

For a crystal with cubic symmetry $\vec{Q} \propto \nabla T$, and one has

$$\vec{Q} = -1/3 \sum_q C_v(q) \, \tau_q \, v_q^2 \, \nabla T,$$

or,

$$\kappa(T) = 1/3 \sum_q C_v(q) \, \tau_q \, v_q^2, \tag{23}$$

where $C_v(q) = \frac{\hbar\omega_q}{\Omega} \frac{\partial N_q^0}{\partial T}$ is the specific heat/unit volume of the phonon state q. Equation 23 is instructive since it is analogous to the expression,

$$\kappa = 1/3 \, C_v \, \tau \, \langle v^2 \rangle$$

of a classical gas.

In the above discussion, it has been implicitly assumed that phonons have been localized in space, since one must speak of a phonon distribution function N_q which characterizes a "local" phonon occupation number. It is obvious that true phonons, which correspond to plane waves in the crystal, are inadequate for this description, but rather wave packet superposition states must be used. In order to characterize a wave packet by a single wavevector $\vec{q}$ and frequency ω_q, we must satisfy the relation $\delta\vec{q} << \vec{q}$, where $\delta\vec{q}$ is the wavevector spread of the packet; but at the same time we must stipulate that the wave packet not be too spatially large when compared to, say, the thermal gradient. The spread in the wavevector and position of a wave packet are related according to $\delta q_x \delta x \simeq 1$.

The condition that the energy spread is not too large is obtained

from the distribution function $N_q^0 = [\exp(\hbar\omega_q/k_BT)-1]^{-1}$ by demanding $\hbar\delta\omega_q/k_BT << 1$.[19] In the Debye approximation, $\hbar\delta\omega = v_D\hbar\delta q \simeq a_o k_B\Theta_D\delta q$. So, $\delta q << T/\Theta_D a_o$ is an appropriate condition on the wavevector. For the criterion that the spatial extent of the packet is not too large, we demand that the change in N_q^0 over the width of the packet, due to the thermal gradient, be negligible, i.e.

$$\partial N_q^0/\partial x\ \delta x << N_q^0, \text{ or } \partial N_q^0/\partial T\ \partial T/\partial x\ \delta x << N_q^0.$$

This relation provides the condition,

$$\delta x << \frac{(1 - \exp(-\hbar\omega/k_BT))}{\hbar\omega/k_BT\ \ \frac{(\partial T/\partial x)}{T}}.$$

Thus, it is required that

$$\delta q_x\,\delta x << T/\Theta_D a_o\ \frac{(1 - \exp(-\hbar\omega/k_BT))}{\hbar\omega/k_BT\ \ \frac{(\partial T/\partial x)}{T}}.$$

Since $\delta q_x\delta x \simeq 1$, this requirement will be satisfied only if

$$T/\Theta_D a_o\ \frac{(1 - \exp(-\hbar\omega/k_BT))}{\hbar\omega/k_BT\ \ \frac{(\partial T/\partial x)}{T}} >> 1. \qquad (24)$$

Even at low temperatures, this inequality is easily obeyed for experimentally reasonable values of $(\partial T/\partial x)/T$. Therefore, under these conditions it is permissible to speak of a "phonon" characterized by a wavevector $\vec{q}$, frequency ω_q, and velocity $\partial\omega_q/\partial\underset{\sim}{q}$, as well as a position coordinate in the crystal.

D. Phonon Scattering Processes

1. Three-Phonon Processes

a. Formalism

In this section we present the three-phonon anharmonic scattering operator $C_{qq'}$ linearized in the manner suggested by Peierls.[19] Although this operator does not have simple properties, it may be symmetrized by a simple transformation,[39,60] and the thermal conductivity evaluated using a formalism developed by Krumhansl,[60] and applied by Bennett.[53] The validity of the computation is discussed, and its results for various forms of the interatomic potential are compared with experiment in the temperature range applicable.

In a perfect, but anharmonic, lattice, Peierls[19] showed that the anharmonic terms in the potential energy expansion account for phonon-phonon scattering which can give rise to thermal resistance by the so-called Umklapp process.

This can be seen by considering Born approximation transition rates between pure phonon states, regarding the third order term in the potential energy Taylor expansion as the perturbation,

$$\phi^{(3)} = 1/12 \sum_{\ell\ell'}{}' \sum_{\alpha\beta\gamma} \phi_{\alpha\beta\gamma}(R_{\ell\ell'}) u^{\alpha}_{\ell\ell'} u^{\beta}_{\ell\ell'} u^{\gamma}_{\ell\ell'}, \tag{25}$$

where,

$$\phi_{\alpha\beta\gamma}(R_{\ell\ell'}) = \frac{\partial^3 \phi(R_{\ell\ell'})}{\partial R^{\alpha}_{\ell\ell'} \partial R^{\beta}_{\ell\ell'} \partial R^{\gamma}_{\ell\ell'}} .$$

Expressing the $u_{\ell\ell'}$ in terms of the normal mode coordinates of Section B, gives:

$$u^{\alpha}_{\ell\ell'} = \sqrt{\hbar/2mN} \sum_{q} \frac{e^{\alpha}_{q}}{\sqrt{\omega_q}} \left[\exp(i\vec{q}\cdot\vec{R}_{\ell\ell'}) - \exp(i\vec{q}\cdot\vec{R}_{\ell\ell'})\right] \ (a_q - a^{\dagger}_{-q}). \quad (26)$$

Substituting Equation 26 into Equation 25, we obtain for the perturbation:

$$\phi^{(3)} = N/6 \ (\hbar/2N)^{3/2} \sum_{qq'q''} \frac{\Phi(qq'q'')}{(\omega_q \omega_{q'} \omega_{q''})^{\frac{1}{2}}} (a_q - a^{\dagger}_{-q})(a_{q'} - a^{\dagger}_{-q'})(a_{q''} - a^{\dagger}_{-q''}). \quad (27)$$

In Equation 27, the quantity $\Phi(q\ q'\ q'')$ is a third order lattice Fourier transform defined as in Maradudin, et al.,[74]

$$\Phi(q\ q'\ q'') = 1/2m^{3/2} \sum_{\ell'} \sum_{\alpha\beta\gamma} \phi_{\alpha\beta\gamma}(R_{\ell\ell'})\ e^{\alpha}_{q}\ e^{\beta}_{q'}\ e^{\gamma}_{q''}$$

$$(1-\exp(i\vec{q}\cdot\vec{R}_{\ell\ell'}))(1-\exp(i\vec{q}\cdot\vec{R}_{\ell\ell'}))(i-\exp(i\vec{q}\cdot\vec{R}_{\ell\ell'})). \quad (28)$$

The extra factor of N in Equation 27 arises from the fact that the lattice sum $\sum'_{\ell\ell'}$ is written $N \sum'_{\ell'}$, i.e. we have fixed on the atom at the origin, and summed over its neighbors.

Then, the first order transition rate from a total phonon occupation state $|N_i\rangle$ to a state $|N_f\rangle$ is,

$$P_{i\to f} = 2\pi/\hbar^2 \ |\langle N_f|\Phi^{(3)}|N_i\rangle|^2 \ \delta(\omega_f - \omega_i). \quad (29)$$

From Equation 27, it is seen that $\Phi^{(3)}$ couples states such that the initial state has either two more or one less phonons than the final state (e.g. $a^{\dagger}_{q} a_{q'} a_{q''}$ destroys phonons q', q'' in the initial state, and creates phonon q in the final state). These transitions are seen to obey energy conservation of the form $\omega_q \pm \omega_{q'} \pm \omega_{q''} = 0$. Furthermore, from the invariance of $\Phi^{(3)}$ for a constant displacement

of the entire crystal through a lattice vector, one can easily show that $\Phi(qq'q'') = 0$ unless $\vec{q}+\vec{q}'+\vec{q}'' = \vec{G}$, where $\vec{G}$ is a vector of the recriprocal lattice given by,

$$\vec{G} = 2\pi/a_o \ (i, j, k), \tag{30}$$

with i, j, and k being integers either all odd or all even. Thus, the three-phonon transitions of Equation 29 are subject to the conservation laws,

$$\omega_q \pm \omega_{q'} \pm \omega_{q''} = 0,$$

and

$$\vec{q} \pm \vec{q}' \pm \vec{q}'' = \vec{G}. \tag{31}$$

These appear as conservation of energy and momentum, except that, in the latter case, the phonon "pseudo-momentum" is conserved only if $\vec{G} = 0$. Transitions for which $\vec{G} = 0$ are known as Normal (N) processes, and they do not contribute directly to the thermal resistance. However, if for example $\vec{q}+\vec{q}'$ lies outside the first Brillouin zone, then $\vec{q}'' = \vec{q} + \vec{q}' - \vec{G}$, where $\vec{G}$ is a reciprocal lattice vector which brings $\vec{q}''$ back into the allowed region. Thus, this process has the effect of "flipping over" the resultant wavevector to produce a phonon traveling, in a sense, oppositely to the original flow. This is the Umklapp (U) mechanism by which Peierls first explained thermal resistance of a perfect, but anharmonic, crystal.[37]

To find the rate of change in the occupation of phonon states due to first order collisions, one invokes Equation 29 and a Master equation,

$$\dot{n}_q = \sum_{q'} \left| P_{q'\to q} - P_{q\to q'} \right|,$$

to obtain,

$$\dot{n}_q = 2\pi/\hbar^2\ \hbar^3/32N \sum_{q'q''} \{2|\Phi(qq'-q'')|^2\ (N_q+1)(N_{q'}+1)N_{q''}$$

$$- |\Phi(-qq'\ q'')|^2\ N_q(N_{q'}+1)(N_{q''}+1) + |\Phi(q-q'-q'')|^2 \qquad (32)$$

$$\cdot\ (N_q+1)N_{q'}N_{q''} - 2|\Phi(qq'-q'')|^2\ N_qN_{q'}(N_{q''}+1)\}/\omega_q\omega_{q'}\omega_{q''}\ .$$

In the above, we have written implicitly, for example,

$$\Phi(qq'-q'') \Rightarrow \Phi(qq'-q'')\ \delta(\omega_q + \omega_{q'} - \omega_{q''})\ \Delta(\vec{q} + \vec{q}' - \vec{q}'').$$

In the present form, Equation 32 is non-linear and hopelessly complicated, but we linearize it by writing in the usual way, $N_q = N_q^0 + n_q$ and retaining only first order terms in the n_q ,[19] (e.g. $(N_q + 1)(N_{q'} + 1)N_{q''} \rightarrow n_q(N_{q'}^0 + 1)N_{q''}^0 + n_{q'}(N_q^0 + 1)N_{q''}^0 + n_{q''}(N_q^0 + 1)(N_{q'}^0 + 1)$. After some algebra, the details of which are shown in Appendix E, one can define a collision operator according to,

$$\dot{n}_q = \sum_{q'} G_{qq'}\, n_{q'},$$

where, for the diagonal elements:

$$G_{qq} = -\hbar\pi/16N \sum_{q''}\left\{\frac{\sinh(x/2)}{\sinh(x'/2)\ \sinh(x''/2)}\left[|\Phi(qq'-q'')|^2\right.\right.$$

$$\left.\left. + \tfrac{1}{2}|\Phi(q-q'-q'')|^2\right]/\omega\omega'\omega'' + \frac{\left[|\Phi(q-q-q'')|^2 - |\Phi(qq-q'')|^2 + |\Phi(qq-q'')|^2\right]}{\sinh(x''/2)\ \omega\omega\ \omega''}\right\}. \qquad (33a)$$

and for the non-diagonal elements:

$$G_{qq'} = -\hbar\pi/16N \sum_{q''} \frac{\sinh(x'/2)}{\sinh(x/2)\ \sinh(x''/2)}\left[-|\Phi(q-q'-q'')|^2\right.$$

$$\left. - |\Phi(qq''-q')|^2 + |\Phi(qq'-q'')|^2\right]/\omega\omega'\omega''. \qquad (33b)$$

In Equations 33a and 33b, we use an obvious notation, and employ the dimensionless quantity $x = \hbar\omega/k_B T$.

We rewrite here the phonon-Boltzmann Equation 21 in the form,

$$\theta_q = \sum_{q'} G_{qq'} n_{q'} , \tag{34}$$

where, $\theta_q = \vec{v}_q \cdot \nabla T \, \partial N_q/\partial T$. Although the collision operator in its present form is non-symmetric in q, q′, there exist simple transformations which symmetrize it.[39,60] One of these, used by Krumhansl,[60] results in the following quantities:

$$n^*_q = 2 \sinh(x/2) \; n_q ,$$

$$\theta^*_q = 2 \sinh(x/2) \; \theta_q ,$$

$$G^*_{qq'} = 2 \sinh(x/2) \; G_{qq'} (2 \sinh(x'/2))^{-1}.$$

Then,

$$\theta^*_q = \sum_{q'} G^*_{qq'} n^*_{q'} , \tag{35}$$

and,

$$G^*_{qq} = -\hbar\pi/16N \sum_{q''} \left\{ \frac{\sinh(x/2)}{\sinh(x'/2) \; \sinh(x''/2)} \left[|\Phi(qq'-q'')|^2 \right.\right.$$

$$\left.\left. + \frac{1}{2} |\Phi(qq'-q'')|^2 \right] / \omega\omega'\omega'' + \frac{\left[|\Phi(q-q-q'')|^2 \; |\Phi(qq''-q)|^2 \; |\Phi(qq-q'')|^2 \right]}{\sinh(x''/2) \; \omega\omega \; \omega''} \right\}$$

$$G^*_{qq'} = -\hbar\pi/16N \sum_{q''} \left[|\Phi(qq'-q'')|^2 - |\Phi(q-q'-q'')|^2 \right. \tag{36}$$

$$\left. - |\Phi(qq''-q')|^2 \right] / (\sinh(x''/2) \; \omega\omega' \; \omega'')$$

Since $G^*_{qq'}$ is real and symmetric, it must possess a set of orthonormal eigenvectors in which n_q can be expanded in an attempt to solve Equation 35. In general, the eigenstates of G^* are not known, but it is obvious that $G^*=N^*+R^*$, where N^* is the N-process collision operator and R^* is the U-process operator. Some eigenstates of N^* are known, however, namely those of zero eigenvalue.[64] These eigenstates derive from phonon distributions which N-type collision do not disturb.

$$N^0_q(\delta T) = [\exp\left(\frac{\hbar\omega}{k_B(T+\delta T)}\right)-1]^{-1} \simeq N^0_q - \frac{\hbar\omega}{k_B T}\frac{\delta T}{T}\frac{1}{4\sinh^2(x/2)},$$

and

$$N^0_q(\vec{c}) = [\exp\left(\frac{\hbar(\omega-\vec{c}\cdot\vec{q})}{k_B T}\right)-1]^{-1} \simeq N^0_q - \frac{\hbar\vec{c}\cdot\vec{q}}{k_B T}\frac{1}{4\sinh^2(x/2)}.$$

The first expression is just the equilibrium distribution at a displaced temperature, while the second is a distribution characteristic of a gas, in thermal equilibrium, but uniformly drifting with velocity $\vec{c}$. Thus, the zero eigenvalue states of N^* are,

$$\eta_0(q) = \lambda_0\,\omega_q/2\sinh(x/2),$$

$$\eta_{1\alpha}(q) = \lambda_{1\alpha}\,q_\alpha/2\sinh(x/2) \qquad (\alpha = 1, 2, 3),$$

where the λ's are normalization constants. These eigenstates are orthogonal in the respect that,

$$\sum_q \eta_0(q)\,\eta_{1\alpha}(q) = 0,$$

$$\sum_q \eta_{1\alpha}(q)\,\eta_{1\beta}(q) = \delta_{\alpha\beta}.$$

As a consequence of energy conservation, R^* , as well as N^*, also does not change $\eta_0(q)$, but η_0 need not be considered since it doesn't give rise to transport (See Equation 19). Likewise, only N^* does not change $\eta_1(q)$ because N-processes conserve crystal momentum, while U-processes do not. We point out that there are other similar distributions of the form $\vec{\lambda}(\vec{G})\cdot(\vec{q}-\vec{G})/2\sinh(x/2)$ which are unaffected by N^*, or by R^* only in the q-subspace for which $\vec{G}$ is the reciprocal vector involved in the three-phonon U-type collision. These distributions are unchanged because the quantity $(\vec{q}-\vec{G})$ is conserved in U-processes involving the reciprocal vector $\vec{G}$. This can easily be seen by rewriting the U-process momentum conservation condition, e.g. $\vec{q} + \vec{q}' - \vec{q}'' = \vec{G} \rightarrow (\vec{q} - \vec{G}) + (\vec{q}' - \vec{G}) - (\vec{q}'' - \vec{G}) = 0$. The above distributions, however, are not independent of η_0 and η_1 and so cannot be used as additional base states in which to expand a solution to the transport equation.

The procedure, then, is to expand n_q^* in terms of the zero-eigenvalue states of N^* according to,

$$n_q^* = \sum_\alpha A_\alpha \eta_{1\alpha}(q) \tag{37}$$

The transport Equation 35 is then used to find the coefficients A_α so that n_q^* is determined, and the thermal conductivity evaluated from the expression for the heat flux,

$$\vec{Q} = \sum \hbar\omega_q \vec{v}_q n_q^*/2\sinh(x_q/2). \tag{38}$$

In order that this procedure be deemed reasonably valid, one must make the following assumptions:[60]

(i) The eigenstates of N^* are complete and span the same vector space as those of G^*.

(ii) The zero-eigenvalue states of N^* are the most important since they will dominate in the inverse of the collision operator. This would be strictly true at low temperatures where $N^* >> R^*$ due to the "freezing out" of Umklapp processes, so that $G^* \to N^*$ and the eigenstates of G^* (say, $|g_i\rangle$) approach those of N^* ($|\eta_i\rangle$). Then, $G^{*-1} = \sum_i 1/g_i \, |g_i\rangle\langle g_i| \to \sum_i 1/\eta_i \, |\eta_i\rangle\langle\eta_i|$, and the zero eigenvalue terms will dominate.

(iii) The states $\eta_{1\alpha}(q)$ exhaust all the zero-eigenvalue states of N^*.

By applying Equation 37 to the transport Equation 35 and the heat flux Equation 38, and employing cubic symmetry, one obtains an expression for the thermal conductivity. The derivation is given in Appendix F and the result is,

$$\kappa(T) = \frac{-k_B}{3\Omega} \sum_q \left[\frac{x_q \, \vec{q}\cdot\vec{v}_q}{4 \sinh^2(x_q/2)} \right]^2 \Bigg/ \sum_{qq'} \frac{(\vec{q}\cdot\vec{q}') \, R^*_{qq'}}{4 \sinh(x/2) \sinh(x'/2)} \qquad (39)$$

Here, again, $x_q = \hbar\omega_q / k_B T$ and Ω is the crystal volume. An examination of this expression reveals that it can be written,

$$\kappa(T) = \frac{-1}{\Omega |\nabla T|^2} \left[\sum_q \eta_{1x}(q)\, \theta_q^* \right]^2 \Big/ \sum_{qq'} \eta_{1x}(q)\, R^*_{qq'}\, \eta_{1x}(q') \quad , \tag{40}$$

where, ∇T is taken to be along the x-axis. In vector notation, Equation 40 becomes,

$$\kappa(T) = \frac{-1}{\Omega |\nabla T|^2} \left[\frac{|\langle \eta_{1x} | \theta^* \rangle|^2}{\langle \eta_{1x} | R^* | \eta_{1x} \rangle} \right] \tag{41}$$

The (negative) quantity in brackets is seen to be identical to the function which is minimized according to the Ziman variational principle,[40] for the case where the trial distribution is taken to be $\eta_{1x}(q)$. Thus, Equation 39 is a greatest lower bound to the true anharmonic thermal conductivity.

b. Numerical Evaluation

To evaluate the expression for the three-phonon contribution to the thermal conductivity, given by Equation 39, we employ the numerical method described here. The numerator of Equation 39 can be computed once the phonon dispersion relations and group velocities have been calculated; the denominator, on the other hand, involves a double sum over the U-type collision operator, which necessitates finding all the Umklapp triplets in the first Brillouin zone of the reciprocal space of the lattice.

The crystal structure of solid Ar is fcc, with one atom/unit cell. Thus, the reciprocal lattice is bcc, and the first Brillouin zone is a truncated octahedron, shown in Figure 6. Due to cubic symmetry, a function of a wavevector need be evaluated only in a 1/48th irreducible section of the first zone (IBZ) , since its value at any other equivalent

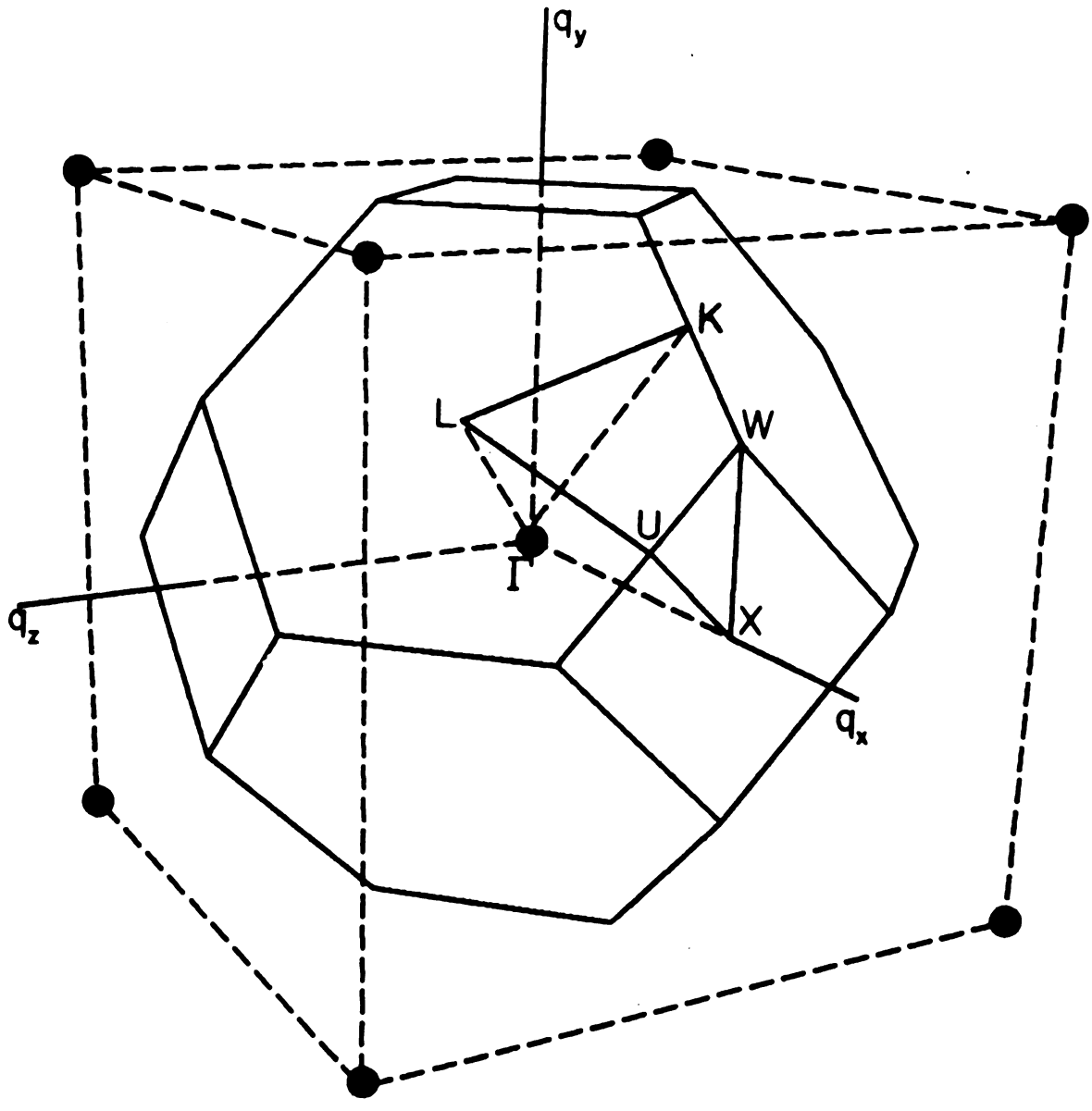

Figure 6: The first Brillouin zone of a fcc crystal lattice, illustrating a 1/48th irreducible section.

point can be found by application of the appropriate cubic symmetry operations (e.g. ω_q is a scalar function of all equivalent points in the zone, while $\vec{v}_q$ is a vector function of the same).

The 1/48th irreducible section we have chosen for evaluation of the eigenfrequencies, polarization vectors, and phonon group velocities is indicated in Figure 6. The wavevectors within this section are chosen to form a cubic grid and take on the values,

$$\vec{q} = 2\pi/a_o n_m \ (n_x, n_y, n_z) \tag{42a}$$

where,

$$n_m \geq n_x \geq n_y \geq n_z \tag{42b}$$

and,

$$n_x + n_y + n_z \leq 3/2 \ \ n_m \tag{42c}$$

In Equation 42, n_m is the number of wavevectors along the positive x-axis, and determines how coarse or fine the wavevector grid is (the equivalent number of wavevectors in the entire zone is given by $4\ n_m^3$). The conditions given by Equations 42b and 42c simply stipulate that $\vec{q}$ remain within the 1/48th section chosen.

The eigenfrequencies ω_q and polarization vectors $\vec{e}_q$ of the crystal lattice are then calculated at each grid point by solving the eigenvalue Equation 11b, with the dynamical matrix $D(\vec{q})$ evaluated for a given interatomic potential. The cartesian components of the phonon group velocities are then computed by using the method employed by Gilat and Dolling.[76] In this technique, perturbation theory is applied to the dynamical matrix in order to find the change in the phonon frequency for small displacements about a given wavevector grid point. For example, to find the γ-th cartesian component of the phonon group

velocity at grid point $\vec{q}$, and for the polarization state s , one forms the perturbed dynamical matrix elements,

$$\delta D^{(\gamma)}_{\alpha\beta}(\vec{q}) = D_{\alpha\beta}(\vec{q} + \delta q_\gamma) - D_{\alpha\beta}(\vec{q})$$

where δq_γ is a small wavevector displacement (we used 1% of the grid cell edge $2\pi/a_o n_m$) in the γ-th direction. Then, to first order, the change in the phonon frequency is,

$$\delta(\omega^2_{\underset{\sim}{q}s}) = \sum_{\alpha\beta} e^{\alpha}_{\underset{\sim}{q}s} \, \delta D^{(\gamma)}_{\alpha\beta} \, e^{\beta}_{\underset{\sim}{q}s} \tag{43}$$

where the $\vec{e}_{\underset{\sim}{q}s}$ are the (previously obtained) polarization vectors (the eigenvectors of the dynamical matrix at point $\vec{q}$).

Then, from Equation 43, the γ-th component of the group velocity is,

$$v^{\gamma}_{\underset{\sim}{q}s} = \sum_{\alpha\beta} \frac{e^{\alpha}_{\underset{\sim}{q}s} \; D^{(\gamma)}_{\alpha\beta} \; e^{\beta}_{\underset{\sim}{q}s}}{2 \, \omega_{\underset{\sim}{q}s} \, \delta q_\gamma} \tag{44}$$

Gilat and Dolling verified this method to be much faster than rediagonalizing the dynamical matrix, and found the first order term to be a very good approximation, even where degeneracies arise from symmetry requirements (except along the [111] symmetry direction,(the Γ-L line in Figure 4) in which case we find the velocity along this axis by subtracting frequencies for successive grid points, and dividing by the grid point separation).

With the above information computed and stored in the computer, we could then evaluate the numerator of Equation 39 by straight forward summation over the wavevectors of the IBZ , with care to properly weight the results for those wavevectors which lie on symmetry lines, planes, or on the surfaces of the first zone (these wavevectors possess

a weight less than 48 since the volume of their cubic grid cells is shared by other sections of the first zone, or by other zones). In replacing a full zone wavevector sum of a function $f(\vec{q})$, $\sum_{\vec{q}} f(\vec{q})$, by one over a grid, $\sum_{\vec{q}}^{\text{grid}} f(\vec{q})$, one has,

$$\sum_{\vec{q}} f(\vec{q}) \rightarrow \frac{\Omega}{(2\pi)^3} \int_{BZ} d^3q\, f(\vec{q}) \rightarrow \frac{\Omega}{(2\pi)^3} \sum_{\vec{q}}^{\text{grid}} \int_{\text{cell}}^{\text{grid}} d^3q'\, f(\vec{q}').$$

The second expression above is the familiar integral representation of the wavevector sum, where $\Omega/(2\pi)^3$ is the density of points in reciprocal space. The grid cell integration is performed over the cubic cell of edge $2\pi/a_o n_m$, which is centered on the grid point $\vec{q}$. If the grid is chosen sufficiently fine that $f(\vec{q})$ does not vary much over a grid cell volume, then the grid cell integral becomes,

$$\int_{\text{cell}}^{\text{grid}} d^3q'\, f(\vec{q}') \simeq f(\vec{q}) \int_{\text{cell}}^{\text{grid}} d^3q' = f(\vec{q})\ (2\pi/a_o n_m)^3 ,$$

where $f(\vec{q})$ is evaluated at the grid point $\vec{q}$. Furthermore, since the crystal volume Ω is $Na_o^3/4$ (there are 4 atoms/unit cell in an fcc lattice), and the total number of wavevectors in the first zone is N, one has the result,

$$\sum_{\vec{q}} f(\vec{q}) \rightarrow N/4n_m^3 \sum_{\vec{q}}^{IBZ} W(\vec{q})\ f(\vec{q}). \tag{45}$$

Here, $W(\vec{q}) \leq 48$ is the weight of the grid point $\vec{q}$ in the 1/48th zone, according to the number of symmetry operations of the type vector of $\vec{q}$.[77] Thus, the numerator of Equation 39, expressed in computational form, is

$$[N/4n_m^3 \sum_{\vec{q}} W(\vec{q}) \sum_{s=1}^{3} x_{\underset{\sim}{qs}}\ (\vec{q}\cdot\vec{v}_{\underset{\sim}{qs}})/4\sinh^2(x_{\underset{\sim}{qs}}/2)]^2 \tag{46}$$

At an intermediate temperature, a grid with $n_m=6$ yielded a computed value of Equation 46 to within 5% of the converged value, obtained for $n_m \geq 12$. Thus, a grid with $n_m=12$ was chosen. With $n_m=12$, the number of wavevector grid points in the 1/48th irreducible zone is 240, resulting in the equivalent number 6912 in the entire zone.

Evaluation of the denominator of Equation 39, which is,

$$\sum_{\underset{\sim}{qs}} \sum_{\underset{\sim}{q's'}} (\vec{q}\cdot\vec{q}') \, R^*_{\underset{\sim}{qs}\underset{\sim}{q's'}}/4 \, \sinh(x_{\underset{\sim}{qs}}/2) \, \sinh(x_{\underset{\sim}{q's'}}/2), \tag{47}$$

requires the following:

(i) Wavevector conservation of the form $\vec{q} \pm \vec{q}' \pm \vec{q}'' = \vec{G}$, with $\vec{G}=0$ excluded.

(ii) Energy conservation $|\omega_{\underset{\sim}{qs}} \pm \omega_{\underset{\sim}{q's'}} \pm \omega_{\underset{\sim}{q''s''}}| \leq A(q,q')$. $A(q,q')$ is a positive function of $\vec{q},s$ and $\vec{q}',s'$, which is non-zero owing to the relatively coarse discreteness of the wavevector grid. It, in effect, allows deviation of the values of $\omega_{\underset{\sim}{qs}}$ and $\omega_{\underset{\sim}{q's'}}$ about their grid point values in proportion to the size of a grid cell, and to the rate of change of the frequencies within their grid cell. If the above condition is satisfied for a given set of frequencies, then the entire computed result of Equation 47 for that set is weighted by a function $S(z)$, where $z = |\omega_{\underset{\sim}{qs}} \pm \omega_{\underset{\sim}{q's'}} \pm \omega_{\underset{\sim}{q''s''}}|$, which is found by double integration of the singular energy delta function over the grid cells at $\vec{q}$ and $\vec{q}'$.

$$S(z) = \iint_{\substack{\tilde{q}\tilde{q} \\ \text{cells}}} d^3q_1 d^3q_2 \; \delta(z) / \iint d^3q_1 d^3q_2$$

A more detailed description of this procedure and a typical integral $S(z)$ are discussed in Appendix G.

(iii) Evaluation of the quantity,

$$\frac{|\Phi(q \pm q' \pm q'')|^2}{\omega_q \omega_{q'} \omega_{q''} \sinh(x_q/2) \sinh(x_{q'}/2) \sinh(x_{q''}/2)} ,$$

where $\Phi(qq'q'')$ is computed for a given interatomic potential according to Equation 28.

All the wavevector triplets satisfying condition (i) could be determined once and for all by performing a 1/48th zone sum over $\vec{q}$ and a full zone sum over $\vec{q}$, with each $\vec{q}$ generated by symmetry group operations on its IBZ type vector. This procedure required the first three shells of reciprocal wavevectors $\vec{G}$, since this set of 26 exhausts all the reciprocal vectors which can transform sums of pairs of wavevectors in the first BZ back to the first BZ. The resulting 15,926 Umklapp triplets (corresponding to a total equivalent number 515,760 in the entire zone) were then stored on a data file for future reference.

It is noted that, for computational purposes, Equation 47 can be written,

$$(N/4n_m^3)^2 \sum_{\tilde{q}\tilde{q}'}^{IBZ} \sum_{ss'} W(\vec{q}) \left[\frac{|\vec{q}|^2 R^*_{qq}}{4 \sinh^2(x_q/2)} + \left(\frac{|\vec{q}'|^2 R^*_{q'q'}}{4 \sinh^2(x_{q'}/2)} + \frac{2(\vec{q}\cdot\vec{q}') R^*_{qq'}}{4 \sinh(x_q/2) \sinh(x_{q'}/2)} \right) (1-\delta_{\tilde{q}\tilde{q}'}) \right] ,$$

due to the symmetry of $R^{*}_{qq'}$. Here the summation $\sum_{q \gtrsim q'}^{IBZ}$ implies that, according to some systematic labeling of the wavevectors in the 1/48th irreducible zone, $\vec{q}'$ is chosen less than or equal to $\vec{q}$; then symmetry group operations are performed on $\vec{q}'$ to generate all wavevectors of its type in the entire zone.

Following the above procedure, we obtain numerical results for the three-phonon contribution to the thermal conductivity according to the present model. Within the validity of this approach, we may examine the temperature dependence of κ , as well as its sensitivity to different models for the interatomic potential. In addition, within the accuracy resulting from quasi-harmonic lattice frequencies, we can draw quantitative information regarding the volume dependence of κ. This results from the fact that, in the quasi-harmonic approximation, zero-point motion and anharmonicity are roughly accounted for by evaluating the derivatives of the interatomic potential at the equilibrium interatomic separation, which results in a minimum crystal free energy, rather than crystal potential energy. Then, the effect of thermal expansion is to shift the lattice mode frequencies, which in turn, is reflected in the value of the thermal conductivity.

De Wette, Fowler, and Nijboer[80], and others, have calculated several thermodynamic properties of solid Ar within the context of the quasi-harmonic approximation, using the analytically simple Lennard-Jones pair potential. Their results verify this to be a reliable method up to temperatures of about half the melting temperature. Above this temperature it appears the more sophisticated theories of linear response or self-consistent phonons are needed to properly account for anharmonicity.[81] However, in view of the limitations of

the present thermal conductivity model at the higher temperatures, an effort along these lines seems unwarranted in this case.

Before proceeding to the results of these calculations, we discuss briefly the model interatomic potentials used, and the form in which they are utilized for calculation of the dynamical matrix, Equation 11a, and of the quantity $\Phi(qq'q'')$, Equation 28.

The reviews of Pollack[4] and Horton[61] have discussed in detail the various potential models for rare gas solids, and their applicability to the description of bulk properties. The simplest and traditionally the most widely used of these has been the Mie--Lennard-Jones (M-L-J) pair potential, given by

$$\phi(r) = \frac{mn\varepsilon}{m-n} [1/m \ (\sigma/r)^m - 1/n \ (\sigma/r)^n].$$

The meanings of r,σ and ε are explained in Figure 7.

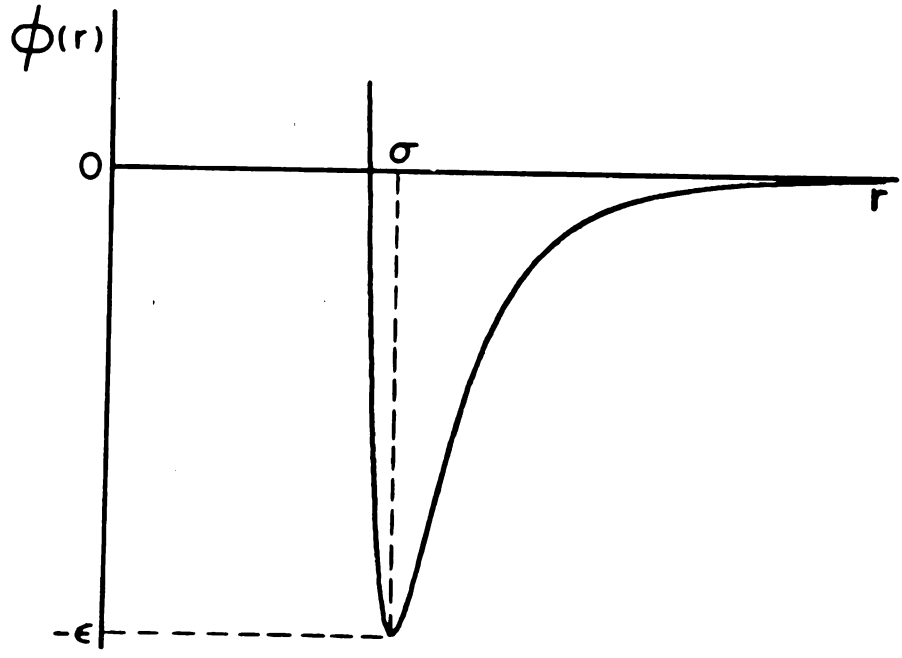

Figure 7: A two-body interatomic potential $\phi(r)$, shown as a function of the interatomic separation r. The meanings of σ and ε are illustrated.

One always chooses n=6 to depict the van der Waals attraction of two widely separated closed shell atoms (the induced dipole-dipole interaction originally calculated quantum mechanically by London). The value m=12 is usually chosen to simulate the charge cloud overlap repulsive force at close distances, since it results in the best agreement of $\phi''(\sigma)$ with experiment.[83] The quantities ε and σ are then chosen to give best agreement with observed solid state properties. Thus, these parameters have no fundamental theoretical foundation, but rather are "effective" parameters which may result in adequate description of only the bulk properties from which they are derived. In fact, that the M-L-J potential is but a phenomenological model for the true pair potential is evident from its completely inadequate description of the temperature dependence of second virial coefficient gas data.[82]

Since the M-L-J potential is known to exaggerate the effect of all but the nearest atoms in a solid[83] it has often been practice to choose the parameters ε and σ to appropriately depict a solid which interacts only through nearest neighbor forces.

For the choice n=6, m=12, the M-L-J pair potential has the form,

$$\phi(r) = \varepsilon[(\sigma/r)^{12} - 2\,(\sigma/r)^{6}]. \qquad (48)$$

The parameters ε and σ have been determined for both the case of first-and all-neighbor interactions, such as to best describe the observed sublimation energy and crystal-lattice spacing at 0^{o} K:[61]

All-neighbor interactions: $\varepsilon/k_B = 119.5$ K

$\sigma = 3.82$ A

First-neighbor interactions: $\varepsilon/k_B = 168.1$ K

$\sigma = 3.709$ A

The pair potential of Barker and Pompe (B-P)[57] is more commensurate with the expected theoretical form of closed-shell atomic interactions. This potential has the form,

$$\phi(r) = [\exp(\alpha(1-r/\sigma)) \sum_{i=0}^{L} A_i (r/\sigma-1)^i - \sum_{i=0}^{2} \frac{C_{2i+6}}{\delta+(r/\sigma)^{2i+6}}]. \quad (49)$$

Here, ε and σ have the same meaning as in Figure 7. The first terms in Equation 49 are consistent with quantum mechanical calculations which suggest the product of an exponential function and a polynomial at overlap distances. The second terms are meant to describe the (negative) asymptotic forces, with the r^{-6} term being the dominant van der Waals interaction at large separations. The small quantity δ is included to suppress the divergence at small r .

Barker and Pompe determined the constants in Equation 49, with L=3, such that this potential function was consistent with pair data (molecular beam data, quantal calculations, second virial gas coefficients, gas transport properties, long-range interaction coefficients), and with third virial gas coefficients and the solid state sublimation energy at 0^o K, all in conjunction with the inclusion of the triple-dipole three-body potential. In this case, the total crystal potential is

$$\Phi(\{r_\ell\}) = 1/2 \sum_{\ell\ell'} \phi(r_{\ell\ell'}) + 1/3! \sum_{\ell\ell'\ell''} \phi(r_{\ell\ell'}, r_{\ell\ell''}, r_{\ell'\ell''}), \quad (50a)$$

where,

$$\phi_3(r_{12},r_{13},r_{23}) = \nu(1 + 3\cos\theta_1\cos\theta_2\cos\theta_3)/(r_{12}r_{13}r_{23})^3 \qquad (50b)$$

is the three-body correction term derived from third-order perturbation theory by Axilrod and Teller.[84] The positive quantity ν is proportional to the static polarizibility of an atom, and the meaning of the other parameters in Equation 50b is illustrated in Figure 8. This triplet potential is thought to be the most important of any many-body interactions in Ar, and has been shown to be absolutely necessary for adequate description of third virial gas coefficients.[57]

By slightly modifying the pair potential Equation 49, (but retaining its applicability to gaseous properties), Bobetic and Barker[21] were able to accurately predict several temperature dependent properties of solid Ar (specific heat, thermal expansion, bulk modulus) at low temperatures.

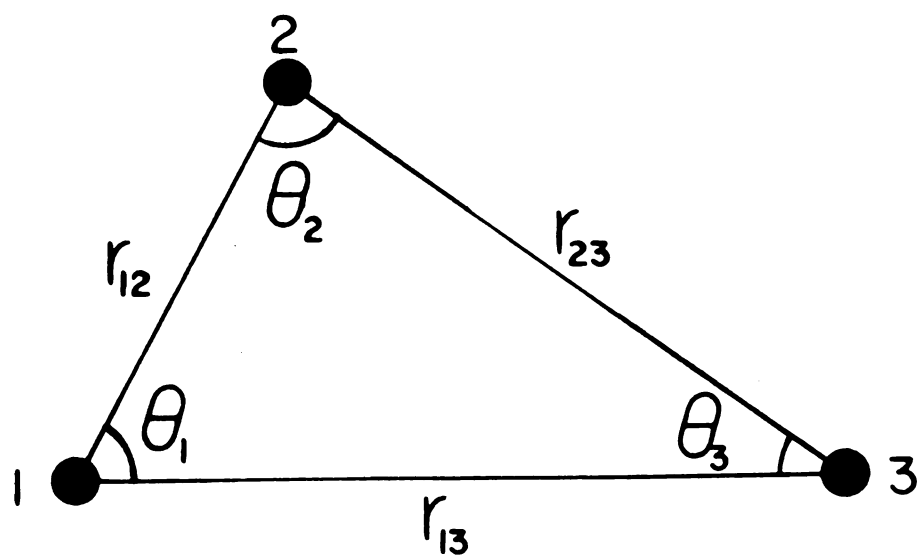

Figure 8: A triplet of atoms, illustrating the meanings of the parameters in Equation 50b.

Their parameters for Equation 49 and 50b are given here:

$$\varepsilon/k_B = 140.23 \text{ K}, \quad \sigma = 3.7630 \text{ A}, \text{ and for } L = 5,$$

$$A_o = 0.29214, \; A_1 = -4.41458, \; A_2 = -7.70182, \; A_3 = -31.9293,$$

$$A_4 = -136.026, \; A_5 = -151.000, \; C_6 = 1.11976, \; C_8 = 0.171551,$$

$$C_{10} = 0.013747, \; \alpha = 12.5, \; \delta = 0.01, \text{ and } D = 73.2 \times 10^{-84} \text{ erg cm}^9.$$

For visual comparison, Figure 9 illustrates the Barker-Pompe (B-P) pair potential, along with the M-L-J all-neighbor potential. Assuming the B-P potential to be the more realistic, once can observe the effect whereby the minimum of the M-L-J potential must be set artificially shallow in order to compensate for a too negative potential interaction at intermediate distances.

Computation of the dynamical matrix $D(\vec{q})$ and the three-phonon coupling constants $\Phi(qq'q'')$ require the second and third order coefficients in the Taylor series expansion of the total crystal potential, e.g.

$$\frac{\partial^2 \Phi(\{\vec{R}_\ell\})}{\partial R^\alpha_{\ell\ell'} \, \partial R^\beta_{\ell\ell'}} \quad \text{and} \quad \frac{\partial^3 \Phi(\{\vec{R}_\ell\})}{\partial R^\alpha_{\ell\ell'} \, \partial R^\beta_{\ell\ell'} \, \partial R^\gamma_{\ell\ell'}} .$$

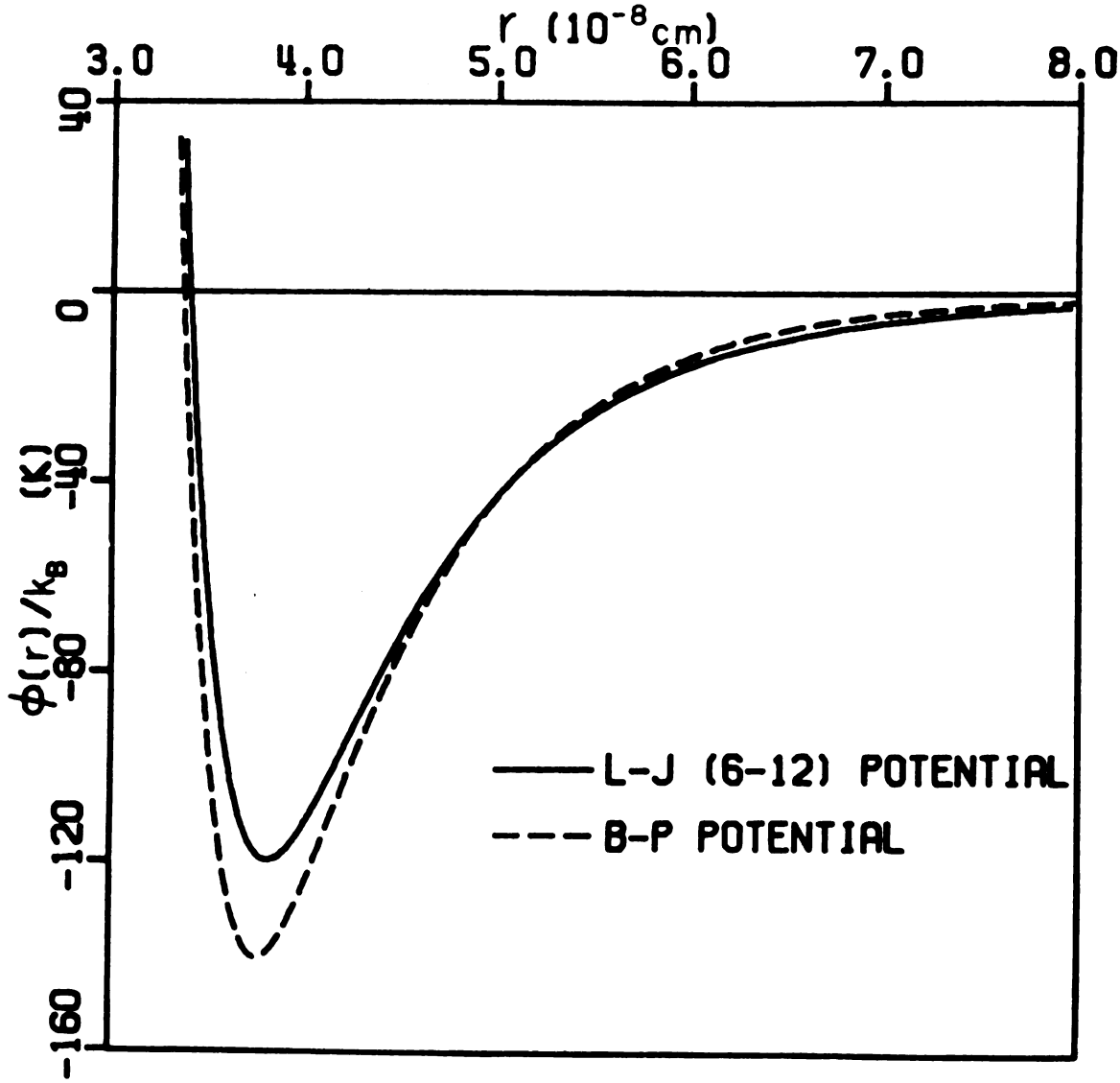

Figure 9: The pair potential $\phi(r)$, according to the models of Lennard-Jones, and Barker and Pompe.

For the case where $\Phi(\{\vec{R}_\ell\})$ is the sum of pair interactions, $\Phi(\{\vec{R}_\ell\}) = 1/2 \sum_{\ell\ell'} \phi(r_{\ell\ell'})$, this reduces to evaluating the quantities,

$$\phi_{\alpha\beta}(R_{\ell\ell'}) = \frac{\partial^2\phi(R_{\ell\ell'})}{\partial R^{\alpha}_{\ell\ell'}\,\partial R^{\beta}_{\ell\ell'}} = \frac{R^{\alpha}_{\ell\ell'} R^{\beta}_{\ell\ell'}}{R^2_{\ell\ell'}} [\phi''(R_{\ell\ell'}) - \frac{\phi'(R_{\ell\ell'})}{R_{\ell\ell'}}] + \delta_{\alpha\beta} \frac{\phi'(R_{\ell\ell'})}{R_{\ell\ell'}}, \quad (51a)$$

$$\phi_{\alpha\beta\gamma}(R_{\ell\ell'}) = \frac{\partial^3\phi(R_{\ell\ell'})}{\partial R^{\alpha}_{\ell\ell'}\,\partial R^{\beta}_{\ell\ell'}\,\partial R^{\gamma}_{\ell\ell'}} = \frac{R^{\alpha}_{\ell\ell'} R^{\beta}_{\ell\ell'} R^{\gamma}_{\ell\ell'}}{R^3_{\ell\ell'}} [\phi'''(R_{\ell\ell'}) - 3\frac{\phi''(R_{\ell\ell'})}{R_{\ell\ell'}} + 3\frac{\phi'(R_{\ell\ell'})}{R^2_{\ell\ell'}}] \quad (51b)$$

$$+ (\delta_{\alpha\beta} R^{\gamma}_{\ell\ell'} + \delta_{\alpha\gamma} R^{\beta}_{\ell\ell'} + \delta_{\beta\gamma} R^{\alpha}_{\ell\ell'}) \frac{(\phi'' - \phi'/R_{\ell\ell'})}{R^2_{\ell\ell'}} .$$

Here, the primed ϕ's are derivatives with respect to the equilibrium atomic separation $R_{\ell\ell'}$. Analytical expressions for ϕ', ϕ'', and ϕ''' are obtained by straight forward differentiation of a particular model potential. In Appendix H we present expressions for these derivatives for the case of the M-L-J (6-12) potential and the B-P pair potential.

The three-body contribution to the total crystal potential,

$$\Phi_3(\{r_\ell\}) = 1/3! \sum_{\ell\ell'\ell''} \phi_3(r_{\ell\ell'}, r_{\ell\ell''}, r_{\ell'\ell''}),$$

is somewhat more difficult to utilize for lattice dynamical computations, since it does not result in as simple expressions for the potential derivatives, as does the two-body potential, as in the Equation 51. For example, in making the transition to the convenient relative coordinates $R_{\ell\ell'}$, one has for the second order coupling constant of the two-body potential,

$$\frac{\partial^2\phi(R_{\ell\ell'})}{\partial R^{\alpha}_{\ell}\,\partial R^{\beta}_{\ell'}} = \frac{\partial^2\phi(R_{\ell\ell'})}{\partial R^{\alpha}_{\ell\ell'}\,\partial R^{\beta}_{\ell\ell'}} ,$$

whereas, for the three-body potential, this becomes,

$$\frac{\partial^2 \phi_3(R_{\ell\ell'}, R_{\ell\ell''}, R_{\ell'\ell''})}{\partial R_{\ell}^{\alpha} \partial R_{\ell'}^{\beta}} = - \frac{\partial^2 \phi_3}{\partial R_{\ell\ell'}^{\alpha} \partial R_{\ell\ell'}^{\beta}} - \frac{\partial^2 \phi_3}{\partial R_{\ell\ell''}^{\alpha} \partial R_{\ell\ell'}^{\beta}}$$

$$+ \frac{\partial^2 \phi_3}{\partial R_{\ell\ell'}^{\alpha} \partial R_{\ell'\ell''}^{\beta}} + \frac{\partial^2 \phi_3}{\partial R_{\ell\ell''}^{\alpha} \partial R_{\ell'\ell''}^{\beta}} .$$

The additional (mixed) terms result from the dependence of the values of two of the interatomic separations of a triplet of atoms, on the displacements of a third.

The triplet potential ϕ_3 can be written in the form,

$$\phi_3(r_{\ell\ell'}, r_{\ell\ell''}, r_{\ell'\ell''}) = [z_{\ell\ell'} z_{\ell\ell''} z_{\ell'\ell''} + 3/8 \, Z_1 Z_2 Z_3](z_{\ell\ell'} z_{\ell\ell''} z_{\ell'\ell''})^{-5/2},$$

where, $z_{\ell\ell'} = r_{\ell\ell'}^2$, etc., and,

$$Z_1 = z_{\ell\ell'} + z_{\ell\ell''} - z_{\ell'\ell''}$$

$$Z_2 = z_{\ell\ell''} + z_{\ell'\ell''} - z_{\ell\ell'}$$

$$Z_3 = z_{\ell'\ell''} + z_{\ell\ell'} - z_{\ell\ell''}$$

In terms of derivatives with respect to the appropriate variables, $z_{\ell\ell'}$, $z_{\ell\ell''}$, and $z_{\ell'\ell''}$ one obtains for the three-body contribution to the components of the dynamical matrix,

$$D_{\alpha\beta}^{(3)}(\vec{q}) = 2/m \sum_{\ell'\ell''}{}' [4 \, R_{\ell\ell'}^{\alpha} R_{\ell\ell'}^{\beta} \frac{\partial^2 \phi_3}{\partial z_{\ell\ell'}^2} + 2 \, \delta_{\alpha\beta} \frac{\partial \phi_3}{\partial z_{\ell\ell'}} + 4 \, R_{\ell\ell'}^{\beta} R_{\ell\ell''}^{\alpha} \frac{\partial^2 \phi_3}{\partial z_{\ell\ell'} \partial z_{\ell\ell''}}$$

$$+ 4 \, R_{\ell\ell'}^{\alpha}(R_{\ell\ell'}^{\beta} - R_{\ell\ell''}^{\alpha}) \frac{\partial^2 \phi_3}{\partial z_{\ell\ell'} \partial z_{\ell'\ell''}} + 4 \, R_{\ell\ell''}^{\alpha}(R_{\ell\ell'}^{\beta} - R_{\ell\ell''}^{\alpha}) \frac{\partial^2 \phi_3}{\partial z_{\ell\ell''} \partial z_{\ell'\ell''}}] \sin^2(\vec{q} \cdot \vec{R}_{\ell\ell'}/2).$$

Analytic expressions for the various potential derivatives which appear in the above expression are given in Appendix H.

c. Results

In Figure 10 and Table 2 we present the results of numerical calculations of the temperature dependent three-phonon thermal conductivity according the the previously described model. These computations were performed using the Control Data Corporation 6500 digital computer at Michigan State University.

Figure 10 illustrates the effect on $\kappa(T)$ of the particular form of the interatomic potential model used to determine the lattice frequencies and anharmonic coupling constants. All these theoretical data are calculated for a crystal density corresponding to that at 0 K (molar volume = 22.55 cm^3/mole). For each interatomic potential model, the calculations are seen to yield the characteristic T^{-1} behavior for $T \gtrsim 20$ K. Thus, for Ar the general criterion that $T \gtrsim \Theta_D$ ($\Theta_D \simeq 85$ K) for this dependence is somewhat relaxed, and extends down to about $\Theta_D/4$. From the expression for the three-phonon conductivity, Equation 39, and from Equations 46, 47, and 36, one can obtain an approximate analytic expression for $\kappa(T)$ in the high T limit. This is accomplished by taking small argument limits of the hyperbolic functions in Equations 36, 39, 46, and 47, and by employing reduced, dimensionless variables according to:

$$\vec{q} \rightarrow \vec{q}/(2\pi/a_o n_m)$$

$$\omega \rightarrow \omega/\omega_0 \; ; \; \omega_0 = \sqrt{2\phi''/m}$$

$$\phi_{\alpha\beta}(R_{\ell\ell'}) \rightarrow \phi_{\alpha\beta}(R_{\ell\ell'})/\phi''$$

$$\phi_{\alpha\beta\gamma}(R_{\ell\ell'}) \rightarrow \phi_{\alpha\beta\gamma}(R_{\ell\ell'})/\phi'''$$

$$\vec{v}_q \rightarrow \vec{v}_q \, \omega_0 (2\pi/a_o n_m)^{-1}.$$

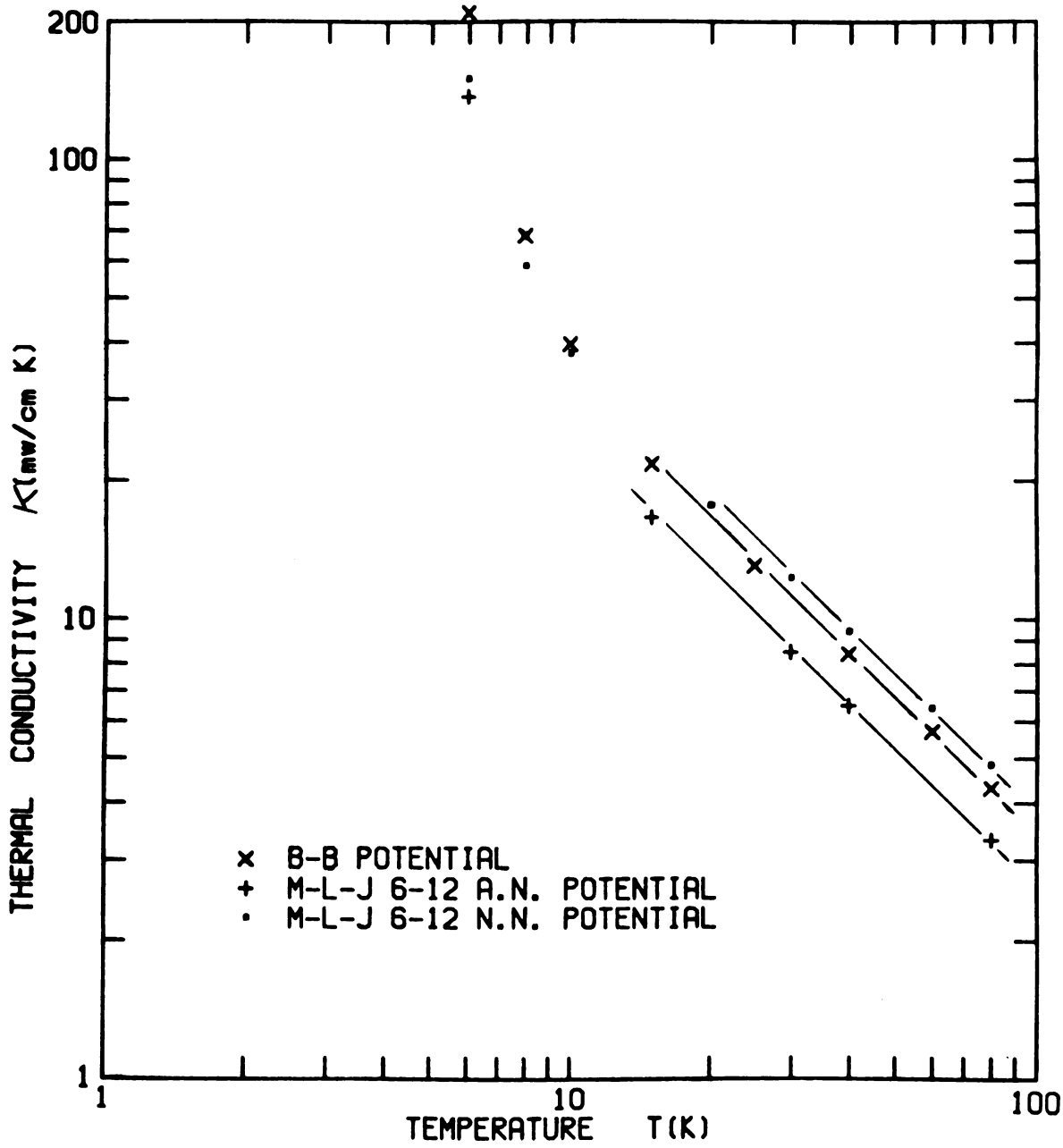

Figure 10: A plot of the three-phonon thermal conductivity $\kappa(T)$, illustrating the effect of the interatomic potential used. The potential models employed are the Mie--Lennard-Jones (6-12) all-neighbor and nearest-neighbor pair potentials, and the Bobetic and Barker pair potential with the triple-dipole three-body correction.

TABLE 2

Theoretical Three-Phonon Thermal Conductivity

Temperature T(K)	Thermal Conductivity $\kappa(T)$ (mw/cm K)	
5.0	387.48	
6.0	150.95	
8.0	58.91	Mie--Lennard-Jones A.N. Potential 0 K Density
10.0	38.15	
20.0	17.86	
30.0	12.40	
40.0	9.49	
60.0	6.44	
80.0	4.86	
6.0	138.57	
15.0	16.92	Mie--Lennard-Jones Potential 0 K Density
30.0	8.59	
40.0	6.55	
80.0	3.35	
5.0	598.39	
6.0	211.15	
8.0	69.00	Bobetic-Barker Potential with Triple-Dipole Correction 0 K Density
10.0	40.05	
15.0	22.02	
25.0	13.24	
40.0	8.49	
60.0	5.75	
80.0	4.34	
20.0	16.11	
40.0	7.14	Bobetic-Barker Potential with Triple-Dipole Correction Equilibrium Density
60.0	3.90	
80.0	2.18	

In these expressions, the quantities ϕ'' and ϕ''' are potential derivatives evaluated at the nearest-neighbor separation. After some straight forward algebra, one obtains for the thermal conductivity under the high T conditions,

$$\kappa(T) = C\,\phi''^{7/2}\,\phi'''^{-2}\,m^{-1/2}\,a_o^{-1}\,T^{-1}.$$

The parameter C involves constants and sums, subject to momentum and energy conservation, over non-dimensionalized phonon curves. This quantity may be evaluated once and for all for use in the high T limit. Listed below are the values of C which we calculated for the three potential models used.

B-B potential: C = 12.07

M-L-J A.N. potential: C = 8.12

M-L-J N.N. potential: C = 20.22

For the case of nearest-neighbor interactions only, C fails to be independent of the particular potential model only through the appearance of terms in $\frac{\phi'}{r_o\phi''}$ and $\frac{3\phi''}{r_o\phi'''}$, which are generally of relative magnitude approximately 10^{-3} - 10^{-2} and 10^{-1} respectively. For the all-neighbor potentials, however, there appear also in C terms involving ratios in which the numerator and denominator are potential derivatives of the same order. For this case, however, the numerators are evaluated at higher order neighbor distances than the denominators; the latter as before are evaluated at the N.N. separation. A typical such term, for example, is $\phi''(2N.)/\phi'' \simeq 0.03$. Based upon these small corrections, then, one would anticipate that the values of C for the different potentials should be very nearly the same. But, in fact, they are not.

The reason for this disparity lies in the large effect on the number of Umklapp triplets, satisfying the energy conservation conditions, which is caused by only small shifting in the relative values of the phonon energies of different branches. Such small shifts result from the shape of the interatomic potential. These small relative shifts arise from the effects of the small terms, discussed in the preceding paragraph, on the dynamical matrix. For example, the average contribution to the thermal resistivity per three-phonon process at 80 K differs by only three parts in 1000 between the B-B and M-L-J A.N. potentials. However, the absolute number of three-phonon processes occuring for the M-L-J A.N. potential is larger by a factor of 1.24, accounting for the observed differences in the thermal conductivities. This effect is even more striking for the case of the M-L-J N.N. potential, which gives an average resistivity per three-phonon process which is about 1.276 times larger then that of the B-B or M-L-J A.N. potentials, while the number of processes is only 0.54 that of the M-L-J A.N. potential. We emphasize that this effect would not be anticipated or included in any over-simplified model for heat transport, and must be detected only by detailed analysis of the interaction processes.

For the M-L-J and B-B all-neighbor potentials, the first 10 inequivalent shells of atoms were found to be adequate for the evaluation of the lattice frequencies and phonon group velocities. However, for computation of the phonon scattering rates, which involve the quantity $\Phi(qq'q'')$ given by Equation 28, the inclusion of more than two shells resulted in the use of a prohibitive amount of computer time.

Fortunately, the computed value of thermal conductivity was found to be identical, to within one part in 1000, for the use of N.N. and of first and second N. N. Detailed examination of the anharmonic coupling constants $\Phi(qq'q'')$ revealed that this phenomenon was attributable to cancellation of errors, since the effect of the neglect of more distant atomic shells was to sometimes increase and sometimes decrease the value of $\Phi(qq'q'')$ for different Umklapp triplets. In general, the overall effect of the neglect of more distant atomic shells is to slightly decrease the thermal conductivity.

In Figure 11 we have included the present experimental data, along with that of K-M and C-B. These may be compared with the computed thermal conductivities of the B-B potential, including the results obtained in the quasi-harmonic treatment of the effects of thermal expansion. This latter procedure differed from the previous analysis only in the respect that the lattice frequencies were evaluated for a crystal density corresponding to the equilibrium value at a given temperature. For this, we used values of the lattice parameter a_o, obtained by Peterson, Batchelder, and Simmons,[7] which were determined from X-ray diffraction patterns of free-standing single crystals of solid Ar.

It is seen that the theoretical results are, in general, too low, particularly in the intermediate temperature range above the region of the exponential rise in $\kappa(T)$. This is probably the fault of the thermal conductivity model used, since the effect of very rapid normal processes (which are assumed in this model) is to help keep occupied those phonon states which scatter strongly by U-processes, thus contributing to the thermal resistance. In view of this fact, the apparent agreement with the high T experimental data is surprising,

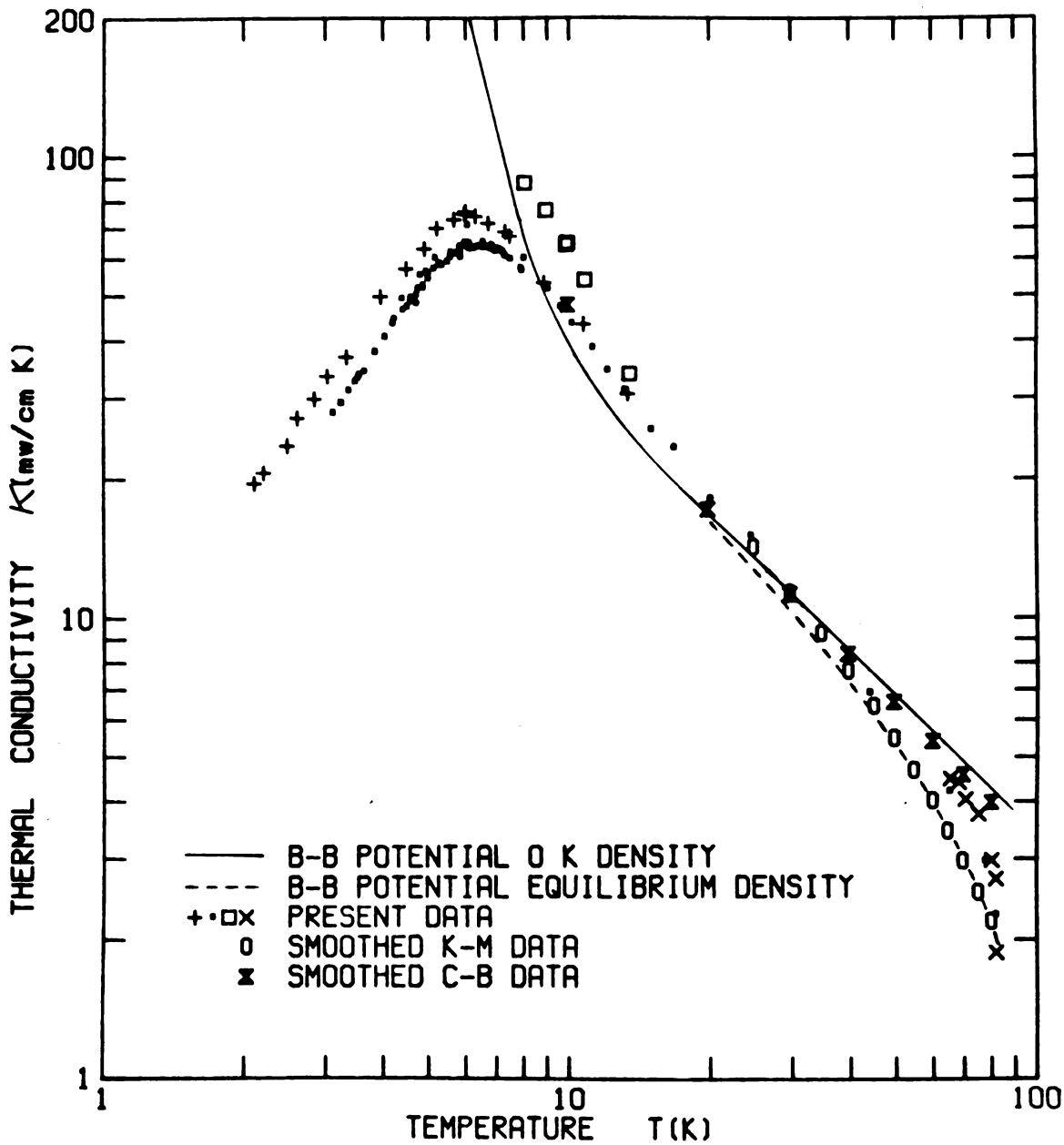

Figure 11: The theoretical three-phonon thermal conductivity obtained from the Bobetic and Barker potential model, evaluated both for a 0 K crystal density, and for the equilibrium density. Included for comparison are the present experimental results, and those of Clayton and Batchelder, and Krupskii and Manzhelii.

since one would expect this model to yield a falsely suppressed thermal conductivity in the high T range. Thus, one must be cautious in assuming that thermal expansivity has completely told the story in the reasonable agreement with the high T data of K-M. Four-phonon processes could conceivably be present, and account for the K-M data being low enough to show apparent agreement with the three-phonon quasi-harmonic calculations. On the other hand, the high T calculations may be higher than a more careful analysis of anharmonic lattice vibrations would yield.

2. Scattering Due to Defects

It was mentioned previously that in the temperature regime where U-type three-phonon processes are prevalent the contribution to the phonon scattering by various types of lattice defects is relatively small. However, at temperatures near and below the onset of the exponential rise in the three-phonon conductivity, the precise behavior of $\kappa(T)$ is determined entirely by the various types crystal defects, impurities, or is limited by the size of the sample. The combined effects of the various types of phonon scattering processes is to depress and shift the peak in $\kappa(T)$ in a manner indicative of the relative strengths of the different scattering mechanisms.

a. Formalism

The role of strain fields in thermal conductivity can be quantitatively assessed only if one has detailed information concerning the nature of the fields, and even then the computational difficulties are formidable. Fortunately, since these effects occur at low temperatures, some of the more usual approximations (such as the assumption of an isotropic, dispersionless medium) are reasonably justified. It is common practice

to manipulate the problem in such a way as to obtain a characteristic phonon lifetime τ_q, which can then be used along with Equation 23 to compute $\kappa(T)$.

Following the perturbation approach similar to that used for three-phonon processes, we present a brief explanation of the origin of strain field phonon scattering, and, in particular, show that it leads to elastic phonon scattering.

The perturbation Hamiltonian for the case of crystal strains is just the change in the crystal potential energy due to a displacement field $\vec{V}_\ell$ in the crystal. This field is the result of either external or internal stresses, and will depend in detail on the specific type of crystal imperfection. In this case, atoms in the presence of the strain field, now occupy instantaneous positions given by,

$$\vec{r}_\ell = \vec{R}_\ell + \vec{V}_\ell + \vec{u}_\ell,$$

where $\vec{u}_\ell$ is now the displacement from the displaced equilibrium position $\vec{R}_\ell + \vec{V}_\ell$. Then, from Equation 8 the harmonic potential becomes,

$$\Phi^{(2)'} = 1/4 \sum_{\ell\ell'} \sum_{\alpha\beta} \phi_{\alpha\beta}(R_{\ell\ell'}) (u^\alpha_{\ell\ell'}+V^\alpha_{\ell\ell'}) (u^\beta_{\ell\ell'}+V^\beta_{\ell\ell'}) \ ,$$

or,

$$\Phi^{(2)'} = \Phi^{(2)} + 1/2 \sum_{\ell\ell'} \sum_{\alpha\beta} \phi_{\alpha\beta}(R_{\ell\ell'}) [V^\beta_{\ell\ell'} u^\alpha_{\ell\ell'} + 1/2 \ V^\alpha_{\ell\ell'} V^\beta_{\ell\ell'}] \ , \qquad (52')$$

where $\vec{V}_\ell = \vec{V}_\ell - \vec{V}_{\ell'}$. Here, $\Phi^{(2)}$ is just the harmonic potential energy when no strain field is present, and the second term represents the strain energy. Neither of the terms of the strain energy scatter phonons since the initial and final states must be the same owing to energy conservation; so these excitations remain normal modes of the crystal, and the harmonic strain potential cannot contribute to thermal resistivity.

Similar examination of the third order crystal potential, however, yields the following result, obtained from Equation 25,

$$\Phi^{(3)'} = \Phi^{(3)} + 1/12 \sum_{\ell\ell'} \sum_{\alpha\beta\gamma} \phi_{\alpha\beta\gamma}(R_{\ell\ell'}) [V^{\alpha}_{\ell\ell'} V^{\beta}_{\ell\ell'} V^{\gamma}_{\ell\ell'} + 3\, V^{\alpha}_{\ell\ell'} V^{\beta}_{\ell\ell'} u^{\gamma}_{\ell\ell'} + 3\, V^{\alpha}_{\ell\ell'} u^{\beta}_{\ell\ell'} u^{\gamma}_{\ell\ell'}] \quad . \tag{53}$$

Of the anharmonic energy terms in Equation 53 arising from the strain field, only those of the form Vuu scatter phonons. Thus the perturbation Hamilitonian to be considered is,

$$\Delta\Phi^{(3)} = 1/4 \sum_{\ell\ell'} \sum_{\alpha\beta\gamma} \phi_{\alpha\beta\gamma}(R_{\ell\ell'})\; V^{\alpha}_{\ell\ell'} u^{\beta}_{\ell\ell'} u^{\gamma}_{\ell\ell'} \quad . \tag{54}$$

Substituting into Equation 54 the normal mode expansion for $\vec{u}_{\ell\ell'}$, Equation 26, one obtains, retaining only the energy conserving terms,

$$\Delta\Phi^{(3)} = \hbar/8mN \sum_{qq'} \sum_{\ell\ell'} \sum_{\alpha\beta\gamma} [\phi_{\alpha\beta\gamma}(R_{\ell\ell'})\; e^{\alpha}_{q} e^{\beta}_{q'} V^{\gamma}_{\ell\ell'}$$

$$\cdot (\exp(-i\vec{q}\cdot\vec{R}_{\ell}) - \exp(-i\vec{q}\cdot\vec{R}_{\ell'}))(\exp(i\vec{q}\cdot\vec{R}_{\ell}) - \exp(i\vec{q}\cdot\vec{R}_{\ell'}))\; a_q a^{\dagger}_{q'}$$

$$+ \text{hermitian conjugate}) \quad .$$

By expressing the displacement field $\vec{V}_{\ell}$ in terms of its Fourier transform,

$$\vec{V}_{\ell} = \sum_{\underset{\sim}{q}} \vec{V}_{\underset{\sim}{q}} \exp(i\vec{q}\cdot\vec{R}_{\ell}) \quad ,$$

one obtains,

$$\Delta\Phi^{3} = \hbar/8mN \sum_{qq'} [C_{q-q'}\, a_q a^{\dagger}_{q'} + C^{*}_{q-q'}\, a^{\dagger}_{q} a_{q'}] \quad ,$$

where,

$$C_{qq'} = \sum_{\ell\ell'}\sum_{\alpha\beta\gamma}\sum_{\tilde{q}''} \phi_{\alpha\beta\gamma}(R_{\ell\ell'})\ v^{\gamma}_{\tilde{q}''} e^{\alpha}_{q} e^{\beta}_{q'} \tag{55}$$

$$\cdot(\exp(i\vec{q}\cdot\vec{R}_{\ell})-\exp(i\vec{q}\cdot\vec{R}_{\ell'}))\,(\exp(i\vec{q}'\cdot\vec{R}_{\ell})-\exp(i\vec{q}'\cdot\vec{R}_{\ell'}))\,(\exp(i\vec{q}''\cdot\vec{R}_{\ell})-\exp(i\vec{q}''\cdot\vec{R}_{\ell'}))\,.$$

From this result the following transition rates,

$$P_{q'\to q} = \pi/32m^2N^2\,|C_{q-q'}|^2\,(N_q+1)\,N_{q'}\,\delta(\omega_q-\omega_{q'}) \quad ,$$

and,

$$P_{q\to q'} = \pi/32m^2N^2\,|C_{q-q'}|^2\,N_q\,(N_{q'}+1)\ \delta(\omega_q-\omega_{q'}) \quad ,$$

which yield the rate of change of the phonon state $\vec{q}s$ due to strain field scattering alone,

$$\dot{n}_q = -\pi/32m^2N^2\sum_{q'}\,|C_{q-q'}|^2\,\delta(\omega_q-\omega_{q'})\ (n_q-n_{q'}) \quad . \tag{56}$$

Therefore, to first order, strain field scattering of phonons is seen to be elastic, and proportional to the square of the Fourier transform of the total strain field (see Equation 55).

In the usual way, one can formally write Equation 56 in terms of a relaxation time τ_q, as,

$$\dot{n}_q = -n_q/\tau_q \ ,$$

where,

$$\tau_q^{-1} = \pi/32m^2N^2\ \sum_{q'}\,|C_{q-q'}|^2\,\delta(\omega_q-\omega_{q'})\,(1-n_{q'}/n_q) \quad . \tag{57}$$

To evaluate this relaxation rate is extremely difficult, since into the quantity $C_{qq'}$, one must put information regarding the nature and precise configuration of the total displacement field due to the combined effect of all strain producing defects. Except for very specialized cases, one does not know the exact number of configuration of strain

producing defects, and must resort to several important approximations. In surveying the work that has been done in this area,[20,43,44,50,69-73] generally several or all of the following simplifying assumptions are made:

(i) The displacement field $\vec{v}_\ell$ is that calculated from classical elastic theory for a particular defect model. This is valid if the extent of the strain field is large compared to the disordered region responsible for the strain.

(ii) Defects are randomly distributed throughout the solid. To a first approximation, this assumption cancels the interference terms in Equation 56 which occur between strain fields of different sources and kinds. Then the phonon scattering rate due to the strain field of a defect of type i is just proportional to the number of defects of that type present in the solid. In this case, one can define a total relaxation time due to all types of defects according to $\tau^{-1} = \sum_i \tau_i^{-1}$. The validity of this assumption is somewhat dubious, since it is well known, for example, that dislocations often occur in arrays, and that point defects interact with edge-type dislocations.[29] This assumption also restricts the values of $\vec{q}''$ in Equation 55 to $\vec{q}-\vec{q}'$ since $\Delta\Phi^{(3)}$ now must be approximately unchanged under a displacement of the entire crystal through a lattice vector $\vec{R}_\ell$.

(iii) Due to low temperature conditions, one normally takes the phonon spectrum to be isotropic and dispersionless (i.e. $\vec{v}_q = \vec{q}\omega_q/q^2$, the Debye approximation). Likewise, since $\vec{q}\cdot\vec{R}_\ell << 1$ for thermal phonons, one takes $\exp(i\vec{q}\cdot\vec{R}_\ell) \simeq 1 + i\vec{q}\cdot\vec{R}_\ell$ in Equation 55, and further restricts the lattice sum to nearest neighbors only. Furthermore, the anharmonic force constant $\phi_{\alpha\beta\gamma}(R_{\ell\ell'})$ may be approximated by the Gruneisen theory as,

$$\phi_{\alpha\beta\gamma}(R_{\ell\ell'}) \simeq 24\gamma\rho v^2 \, R_0^\alpha R_0^\beta R_0^\gamma / R_0^3 \ ,$$

where, γ = Gruneisen's constant

ρ = crystal density

v = velocity of sound

R_0 = nearest neighbor separation.

Finally, integrals over angles are often approximated by r.m.s. values.

Within the context of these simplifying assumptions, expressions for the most common types of strain field scattering rates have been obtained by several workers.[20,43,44,50,73] For the most part, their results are similar, and we list here representative expressions for the most common types of strain field scattering.

Point defects: The presence of a substitutional atom or vacancy in a crystal lattice will introduce a strain field. If the medium is isotropic and elastic, the displacement field is given by,

$$\vec{V}(\vec{r}) = \epsilon r_0^3 \vec{r}/r^3 \ ; \ r > r_0$$

$$= 0 \qquad ; \ r < r_0 \ ,$$

where r_0 is the radius of the impurity atom or vacancy, and εr_0 is the relative atomic misfit (i.e. $V(r_0)=\varepsilon r_0$). For this field, analogous to the electric field of a uniform spherical charge distribution, the Fourier components of $\vec{V}(r)$ are,

$$\vec{V}_q = (4\pi i\, \varepsilon r_0^3 \vec{q}/\Omega q^2)\, \sin(qr_0)/qr_0 \qquad (59)$$

The factor $\sin(qr_0)/qr_0$ is seen to reduce the scattering rate at higher temperatures where $qr_0 > 1$. The low temperature scattering rate, given by Carruthers,[20] is,

$$\tau_{pt}^{-1} = 8\pi\sigma/45\, (g\varepsilon r_0^3/\rho)\, q^4/v^3 \ . \qquad (60)$$

Here, $g \simeq \phi'''-3\phi''/R_0$ (from Equation 51b), σ is the density of scatterers, and ρ and v have the same meaning as in Equation 58. The fact that $\tau_{pt}^{-1} \propto q^4$ (or ω^4) is essentially a consequence of the spherical symmetry of the strain field (analogous to Rayleigh scattering of sound). As was mentioned in Chapter I, at low temperatures $\kappa(T) \propto T^{3-n}$ for $\tau^{-1} \propto q^n$.[86] Thus, if point defects constituted the only departure of an infinite crystal from perfection, then $\kappa(T) \propto T^{-1}$ would diverge as $T \to 0$. Other scattering mechanisms must limit the thermal conductivity at low temperatures.

Dislocations: Results based on the conventional treatment of dislocation strain field phonon scattering are somewhat suspect. First, because of the relatively complicated nature of this strain field, it is essential to limit the treatment to only straight dislocations. In reality, however, dislocations are known to more often occur in clusters, and form spirals, closed loops, or other complicated configurations.[29] Second, even for the case of a straight edge or screw dislocation, the displacement field is long-ranged, casting doubt on the validity of Born approximation techniques.

Klemens[43] approached the problem for the case of simple, straight dislocations, randomly distributed and oriented in the solid, using a Gruneisen-type model for the anharmonic coupling. Carruthers[20] later solved the problem from the more fundamental atomic force constant approach, and obtained the result,

$$\tau_d^{-1} \simeq 2/3\ (\sigma/128\ v^3)(gb\alpha/\rho)^2\, q\ . \qquad (61)$$

In Equation 61, $\alpha = (1-2\nu)/(1-\nu)$, where ν is Poisson's ratio and b is the Burger's vector. Other parameters are as in Equation 60. This result happens to apply for a random array of straight edge dislocations, but, due to the approximations and averaging procedure, the expression for screw dislocations is essentially the same. Of primary importance is the fact that $\tau_d^{-1} \propto q$, so that at low T, a crystal possessing mostly dislocation defects would have $\kappa(T) \propto T^2$.

Ohasi[44] has treated this same problem by the method of Green functions, and also obtained the result $\tau_d^{-1} \propto q$, but with the multiplying constant about 100 times larger than that of Carruthers. At first glance, Ohasi's result seems to partially reconcile the marked discrepancies whereby the dislocation density in Alkali Halide crystals obtained from thermal conductivity measurements, along with Klemens' theory, were as much as a factor of 1000 larger than dislocation densities measured from surface etch pit patterns.[45-47] However, the experimental results of Malinowski and Anderson[85] present a strong argument for an entirely different, and stronger, dislocation phonon scattering mechanism.

In their work, Malinowski and Anderson discovered that the 50% reduction in the low temperature $\kappa(T)$ of a LiF crystal, resulting from application of a shear stress, could be nearly restored by subsequent γ-irradiation of the strained region. This observation is consistent

with a theory of Granato and Lucke,[87] which has to do with the resonant motion of dislocation cores within their equilibrium potential valley between atom rows. In this model, the dislocation loops or segments are pinned at their ends by impurity atoms or point defects. The segments then vibrate as elastic strings, with the resonant frequency determined by the segment length. These mobile dislocations effect strong resonant scattering of thermal transverse phonons, explaining the 50% reduction in $\kappa(T)$, since then most of the remaining heat conduction is due only to the higher frequency modes. Subsequent irradiation of the strained sample presumably creates additional point defects, which pin the dislocation segments at more points, shortening the average segment length, and increasing the resonant frequency. Then the thermal transverse phonons lie in the low frequency tail of the damping curve, and are thus free to conduct energy, restoring the original value of $\kappa(T)$.

This would seem to indicate that the residual phonon scattering, which must be due to the remaining dislocation strain fields, is in fact a smaller effect, more in agreement with the results of Carruthers[20] and Klemens,[43] rather than with those of Ohasi.[44]

Ishioka and Suzuki[88] attempted to compute a scattering cross-section for a simplified model of phonons interacting with a vibrating dislocation. Their calculations are a quantum mechanical extension of those performed by Granato,[89] which were based upon the classical results of Nabarro.[90] Since the model of Ishioka and Suzuki is one of quasi-static dislocation motion, the results are incomplete, and unable to reconcile the differences with experiment, including the T^2 temperature dependence.

There are two other important heat flow resisting mechanisms in insulators at low temperatures. These are the scattering of phonons by

crystal grain boundaries (or the surfaces of the sample), and mass-difference scattering. Although our experimental results indicate these effects to be relatively small in high quality samples prepared from high-purity Argon gas, for completeness we present expressions for the scattering rates for these processes.

Mass-difference scattering: In a pure, non-quantum solid, the existence of atoms of different isotopic mass does not produce strains, so there is no change in the potential energy of the crystal. However, the kinetic energy is modified according to,

$$T = 1/2 \sum_{\ell} m_{\ell} \dot{\underset{\sim}{u}}_{\ell}^2 = 1/2 \sum_{\ell} \bar{m}\, \dot{\underset{\sim}{u}}_{\ell}^2 + 1/2 \sum_{\ell} (m_{\ell}-\bar{m}) \dot{\underset{\sim}{u}}_{\ell}^2 = T_0 + \Delta T \ . \tag{62}$$

Here, $\bar{m} = \sum_{\ell} m_{\ell}/N$ is the average atomic mass of the crystal, and the perturbation energy is $\Delta T = 1/2 \sum_{\ell} (m_{\ell} - \bar{m}) \dot{\underset{\sim}{u}}_{\ell}^2$. Following the same first order transition rate scheme as before, one obtains,

$$\dot{n}_q = -\pi/8m^2N^2 \ \omega_q^2 \sum_{q'} |M_{qq'}|^2 \ \delta(\omega_q - \omega_{q'})(n_q - n_{q'}) \ ,$$

where,

$$M_{qq'} = [\sum_{\ell} \Delta m_{\ell} \exp(i(\vec{q}-\vec{q}')\cdot\vec{R}_{\ell})](\vec{e}_q \cdot \vec{e}_{q'}) \ .$$

Assuming a random array of isotopic impurities, and using the set of simplifying assumptions previously mentioned, Carruthers[20] gives the result,

$$\tau_{\Delta m}^{-1} = \Omega/N \ \sigma\omega^4/4\pi v^2. \tag{63}$$

In Equation 63, $\sigma=\sum_i f_i(1-m_i/\bar{m})^2$, where f_i is the fraction of atoms in the solid having mass m_i. Thus, mass-defect scattering, like point defect strain field scattering, is proportional to the fourth power of frequency, and so cannot limit low temperature heat conduction.

Boundary scattering: For crystals in which the number of imperfections is reasonably small, and at low temperatures such that the phonon mean free path is large, the finite dimensions of the crystal come into play. In this case, phonons are considered to propagate ballistically from one surface element to the next, where they are either specularly reflected, or absorbed and subsequently randomly re-emitted. As a result, the Boltzmann equation as it is written in Equation 21 is inapplicable, since the distribution function N_q must now depend explictly on position.[20]

Berman[42] points out that this situation is analogous to that of Knudsen flow of a gas through a tube. For that example, at ordinary pressures, the rate of gas flow G is proportional to the pressure gradient along the tube according to,

$$G \propto D^4/\eta \; dP/d\ell \;,$$

where, D is the diameter of the cylindrical tube, and η is the viscosity of the gas. For a sufficiently dilute gas under Knudsen flow conditions, one has,

$$G \propto D^3 \; dP/d\ell \;,$$

and the concept of viscosity is lost, since gas atoms collide with one another so infrequently. However, by defining an "effective" viscosity according to,

$$G \propto D^3 \; dP/d\ell \equiv D^4/\eta_{eff} \; dP/d\ell \;,$$

one has the result that $\eta_{eff} \propto D$, no longer independent of extrinsic parameters.

Analogously, for heat flow under boundary scattering conditions, a thermal conductivity is defined from $Q = -\kappa dT/d\ell$, whereas its definition within the context of a distribution function n_q is unclear. Casimir[91] originally calculated the heat flux in the presence of phonon boundary scattering, with the assumption that phonons were completely absorbed at a surface element, and then re-emitted with the Planck distribution function corresponding to the temperature of that surface element. Casimir's results revealed that,

$$\vec{Q} \propto T^3 \, D \, \nabla T \, ,$$

where D is the diameter of a cylindrical solid. Furthermore, from his result, a thermal conductivity could be written in the form,

$$\kappa(T) = 1/3 \, C_v \, v \, D, \tag{64}$$

provided T is sufficiently low that $C_v \propto T^3$, and provided one defines an average phonon velocity v according to,

$$v = \sum_{s=1}^{3} v_s^{-2} / \left(\sum_{s=1}^{3} v_s^{-3} \right) .$$

Here, s denotes the polarization branch.

Equation 64 has been experimentally verified, although it has been shown necessary to account for finite sample length, and for the possibility of specular surface reflections of very long wavelength modes.[92-94] The case of grain boundary scattering is more complicated,[43] since a model is required for the nature of the boundary mismatch. The results are qualitatively the same as Equation 64, where D is a constant dependent upon the size of the grains.

b. Numerical Evaluation

Employing expressions for relaxation rates according to the preceding models, one may compare low temperature experimental data to values obtained from Equation 23. Assuming validity of the Debye approximation at temperatures below about 10 K, one may write Equation 23 in integral form as,

$$\kappa(T) = 1/3\ (1/2\pi^2)(k_B T/\hbar)^3 \sum_s v_s^{-1} \int_0^{\Theta/T} x_s^2\, C_v(x_s)\, \tau(x_s)\, dx_s\ , \qquad (65)$$

where, $C_v(x)$ is the specific heat/mode, given by,

$$C_v(x) = k_B\, x^2/4\sinh^2(x/2)\ ;\quad x = h\omega/k_B T\ .$$

In the above, v_s is the Debye velocity for branch s. For Ar, $\Theta \simeq 85$K, so that $C_v(x)$ is small near the upper limit of the integration in Equation 65, and thus the branch distinction has little effect on the integral. Therefore, Equation 65 can be written,

$$\kappa(T) = 1/3\ C_v\, v^2\, \langle\tau\rangle \qquad (66a)$$

where, the specific heat C_v, is just,

$$C_v = (k_B T/\hbar)^3/8\pi^2 \sum_s v_s^{-3} \int_0^{\Theta/T} \frac{x^4\, dx}{\sinh^2(x/2)}\ . \qquad (66b)$$

The average velocity v is given by,

$$v^2 = \sum_s v_s^{-1} / \sum_s v_s^{-3}\ , \qquad (66c)$$

and the mean relaxation time $\langle\tau\rangle$ is,

$$\langle\tau\rangle = \int_0^{\Theta/T} \frac{\tau(x)\, x^4\, dx}{\sinh^2(x/2)} \Big/ \int_0^{\Theta/T} \frac{x^4\, dx}{\sinh^2(x/2)}\ . \qquad (66d)$$

It is usual practice to write for $\tau(x)$,

$$\tau^{-1}(x) = \sum_i \tau_i^{-1}(x) \ ,$$

where each i denotes a particular type scattering.

By directly summing reciprocal relaxation times, one explicitly neglects any interference between elastic scattering processes, as described in the preceding section. If U-type processes are still important at the temperature of interest, a rate τ_U^{-1} , derived from some model,[69] may be included. A relaxation rate of N-type three-phonon processes was traditionally excluded since N-type collisions conserve both momentum and energy, and so cannot, by themselves, resist energy flow.

Callaway,[63] however, recognized that τ_N should somewhat be included, since if N-processes are still rapid at low temperatures, they can shuffle momentum and energy among the different modes, and thus aid in keeping occupied those states which are scattered strongly by other, resistive, mechanisms (R-type processes). Indirectly, then, N-type collisions could contribute to thermal resistance. Callaway included this effect in a phenomenological manner by expressing $\dot{n}_q$, in the Boltzmann Equation 21, as,

$$\dot{n}_q = -n_q/\tau_R - (N_q^0(\vec{c}) - N_q)/\tau_R \ . \qquad (67)$$

This expression accounts for the fact that N-type processes will relax the distribution N_q back to the drifting phonon distribution, given by,

$$N_q^0(\vec{c}) = (\exp(\hbar(\omega - \vec{c}\cdot\vec{q})/k_B T) - 1)^{-1} \ ,$$

while intrinsic resistive processes described by τ_R relax N_q to the equilibrium distribution N_q^0.

Krumhansl[60] lent credence to Callaway's model by "deriving" a very similar result from a much more fundamental level. His work gives for $\langle\tau\rangle$,

$$\langle\tau\rangle = [\langle\tau_R\rangle s + \langle\tau_R^{-1}\rangle^{-1}]/(1+s), \tag{68a}$$

where,

$$s = \langle\tau_N\rangle/\langle\tau_R\rangle . \tag{68b}$$

The parameter s describes the relative importance of N-type collisions. If N-processes are slow compared to R-processes, then $s >> 1$ and $\langle\tau\rangle \to \langle\tau_R\rangle$. However, for very rapid N-type collisions, $s \to 0$, and $\langle\tau\rangle \to \langle\tau_R^{-1}\rangle^{-1}$. In this latter limit, it is seen that thermal resistivities of the various resistive scattering mechanism are additive, i.e.

$$W \equiv 1/\kappa = \sum_i W_i \quad ; \quad W_i = (1/3\, C_v\, v^2/\langle\tau_i^{-1}\rangle)^{-1}.$$

This situation is the so-called Ziman limit.

c. Results

Using Equations 66, and 68, we fit the experimental low temperature data. This procedure entailed performing numerically the integrals of Equation 66d for a given set of trial relaxation rates at a fixed temperature. The best set of scattering strengths were then found by using a computer search routine[94] such as to best fit the experimental data over a given temperature interval. Since only certain scattering processes are important over certain temperature ranges, it was not necessary to include all scattering mechanisms for each temperature interval of interest. The procedure was as follows:

(i) The average phonon velocity was evaluated once and for all, according to Equation 66c, using the experimental data of Keeler and Batchelder.[95] Likewise,

for the values of the specific heat which go into Equation 66a, we used the experimental data of Finegold and Phillips.[96]

(ii) Employing a phenomenological relaxation rate to depict U-type processes, which was of the form $\tau_U^{-1} = b_U x^2 T^5 e^{-E/T}$,[97] we required that Equation 66a result in a thermal conductivity which best fit our three-phonon theoretical data, previously described, in the temperature interval from 5K to 12 K (this interval encompasses the exponential rise in $\kappa(T)$). To simulate the conditions under which the basic three-phonon calculations were made, the quantity s of Equation 68b was taken to be zero (i.e. very rapid N-processes). This procedure resulted in a value $b_U = 4.836 \times 10^4\ K^{-5}$, and $E = 17.5$ K.

(iii) A functional form for the Normal-process relaxation rate was chosen after the work of Herring[69]: $\tau_N^{-1} = b_N x^2 T^4$. The parameter b_N was then determined by best fitting the experimental data of run #7 for temperatures between 8 K and 15 K, in conjunction with the previous results for b_U and E. These experimental data were chosen for this fit because of the good agreement with the data of some other workers in that temperature interval, even though there were disparities among those same data at lower temperatures. This latter fact indicated

that nearly all of the thermal resistivity in the 8-12 K range was due to three-phonon effects, which should amply be accounted for by only τ_U^{-1} and τ_N^{-1} . The best fit yielded a value for b_N: $b_N = 1.254 \times 10^5\ K^{-4}$.

(IV) The remaining low temperature data (in particular, that of run #10) were then used to ascertain the appropriate scattering strengths of the various scattering rates described in Section a. Expressed in terms of the dimensionless parameter $x=\hbar\omega/k_B T$, these scattering rates have the following functional forms:

Point defects: $\tau_{pt}^{-1} = \alpha\, x^4\, T^4$. In the quantity α is tentatively included the strengths of both mass-defect and point source strain field scattering.

Dislocations: $\tau_d^{-1} = \gamma\, x\, T$.

Boundaries: $\tau_b^{-1} = v/D$. Here, v is the average phonon velocity and D a characteristic length.

Employing only the scattering rate functions listed above, no combination of strengths could be found which adequately reproduced the experimental data of run #10 both on the low T ramp and in the sensitive area of the peak in $\kappa(T)$. However, the inclusion of a rate $\tau_D^{-1} = \delta\, x^2\, T^2$ resulted in the agreement shown in Figure 12. In all cases, the best

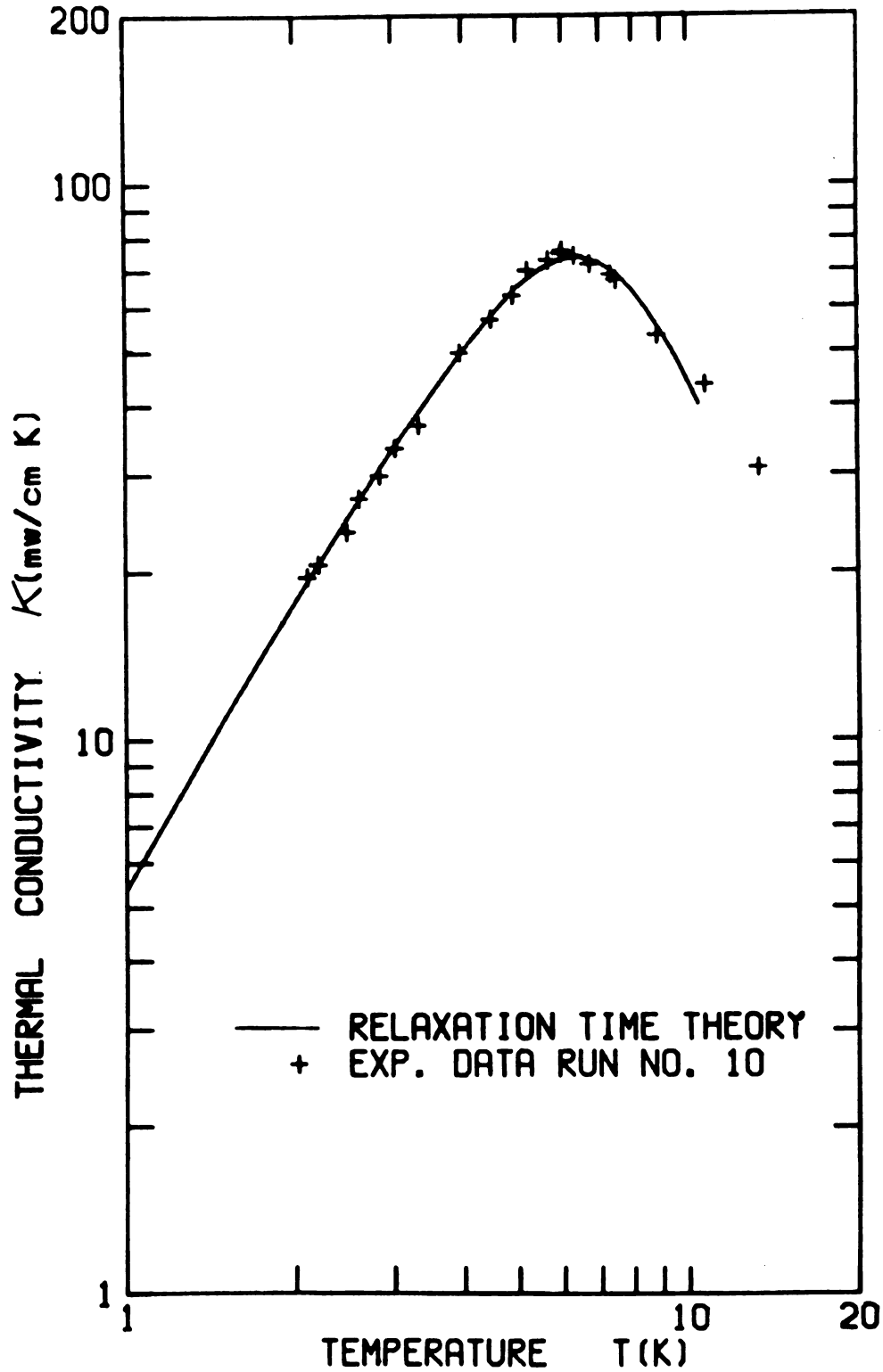

Figure 12: A best fit of the relaxation time model of thermal conductivity to the low temperature data of run #10.

fits were rather insensitive to the (small) values of v/D and α. Therefore, for these parameters we merely inserted D = 1cm, the diameter of the sample, and $\alpha \simeq 33K^{-4}$, which is the value one obtains Equation 63 by considering only mass-defect scattering due to the isotopic impurity Ar^{36}.

The necessity of including the rate τ_D^{-1} is illustrated in Figure 13, which shows the family of curves which results when $\delta = 0$ and γ is varied. Obviously, the exact temperature dependence of the low T ramp is not well produced. Although a member of this family appears to fairly well fit the low T ramp of Clayton and Batchelder's data, it inadequately describes the dependence around the peak. Below about 5 K, the temperature dependence of the curves in Figure 13 is essentially T^2, as expected from the simplified theory of straight line dislocation scattering of phonons. Thus, our experimental data are seen to vary more slowly then T^2, consequently requiring the scattering rate which varies quadratically with frequency in order to provide a component to κ which is linear in T.

Although this temperature dependence is unusual, this trend has been observed previously by Moss[46] in crystals of CaF_2. One set of his data could be fit by considering only τ_D, without need of τ_d while another set could not be well fit with a variety of frequency dependences. Moss attempted to explain this behavior in terms of the formation of dislocation dipoles. In this case, the distant strain field from two close, and oppositely oriented dislocations falls off as r^{-2} rather than r^{-1}. Detailed analysis of this model results in the simple result $\tau_D^{-1} = \tau_d^{-1} \sin^2((\vec{q}/2)\cdot\vec{d})$, where $\vec{d}$ is the vector joining the two

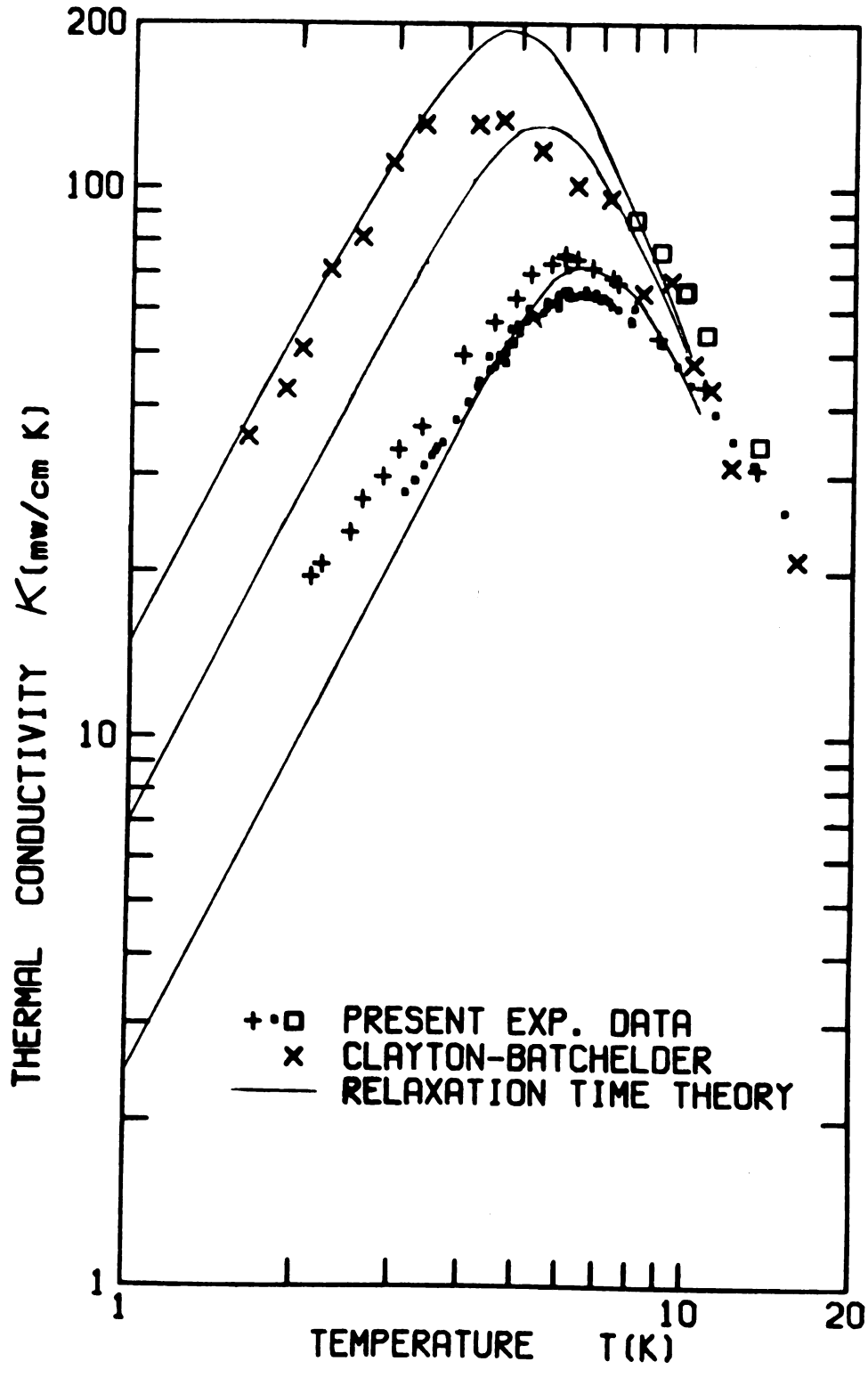

Figure 13: A family of curves for different values of γ, with $\delta=0$. The low T experimental data of runs 7, 8, and #10, and those of Clayton and Batchelder are included for comparison.

dislocation cores. For small separations $\vec{d}$, this rate is then proportional to $\omega\, q^2 d^2 \alpha x^3 T^3 (\frac{d}{v})^2$, which is one order of ω larger than that of the τ_D^{-1} which we found to best fit the data. Besides, the small quantity $(\frac{2\pi}{4}\frac{d}{\lambda})^2$ would greatly decrease the effectiveness of this type of scattering, demanding an unrealistically large density of dislocation dipoles to result in the observed deviation from a T^2 dependence of $\kappa(T)$.

The best fit of Equation 66a to the data of run #10 resulted in the values $\gamma = 1.711\text{X}10^{7}\ \ K^{-1}$ and $\delta = 1.500\text{X}10^{6}\ K^{-2}$. Using Equation 61, one may calculate a dislocation density σ from the quantity γ according to,

$$\sigma = \hbar/k_B\ (\rho/gb\alpha)^2\ (192/v^4)\ \gamma\ , \qquad (69)$$

where the parameters in Equation 69 were defined in Section a, and have the values,

$$v = 1.076\text{x}10^{5}\ \ \text{cm/sec.}$$

$$g = .845\ \phi''' = 5.63\text{X}10^{11}\ \ \text{erg/cm}^3$$

$$\rho = 1.77\ \text{gm/cm}^3$$

$$b = 5\text{X}10^{-8}\ \ \text{cm}$$

$$\alpha = 1.558.$$

Then, $\sigma = 306.8\gamma$, which gives the result, $\sigma = 5.24\text{X}10^{9}\ \ \text{cm}^{-2}$, for the dislocation density.

In view of the need of the additional scattering term and the fact that Peterson et al. were able, by X-ray analysis, to set a lower limit of $\sigma = 10^{6}\text{cm}^{-2}$ for Ar samples prepared and handled in a manner very similar to ours, the value of σ obtained here is suspiciously large. Therefore, it appears the present theory of defect phonon scattering is somewhat lacking, and in need of refinements, especially

in the area of dislocation effects.

Evidently, whatever aspect of the experimental procedure resulted in the rather anomalous temperature dependence, was somewhat reproduced for two of the runs. This can be seen by inspecting Figure 14, which is a plot of a family of curves of various values of γ, but with δ held fixed at the value $1.5X10^{6}$ K^{-2}, which is that obtained from the best fit of the data from run #10. It appears that the data from run #8 (small solid squares) also belong to a member of this family, while it is clear that the data of run #7 (large open squares), and of C-B do not.

Surprisingly, another member of this family of curves also fits very well the low T data of White and Woods. For that curve, however, the distinction between $\delta = 0$, and $\delta = 1.5X10^{6}$ is not so pronounced, due to the relatively large, and thus dominating, value of γ ($\gamma = 8.0X10^{7}$ K^{-1} for that curve).

It is interesting to note the role of N-processes in depicting the thermal conductivity in the relaxation time model. A measure of this is the quantity s of Equation 68b ($s = \langle\tau_N\rangle \langle\tau_R\rangle$). For the fit to the data of run #10, s varies from a value 80 at 1 K, indicating relatively slow N-processes, to a value of about unity in the vicinity of the peak in K(T). Thus, over that entire temperature range, one would obtain erroneous results by attempting to add thermal resistivities for different processes (Ziman limit).

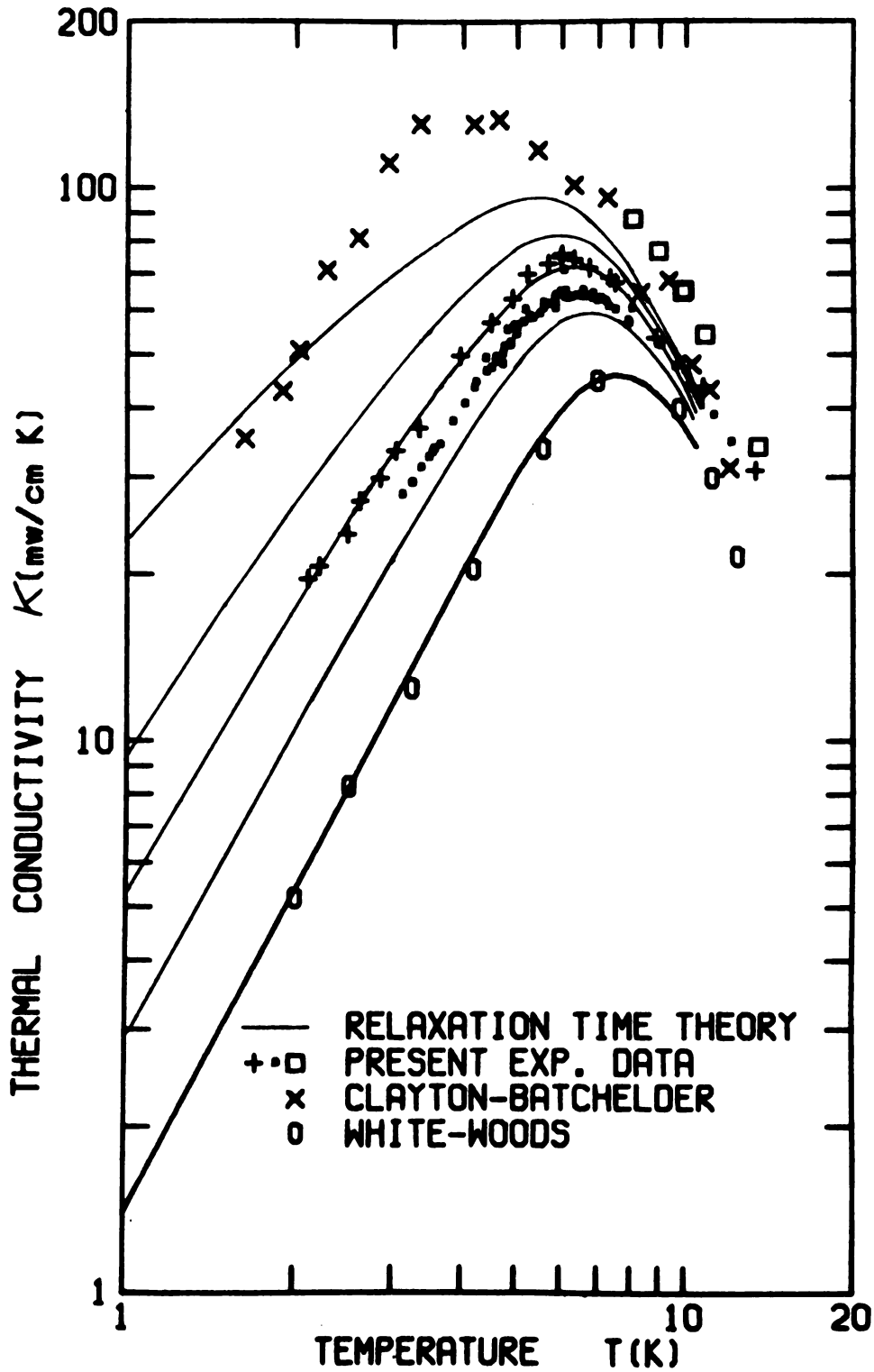

Figure 14: A family of curves for different values of γ, with $\delta = 1.500 \times 10^{6}\ K^{-2}$. Included for comparison are the present experimental data, along with those of Clayton and Batchelder, and of White and Woods.

V. SUMMARY AND CONCLUSIONS

We have measured the thermal conductivity of solid normal Argon over a temperature range from about 2 K to the triple point temperature 83.8 K. Care was taken to make measurements only on large-grained or single crystalline, strain free samples. The data obtained were highly reproducible within a single run, and of sufficient density to make possible quantitative comparison with current theories of heat transport in insulators at low temperatures.

In particular, we computed from first principles the thermal conductivity of an Ar crystal whose lattice wave scattering is entirely of the three-phonon type. The results of these calculations indicate that resistance to heat transport via phonon-phonon interactions is sensitive to the particular form of the potential energy function through which the atoms interact. The heat transport is found to depend sensitively upon even small variations in the magnitude and relative values of the lattice frequencies (due to the exact shape of the interatomic potential). At high temperatures these small variations among potential models are manifested most importantly in the absolute number of phonon-phonon processes observed to occur in the crystal, and less importantly in the values of the scattering matrix elements. At lower temperatures, this distinction is gradually lost.

Within the context of the quasi-harmonic theory of lattice vibrations, the pair potential of Bobetic and Barker, in conjunction with the three-body triple-dipole potential of Axilrod and Teller, is

found to provide reasonable quantitative agreement with the high temperature experimental thermal conductivity data of both constant density, and of free-standing Ar crystals. Thus, the observed T^{-1} temperature dependence of constant volume samples (as expected from the three-phonon collisions of first order perturbation theory), and the observed deviations from this T^{-1} dependence for free-standing samples, appear to be adequately reconciled by the effects of thermal expansion on the normal mode frequencies of the lattice. Therefore, the presence of four-phonon or higher order lattice wave interactions appear to be of minor importance in solid Ar.

For temperatures below 10 K, we fit the experimental data to a relaxation time model of heat transport. This procedure indicated the contribution to the thermal resistance due to grain boundary and impurity scattering to be of negligible magnitude in comparison to that of other mechanisms. Of these other mechanisms, the most predominant is that described by the present theory of phonon scattering by the static strain fields of dislocations. In addition, however, adequate fit to the data necessitated the inclusion of a scattering mechanism which, at present, has little theoretical foundation. This sort of behavior has been observed in $\kappa(T)$ of other insulators, and may be due to some strong coherent phonon scattering by arrays of dislocations, or by dynamic scattering from vibrating dislocation cores.

Unfortunately, at present there exists no complete theory for description of either of these phenomena, although the need for an improved theory of dislocation phonon scattering has been previously recognized. Our data tend to reinforce the apparent inadequacy in the present theory of defect scattering, since the contribution to the

thermal resistivity due to the scattering rate characteristic of dislocation strain fields implies an unrealisticly large dislocation density, especially in view of the care taken in the handling of these samples. It should be noted, however, that there do appear to be certain inherent difficulties in keeping free of defects samples which must undergo thermal cycling.

It would be interesting to relate quantitatively the effects of various manners and rates of cooling to the defect density, which must result from differential thermal contraction. The thermal conductivity, near the region of the peak, provides a sensitive indication of such defect density, and would thus be a valuable tool in investigating the manner in which defects are formed in simple solids.

APPENDICES

1072

APPENDIX A: CRYSTAL NUCLEATION PROBABILITY

By employing the general theory of nucleation, one can obtain at least a qualitative concept of the relatively large nucleation probability of Ar.

The simplest case is that of homogeneous nucleation, i.e. the formation of pure α-phase nuclei in a pure β-phase medium. If it is supposed that thermodynamics can be applied to the α-β system of nuclei in the mother medium, the approach is as follows.

The change in the total free energy of the α-β system when a nucleus of atoms is formed by statistical fluctuations is given by,

$$\Delta G = \Delta G_s + \Delta G_v .$$

The change in the surface free energy, ΔG_s, is proportional to the number of atoms on the surface of the nucleus,

$$\Delta G_s = i^{2/3}\, a ,$$

and, the change in the bulk free energy, ΔG_v, is proportional to the number of atoms in the nucleus,

$$\Delta G_v = i\, b .$$

The net change ΔG is a maximum for $i = i_c = (2a/3b)^3$, in which case,

$$\Delta G = \Delta G_c = 4/27\; a^3/b^2 .$$

This implies that nuclei with $i<i_c$ are unstable and will disperse since ΔG increases with i; but, nuclei with $i>i_c$ will continue to grow since ΔG decreases with i.

The rate of nucleation depends upon the mean time τ needed to form a nucleus of critical size i_c. The energy ΔG_c poses an activation energy barrier for this process, so $\tau \propto \exp(\Delta G_c/k_B T)$. The nucleation rate is also proportional to the number of atoms/unit volume in the α-phase, to the cross-sectional area of the critical sized nuclei, and to the frequency with which atoms move through the boundary between the mother medium and the nucleus. The only situation for which all of these parameters are well known is the formation of spherical liquid droplets in a vapor medium. In this case the rate of nucleation $\dot{N}$ is,[26]

$$\dot{N} = \frac{P}{(2\pi m k_B T)^{1/2}} \; n \; v_\ell / 2 \; (3\gamma/k_B T)^{1/2} \; \exp(-\Delta G_c/k_B T) \; , \qquad \text{(A1)}$$

where,

$$\Delta G_c = 16\pi\gamma^3/3 \; (k_B T/v_\ell \; \ell n(P/P_0))^2 \; . \qquad \text{(A2)}$$

The parameters in Equations A1 and A2 are as follows:

P = Pressure of the vapor,

P_0 = Equilibrium vapor pressure of the bulk liquid,

k_B = Boltzmann constant,

T = Temperature,

m = Atomic mass,

v_ℓ = Volume/atom of liquid,

γ = Surface tension of liquid droplet, and

n = Number of atoms/cm^3 in vapor.

Since all these parameters are known, we may calculate the nucleation rate for Ar and compare it to that of some familiar substance, e.g. H_2O. Since this rate is a sensitive function of the degree of supersaturation P/P_0, we will simply assume this pressure ratio to be the same for both

substances. Furthermore, the nucleation rates will be evaluated at the triple point temperature of each substance to assure analogous conditions.

The results of these straight forward calculations are,

$$\dot{N}_{Ar} = 2.56X10^{28} \exp(-55/(\ell n(P/P_0))^2) \ , \tag{A3}$$

and,

$$\dot{N}_{H_2O} = 2.76X10^{23} \exp(-120/(\ell n(P/P_0))^2). \tag{A4}$$

so,

$$\dot{N}_{Ar}/\dot{N}_{H_2O} = 10^5 \exp(66/(\ell n(P/P_0))^2). \tag{A5}$$

For reasonable values of supersaturation the absolute rates given by Equation A3 and A4 are unrealistically small. This does not necessarily imply they are in error, however, since in normal practice observed nucleation occurs heterogeneously (foreign particles, ions, or surfaces catalyze the nucleation event). For example, it has been experimentally verified for water that homogeneous droplet formation will never be observed unless supersaturation is imposed very rapidly and is of magnitude $P/P_0 \simeq 7$.[27]

While Equation A5 does not depict real experimental conditions, the huge disparity it displays between the rates for Ar and H_2O gives a qualitative indication of the rapidity with which Ar will nucleate. This is fundamentally the result of the short-ranged and weak interatomic forces of Ar, as manifested in the relatively small surface tension which enters into Equation A2 as the third power.

APPENDIX B: THE PROBLEM OF PLASTIC DEFORMATION

Under ideal conditions, one can easily derive the net stress on the upper surface of the solid Ar sample due to the bellows spring force. As the temperature is lowered from the triple point (where there is no net stress) this quantity will rapidly rise and then gradually fall off to some constant value at 0 K, that constant value being given by the bellows' spring pressure evaluated at a displacement equal to that of the overall length contraction of the sample. In practice, the important question arises: Is there, at any time during the course of the cool-down, a compressional stress sufficiently large to induce plastic deformation of the sample? In an attempt to answer this question, we evaluate the net stress at the temperature for which it is a maximum.

The zero initial displacement condition occurs at T=83.8 K and P=516.8 Torr (i.e. at the triple point immediately after the solid has frozen). A change in relative vertical position of the sample and upper block due to bellows motion alone is given by (see Figure B1),

$$\Delta\ell = \alpha(516.8 \text{ Torr} - P) \ , \tag{B1}$$

where, P is the ambient pressure within the tube (Ar sublimation pressure), and α is the bellows compliance rate which we measured to be about 1 mm/200 Torr. Likewise, a displacement $\Delta\ell_{bulk}$ due to thermal contraction of the solid is,

$$\Delta\ell_{bulk} = -\ell_0/3 \int_{83.8K}^{T} \beta(T')\, dT' \ . \tag{B2}$$

Here, ℓ_0 is the initial sample length $\simeq$ 30mm, and $\beta(t)$ is the volume thermal expansivity at temperature T.

At some temperature T, the net stress σ is given by,

$$\sigma = 516.8 \text{ Torr} - \Delta\ell_{bulk}/\alpha - P \ , \qquad \text{(B3)}$$

and the condition for which σ is a maximum is,

$$\frac{d\sigma}{dT} = 0 = -\ 1/\alpha \ \frac{d\ell_{bulk}}{dT} - \frac{dP}{dT} \ ; \quad \text{or} \ \frac{d\ell_{bulk}}{dT} = \frac{d\ell}{dT} \ .$$

So,

$$\ell_0/3 \ \beta(T) = \alpha \ dP/dT \ ,$$

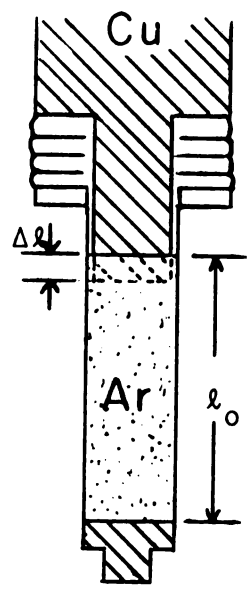

Figure B1: An illustration of the parameters $\Delta\ell$ and ℓ_0.

and, dP/dT can be expressed as,[30]

$$dP/dT = P/T\ (10^3/T - 0.5)\ .$$

This yields the relation,

$$T = 0.5\ P/\beta(T)\ (T^{-1} - 5X10^{-4}). \qquad \text{(B4)}$$

One obtains from Equation B4 the solution,

$$T \simeq 62.8\ K\ ,\ \text{and}\ P = 12\ \text{Torr}\ .$$

Thus,

$$\sigma \simeq 507\ \text{Torr} - \Delta\ell_{bulk}/\alpha \simeq 6.8\ gm/mm^2\ .$$

Unfortunately, whether or not this stress exceeds the yield strength of solid Ar a 63 K is not evident, since this quantity, as far as we know, has not been measured on single or large-grained solids. A lower limit on the yield stress may be obtained from the work of Stroilov et al.,[31] who measured the yield stress of polycrystalline samples. These workers recorded a value of about 43 $\frac{gm}{mm2}$ at 63 K. Also Stansfield measured the ultimate tensile strength of solid Ar at 75 K, and obtained a value of about 50 gm/mm^2.[32] On the other hand, the theoretical yield strength at 0 K is greater than 1000 gm/mm^2.[33] Thus, these values are strongly indicative that plastic deformation is unlikely.

APPENDIX C: ON THE VALIDITY OF EQUATION 3

For a sample of constant cross-sectional area A and length L, and whose ends are at temperatures T and $T + \Delta T$, one obtains from Equation 3 and Equation 1, respectively,

$$\dot{Q}/A = \kappa_{eff}(\bar{T})\ \Delta T/L \ ; \quad \dot{Q}/A = \kappa(T)\ dT/dx. \tag{C1}$$

So,

$$\kappa_{eff}(\bar{T}) = L/\Delta T \int \kappa(T)\ dT/dx \ . \tag{C2}$$

The quantity $\kappa_{eff}(\bar{T})$ is an effective thermal conductivity defined by Equation 3, and $\bar{T} = T + \Delta T/2$ is the effective temperature of the sample. The right hand side of Equation C2 is true at any point in the solid. Integrating over the length of the sample,

$$\kappa_{eff}(\bar{T}) = 1/\Delta T \int_{T-\frac{\Delta T}{2}}^{\bar{T}+\Delta T/2} \kappa(T)\ dT = \int_{-\frac{\Delta T}{2}}^{\Delta T/2} \kappa(\tau+\bar{T})\ d\tau \ , \tag{C3}$$

where, $\tau = T - \bar{T}$.

To see how $\kappa_{eff}(\bar{T})$ differs from $\kappa(T)$ evaluated at $\bar{T}$, we expand $\kappa(T)$ in a Taylor series about $\bar{T}$.

$$\kappa(T) = \kappa(\bar{T}) + \partial\kappa(\bar{T})/\partial\bar{T}\ \tau + 1/2\ \partial^2\kappa(\bar{T})/\partial\bar{T}^2\ \tau^2 + \ldots$$

Of the terms retained, only the zeroth and second order terms contribute to the integral, and one obtains,

$$\frac{\kappa_{eff}(\bar{T}) - \kappa(\bar{T})}{\kappa(\bar{T})} \simeq 1/24\ \kappa''(\bar{T})/\kappa(\bar{T})\ \Delta T^2 \tag{C4}$$

Equation C4 gives the fractional difference between $\kappa_{eff}(T)$ and $\kappa(T)$ in terms of the temperature differential ΔT.

By knowing the approximate temperature dependence of $\kappa(T)$, one can set a safe upper limit on ΔT such that the effect of this type of error is negligible. We give here some quantitative examples:

In the high temperature range, assume $\kappa(T) = \frac{A}{T}$; then, $\kappa'' = 2A/T^2$. Demanding no greater than a 1% error, one has the condition,

$$\Delta T \lesssim \sqrt{0.12}\, T. \qquad \text{(C5)}$$

Thus, at 80 K, for example, the allowed ΔT is $\Delta T \lesssim 28$ K.

Likewise, in the low temperature region, if $\kappa(T) = BT^2$, then Equation C5 is again the correct expression. At 2 K, $\Delta T \lesssim 0.7$ K.

APPENDIX D: THERMAL RELAXATION TIMES

The model for the transient heat flow problem of interest is depicted in the Figure D1. This setup consists of a highly thermally conducting block at temperature T. The block is of mass M_{bl} and specific heat C_{bl}. It is connected to a thermal reservoir at a fixed temperature $T_0<T$ by a thermal conductor with constant cross-sectional area A_{cond} and total length L_{cond}. This conductor possesses a total heat conductance given by $K_{cond} = (\kappa A/L)_{cond}$, which is assumed to be much less than that of the block, and it has a density ρ_{cond} and a specific heat C_{cond}.

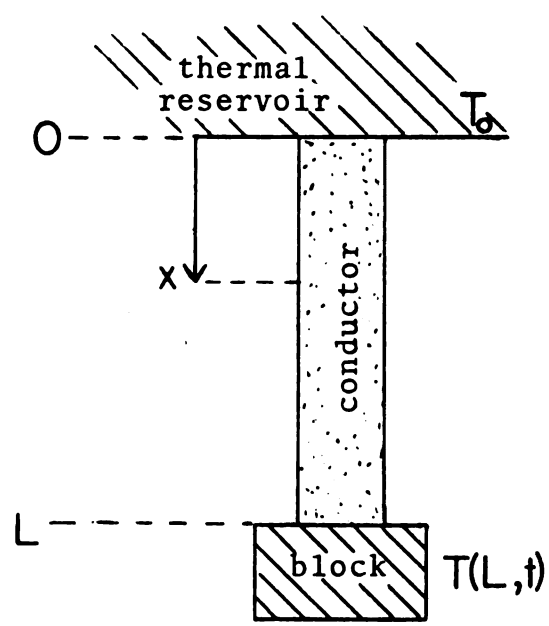

Figure D1: A physical model for the transient heat flow problem.

The temperature at position x in the conductor at some time t is given by the solution of the Fourier heat conduction equation.

$$\partial^2 T(x,t)/\partial x^2 = C_{cond}\ \rho_{cond}/\kappa_{cond}\ \partial T(x,t)/\partial t\ . \qquad (D1)$$

By separation of variables, it is a simple matter to find a general solution to Equation D1 of the form,

$$T(x,t) = [B\ \sin\beta x + C\ \cos\beta x]e^{-t/\tau} + Dx + E, \qquad (D2)$$

where,

$$\tau = C_{cond}\ \rho_{cond}\ \kappa_{cond}^{-1}\ \beta^{-2}\ . \qquad (D3)$$

This solution is subject to the following boundary condition:

(i) $T(0,t) = T_0$

(ii) $T(x,\infty) = T_0$

(iii) $\partial T(L,t)/\partial x = -M_{bl}\ C_{bl}\ \dot{T}(L,t)/\kappa_{cond}\ A_{cond}$

Condition (iii) is just Equation 1 of the text, with $\vec{Q}$ given by the heat loss rate of the block. $M_{bl}\ C_{bl}\ \dot{T}(L,t)/A_{cond}$. Condition (i) implies C=0. and $E=T_o$. while condition (ii) yields D=C. Condition (iii) determines β according to,

$$(\beta L)_{cond}\ (MC)_{cond}/(MC)_{cond} = \cot(\beta L_{cond}), \qquad (D4)$$

where, $M_{cond} = (\rho AL)_{cond}$.

This transcendental relation has an infinite number of solutions β_n, so the temperature at the block at any time t is,

$$T = T(L,t) = \sum_{n=1}^{\infty} B_n\ \sin(\beta_n L)\ e^{-t/\tau_n} + T_0\ ;\ \tau_n = (C\rho/\kappa)_{cond}\ 1/\beta_n \qquad (D5)$$

Although the B_n can be determined,[34] they are not needed explicitly for our application.

For the case where the heat conductor consists of only the electrical leads which run from the thermometer and heater on the block to the thermal reservoir (upper block), the ratio of the total heat capacities $(MC)_{bl}/(MC)_{cond}$ in Equation D4 is large (about 390). Thus, $\beta_1 L_{cond}$ is small and approximately equal to $\sqrt{(MC)_{cond}/(MC)_{bl}}$. Since the higher order solutions are given by $\beta_n L_{cond} \simeq n\pi$, terms in Equation D5 for $n > 1$ damp out quickly compared to the n=1 term.

Our procedure was to employ Equation D5 in the form,

$$\ell n(T-T_0) = \ell n[B_1 \sin(\beta_1 L_{cond})] - t/\tau_1 \; ; \quad t > \tau_2. \tag{D6}$$

This was done by initially heating the lower block to some temperature $T>T_0$ in the absence of an Ar sample, and then allowing the block to thermally relax toward the temperature T_0, while monitoring the time dependence of T. From a least squares fit of Equation D6 to the recorded data, we could ascertain the value of τ. From Equation D3 and the expression for $\beta_1 L_{cond}$ we find that,

$$\tau_1 = (MC)_{bl}/K_{cond}. \tag{D7}$$

It should be pointed out, incidentally, that this form for τ_1 is identical with that obtained for heat loss by radiation, which is described by a relation of the same form as Equation D6. Thus, the K_{cond} derived from the measured τ_1, can be regarded as a total conductance representative of <u>all</u> mechanisms of heat loss from the lower block. Once K_{cond} is evaluated from Equation D7, the following corrected form of Equation 3 yields the Ar thermal conductivity,

$$\kappa = L/A \; (\dot{Q}/\Delta T - K_{cond}). \tag{D8}$$

It should be noted that, although the geometrical factos A_{cond} and L_{cond} were used in the development of Equation D6, their values are not needed, since they are contained in K_{cond}. One must know, however, the mass M_{bl} and specific heat C_{bl} of the block in order to evaluate K_{cond} from Equation D7.

For example, at 80 K we obtained from the least squares fit of Equation D6, $\tau_1 = 2.8 \times 10^4$ sec = 7.7 hr. This quantity, along with the known mass M_{bl} and the specific heat C_{bl},[35] yields the value, $K_{cond} = 0.18$ mwatt/K. A typical value of the measured uncorrected conductance, $K = \dot{Q}/\Delta T$, at this temperature is about 1 mwatt/K, so that K_{cond} represents a correction of about 18%.

It is interesting to notice that if the Ar sample itself is considered to be the conductor, then the ratio of total heat capacities in Equation D4 is small at high temperatures. In the limit of a massless block, $\beta_1 L = \pi/2$, and $\tau_1 = C\rho L^2/\kappa(\pi/2)^2$. At temperatures near the triple point the quantity $C\rho/\kappa$ is very large for Ar (e.g. at 80 K, $(C\rho/\kappa)_{Ar} \simeq 7000\ (C\rho/\kappa)_{Cu}$. In this limit of a massless block, one calculates from Equation D3 that $\tau_1 \simeq 45$ min. Since a time interval equal to several τ is needed for the establishment of thermal equilibrium, this characteristic is a significant handicap in making high temperature thermal conductivity measurements.

APPENDIX E: THREE-PHONON COLLISION OPERATOR

We present here a derivation of the three-phonon collision operator. Although these expressions are given elsewhere,[19,52,53,75] their interpretation is often obscured by notation, and in some cases are inconsistent or erroneous (e.g. Julian[52] notes the results of Leibfried[75] are in error by a factor of two).

When the third order anharmonic potential $\Phi^{(3)}$, given by Equation 27 of the text, is written in terms of only the energy conserving products of annihilation and creation operators, (i.e. products of the form $a^\dagger_q a^\dagger_{q'} a^\dagger_{q''}$ or $a_q a_{q'} a_{q''}$ do not contribute), one has,

$$\Phi^{(3)} = N/6\ (\hbar/2N)^{3/2} \sum_{qq'q''} \frac{\Phi(qq'q'')}{\omega_q \omega_{q'} \omega_{q''}} \left[-a_q a_{q'} a^\dagger_{-q''} + a_q a^\dagger_{-q'} a^\dagger_{-q''}\right.$$

$$\left. - a_q a^\dagger_{-q'} a_{q''} - a^\dagger_{-q} a_{q'} a_{q''} + a^\dagger_{-q} a_{q'} a^\dagger_{-q''} + a^\dagger_{-q} a^\dagger_{-q'} a_{q''}\right] . \qquad \text{(E1)}$$

Using the properties of $\Phi(qq'q')$: $\Phi(qq'q') = \Phi(q'qq')$, etc. $= -\Phi(-q-q'-q')$, Equation E1 can be written in more condensed form,

$$\Phi^3 = N/2\ (\hbar/2N)^{3/2} \sum_{qq'q''} \left[\Phi(qq'-q'')\, a^\dagger_q a^\dagger_{q'} a_{q''}\right.$$

$$\left. - \Phi(q-q'-q'')\, a^\dagger_q a_{q'} a_{q''}\right] / (\omega_q \omega_{q'} \omega_{q''})^{1/2} . \qquad \text{(E2)}$$

For the phonon state $q=\vec{q},s$, terms of the form $a_q^\dagger a_{q'}^\dagger a_{q''}$, for example, represent transitions for which state q is increased by one phonon, while terms of the form $a_q a_{q'}^\dagger a_{q''}^\dagger$ deplete the state q by one phonon, and thus will contribute negatively to the rate of change of the distribution n_q. Using the Master equation $\dot{n}_q = \sum_{q'} [P_{q'\to q} - P_{q\to q'}]$ and the transition rates given by Equation 29 of the text, we get Equation 32, reproduced here,

$$\dot{n}_q = 2\pi/\hbar^2\ \hbar^3/32N \sum_{q's''} \{2|\Phi(qq'-q'')|^2 (N_q+1)(N_{q'}+1)N_{q''}$$
$$- |\Phi(-qq'q')|^2 N_q (N_{q'}+1)(N_{q''}+1) + |\Phi(q-q'-q'')|^2 (N_q+1) N_{q'} N_{q''}$$
$$-2|\Phi(qq'-q'')|^2 N_q N_{q'} (N_{q''}+1)\}/\omega_q \omega_{q'} \omega_{q''} . \qquad \text{(E3)}$$

These terms arise from selecting out of Equation E2 the final or initial states q, assigning the sign of the term in accordance with its contribution to or depletion from the state q, and then summing over all other states q',q'' (the $\vec{q}''$ sum is implied due to the momentum conservation condition $\Delta(\vec{q}\pm\vec{q}'\pm\vec{q}'')$. The phonon occupation products of the form $(N_q+1)N_{q'}N_{q''}$ are matrix elements of the products of three operators $a_q^\dagger a_{q'} a_{q''}$ taken between initial and final phonon occupation number states according to Equation 17 of the text. The N_q are assumed thermally averaged such that they represent the true local phonon distributions of the crystal.

Employing the Peierls linearization scheme described in the text, one obtains,

$$\dot{n}_q = \pi/16\ \hbar/N \sum_{q's''} \{2|\Phi(qq'-q'')|^2 [n_q((N^{0'}+1)N^{0''} - N^{0'}(N^{0''}+1))$$

$$+ n_{q'}((N^0+1)N^{0''}-N^0(N^{0''}+1)) + n_{q''}((N^0+1))N^{0'}+1) - N^0N^{0'})]$$

$$+ |\Phi(q-q'-q'')|^2[n_q(N^{0'}N^{0''} - (N^{0'}+1)(N^{0''}+1)) + n_{q'}((N^0+1)N^{0''}$$

$$- N^0(N^{0''}+1)) + n_{q''}((N^0+1)N^{0'}-N^0(N^{0'}+1))]/\omega x\omega'\omega'' .$$

By writing $N^0 = e^{-x/2}/2\sinh(x/2)$ and $N^0+1 = e^{x/2}/2\sinh(x/2)$, and utilizing the energy conservation conditions $x\pm x'\pm x'' = 0$, we see that the term $[(N^{0'}+1)N^{0''}-N^{0'}(N^{0''}+1)]$, for example, becomes,

$$\frac{e^{x'/2}\ e^{-x''/2} - e^{-x'/2}\ e^{x''/2}}{4\sinh(x'/2)\ \sinh(x''/2)} = \frac{e^{-x/2}(e^{\frac{x+x'-x''}{2}} - e^{x/2}(e^{\frac{-x-x'+x''}{2}})}{4\sinh(x'/2)\ \sinh(x''/2)} .$$

Energy conservation requires $x+x'-x''= 0$, so

$$[(N^{0'}+1)N^{0''} - N^{0'}(N^{0''}+1)] = -\sinh(x/2)/2\sinh(x'/2)\sinh(x''/2).$$

With this, and similar results, one obtains,

$$\dot{n}_q = \pi\hbar/16N \sum_{q's''} \{\frac{-\sinh(x/2)}{\sinh(x'/2)\sinh(x''/2)}[|\Phi(qq'-q'')|^2$$

$$+ 1/2|\Phi(q-q'-q'')|^2]n_q + \frac{\sinh(x'/2)}{\sinh(x/2)\sinh(x''/2)}[|\Phi(q-q'-q'')|^2$$

$$+ |\Phi(qq''-q')|^2 - |\Phi(qq'-q'')|^2]n_{q'}\}/\omega x\omega'\omega'' \qquad \text{(E4)}$$

Thus, Equation E4 may be formally written, $\dot{n}_q = \sum_{q'} G_{qq'} n_{q'}$, where the diagonal and non-diagonal components of the collision operator G are apparent. Due to similarities in notation, Equation E4 can most readily be compared with the expressions given by Bennett,[53] and we find some disagreement in the value of the multiplying constants. These

disparities are apparently due to typographical errors in Bennett's paper.

APPENDIX F: EXPRESSION FOR THE THREE-PHONON THERMAL CONDUCTIVITY

To obtain an expression for the three-phonon thermal conductivity, we begin by substituting the distribution $n_q^* = \sum_\alpha A_\alpha \eta_{1\alpha}(q)$ into the Peierls-Boltzmann Equation 35 of the text.

$$|\theta^*\rangle = \sum_\alpha G^* |\eta_{1\alpha}\rangle A_\alpha = \sum_\alpha A_\alpha R^* |\eta_{1\alpha}\rangle ,$$

where we have used the Dirac vector notation (e.g. $\theta_q^* = \langle q|\theta^*\rangle$). Then, operating from the left with $\langle\eta_{1\beta}|$, one obtains,

$$\langle\eta_{1\beta}|\theta^*\rangle = \sum_\alpha \langle\eta_{1\beta}|R^*|\eta_{1\alpha}\rangle A_\alpha ,$$

which is a matrix equation for the coefficients A_α. Now, the quantity,

$$\langle\eta_{1\beta}|R^*|\eta_{1\alpha}\rangle \propto \sum_{qq'} q_\alpha q'_\beta R^*_{qq'} ,$$

vanishes unless $\alpha=\beta$, as a result of cubic symmetry. Furthermore, all $\langle\eta_{1\beta}|R^*|\eta_{1\alpha}\rangle$ are equal for the same reason. Thus, the coefficients A_α are given by,

$$A_\alpha = A = \langle\eta_{1\alpha}|\theta^*\rangle / \langle\eta_{1\alpha}|R^*|\eta_{1\alpha}\rangle ,$$

so that

$$n_q^* = \sum_\alpha \langle\eta_{1\alpha}|\theta^*\rangle / \langle\eta_{1\alpha}|R^*|\eta_{1\alpha}\rangle \eta_{1\alpha}(q)$$

Then the heat flux $\vec{Q} = \sum_q \hbar\omega_q \vec{v}_q n^*_q / 2\sinh(x_q/2)$ becomes,

$$\vec{Q} = 1/\Omega \sum_\alpha \sum_q \frac{\hbar\omega_q \vec{v}_q \eta_{1\alpha}(q)}{2\sinh(x_q/2)} \sum_{q'} \eta_{1\alpha}(q') \sinh(x'/2) \partial N^0_{q'}/\partial T \; \vec{v}_{q'} \cdot \nabla T / \langle \eta_{1\alpha} | R^* | \eta_{1\alpha} \rangle . \quad (F1)$$

From Equation F1, one may define the thermal conductivity tensor $\overleftrightarrow{\kappa}(T)$ according to $\vec{Q} = -\overleftrightarrow{\kappa} \cdot \nabla T$.

Since $\eta_{1\alpha}$ is odd in $\vec{q}$, then the sum over $\vec{q}$ in Equation F1 is non-zero only for the α-components of $\vec{v}_q$. Likewise, the sum over $\vec{q}'$ vanishes unless ∇T has an α-component, all a consequence of cubic symmetry. Thus it is seen that $\kappa(T)$ is a scalar quantity given by,

$$\kappa(T) = -k_B/\Omega \left[\sum_q \frac{x_q v_q \eta_{1\alpha}(q)}{4\sinh^2(x_q/2)} \right]^2 / \sum_{qq'} \eta_{1\alpha}(q) \eta_{1\alpha}(q') R^*_{qq'} ,$$

or,

$$\kappa(T) = -k_B/3\Omega \left[\sum_q \frac{x_q (\vec{v}_q \cdot \vec{q})}{4\sinh^2(x_q/2)} \right]^2 / \sum_{qq'} \frac{(\vec{q} \cdot \vec{q}') \; R^*_{qq'}}{4\sinh(x_q/2)\sinh(x_{q'}/2)} .$$

APPENDIX G: NUMERICAL TREATMENT OF EQUATION 47

The expression for the three-phonon thermal conductivity denominator, Equation 47, involves double wavevector space sums of the form,

$$\sum_{\underset{\sim}{q}s} \sum_{\underset{\sim}{q}'s'} f(\vec{q}s\vec{q}'s') \; \Delta(\vec{q}\pm\vec{q}'\pm\vec{q}'') \; \delta(\omega_q \pm \omega_{q'} \pm \omega_{q''}) \; ,$$

which, for a fine enough wavevector grid, can be represented for computational purposes, as

$$(N/4n_m^3)^2 \sum_{\underset{\sim}{q}s}^{IBZ} W(\vec{q}) \sum_{\underset{\sim}{q}'s'} f(qq') \; \Delta(\vec{q}\pm\vec{q}'\pm\vec{q}'') \cdot \iint_{\substack{\text{grid} \\ \text{cell}}} d^3q_1 \; d^3q_2 \; \delta((\omega_q+\omega_1) \pm (\omega_{q'}+\omega_2) \pm \omega_{q''}) / \iint d^3q_1 d^3q_2 \qquad \text{(G1)}$$

Here, again, $W(\vec{q})$ weights the wavevectors $\vec{q}$ according to their cubic symmetry type vectors, and the function $f(qq')$ has been pulled outside the grid cell integrals since it does not vary much over the volume of the grid cells. The resulting double integral averages the singular energy delta function over the full grid cells at $\vec{q}$ and $\vec{q}'$. In Equation G1, ω_1 and ω_2 represent the small variations in the frequencies ω_q and $\omega_{q'}$ respectively, as the wavevectors $\vec{q}_1$ and $\vec{q}_2$ vary over the volume of the grid cells at $\vec{q}$ and $\vec{q}'$.

Due to the finite size of the grid cells, this integration results in a broadened weight function $S(z)$ which has a maximum value when $z = |\omega_q \pm \omega_{q'} \pm \omega_{q''}| = 0$, but which is non-zero for values of z within the extent of frequency variations within the grid cells at $\vec{q}$ and $\vec{q}'$.

That this is so can be seen by execution of the integral for a specific delta function representation. We present here an example

for the case where,

$$\delta(x) = \lim \varepsilon \to 0 \frac{1}{\pi} \frac{\varepsilon}{x^2 + \varepsilon^2} .$$

Thus, one has for $S(z)$, where $z = (\omega_q - \omega_{q'} - \omega_{q''})$,

$$S(z) = \lim_{\varepsilon \to 0} \frac{\varepsilon}{\pi} \iint_{\substack{\text{grid} \\ \text{cells}}} \frac{d^3q_1 d^3q_2}{(z+\omega_1-\omega_2)^2 + \varepsilon^2} \Big/ \iint d^3q_1 d^3q_2 \qquad \text{(G2)}$$

To a good approximation, the variation of frequency within a grid cell is just the scalar product of the wavevector deviation and the phonon group velocity at the grid point, i.e.

$$\omega_1 = \omega_{q+q_1} - \omega_q \simeq \frac{\partial \omega_q}{\partial \underset{\sim}{q}} \cdot \vec{q}_1 = \vec{v}_q \cdot \vec{q}_1$$

Also, to simplify the integration, we approximate the cubic grid cell by a spherical one of the same volume. Then, one has that,

$$S(z) \propto \varepsilon \iint_{-R}^{+R} \frac{A_1 dq_1 A_2 dq_2}{(z+\omega_1-\omega_2)^2+\varepsilon^2} , \qquad \text{(G3)}$$

where, A_1 and A_2 are surfaces of constant frequency within the spherical grid cell (e.g. see Figure G1).

In Figure G1, R is the radius of the spherical grid cell, given by

$$R = (3/4\pi)^{1/3} \, 2\pi/a_o n_m .$$

Defining the quantities, $\omega_1^0 = v_q R$ and $\omega_2^0 = v_{q'} R$, which represent the maximum variation of frequency within the grid cells, Equation G3 can be written,

$$S(z) \propto \frac{\varepsilon \pi^2}{v_q^3 v_{q'}^3} \int_{-\omega_1^0-\omega_2^0}^{\omega_1^0 \, \omega_2^0} \frac{(\omega_1^{0\,2}-\omega_1^2)(\omega_2^{0\,2}-\omega_2^2)}{(z+\omega_1-\omega_2)^2+\varepsilon^2} \, d\omega_1 d\omega_2 \qquad \text{(G4)}$$

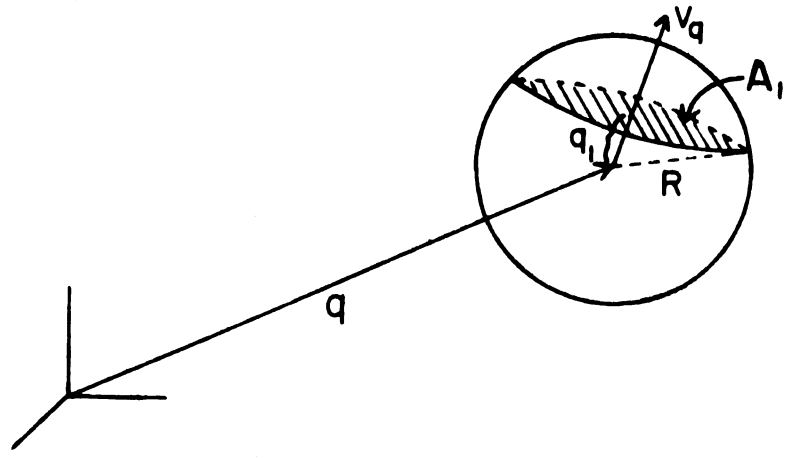

Figure G1: A spherical grid cell at grid point $\vec{q}$, illustrating the phonon group velocity $\vec{v}_q$, and a constant frequency surface A.

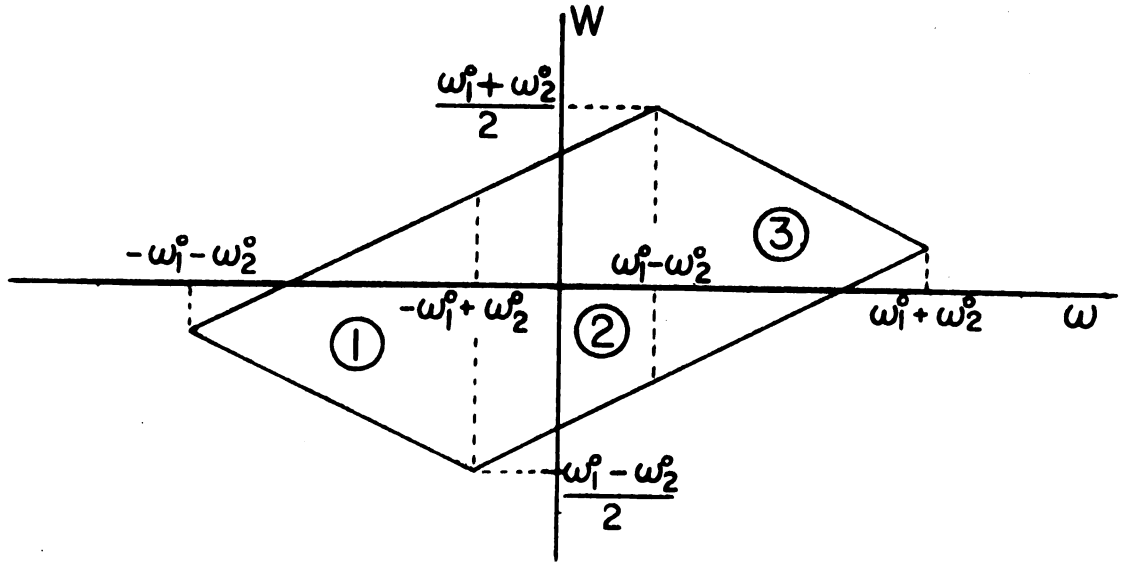

Figure G2: The region of integration for the variables ω and W, expressed in terms of ω_1^0 and ω_2^0.

By transformation to "center of mass" and "relative" coordinates,

$$\omega = \omega_1 - \omega_2 \text{ and } W = (\omega_1 + \omega_2)/2 \ .$$

Equation G4 becomes,

$$S(z) \propto \frac{\varepsilon\pi^2}{v_q v_{q'}} \iint \frac{[\omega_1^{0\,2} - (W+\omega/2)^2]\,[\omega_2^{0\,2} - (W-\omega/2)^2]}{(z+\omega)^2 + \varepsilon^2}\, d\omega\, dW \ . \tag{G5}$$

The region of integration for these variables is shown in Figure G2. In Figure G2, we have shown the case where $\omega_1^0 > \omega_2^0$.

If we further define the variable $\zeta = z + \omega$, we need not retain terms in the numerator of Equation G5 which are non-zero order in ζ, since integrals of the form,

$$\lim_{\varepsilon \to 0} \ \varepsilon \int \frac{\zeta^n\, d\zeta}{\zeta^2 + \varepsilon^2}$$

vanish unless n=0. Thus, Equation G5 becomes,

$$S(z) \propto \frac{\pi^2}{v_q^3 v_q^3} \int [\omega_1^{0\,2} - (W - z/2)^2]\,[\omega_2^{0\,2} - (W+z/2)^2]\ dW\ \varepsilon \int \frac{d\zeta}{\zeta^2 + \varepsilon^2} \tag{G6}$$

As can be seen from Figure G2, the integrations are carried out over three separate regions. For example, the ζ-integral for region (1) is,

$$\lim_{\varepsilon \to 0} \varepsilon \int \frac{d\zeta}{\zeta^2 + \varepsilon^2} = \lim_{\varepsilon \to 0} \tan^{-1}(\zeta/\varepsilon) \Big|_{z-\omega_1^0-\omega_2^0}^{z-\omega_1^0+\omega_2^0} \tag{G7}$$

Equation G7 indicates that unless $\omega_1^0 - \omega_2^0 < |z| < \omega_1^0 + \omega_2^0$, there is no contribution to $S(z)$ from integrals over region (1). The interval (3) ζ-integral gives the same information, while for interval (2), the condition is $0 \le |z| \le \omega_1^0 - \omega_2^0$. Thus, the range of values of z for which $S(z)$ is non-zero are,

$$-\omega_1^0 - \omega_2^0 \le z \le \omega_1^0 + \omega_2^0 \tag{G8}$$

The condition G8 reveals the intuitive percept that, in compensation for the finite grid size, the energy conservation condition is allowed a maximum deviance from z=0, which is characterized by the true wavevectors $\vec{q}$ and $\vec{q}$ not being situated at the center of the grid cells, but rather at points on the surfaces defined by the direction of maximum frequency change.

In general, one obtains the result,

$$S(z) = \frac{9/16}{\omega_1^{03}\omega_2^{03}} \int_a^b [\omega^{>2} - (W-|z|/2)^2][\omega^{<2} - (W+|z|/2)^2]\, dW$$

where,

$$\text{(i)} \quad a = |z|/2 - \omega^{>},\ b = -|z|/2 + \omega^{<}$$
$$\text{if } |\omega_1^0 - \omega_2^0| \leq |z| \leq \omega_1^0 + \omega_2^0 .$$
$$\text{(ii)} \quad a = -|z|/2 - \omega^{<},\ b = -|z|/2 + \omega^{<}$$
$$\text{if } 0 \leq |z| \leq |\omega_1^0 - \omega_2^0| .$$

and, $\omega^{<}$ ($\omega^{>}$) is the smaller (larger) of ω_1^0 and ω_2^0.

The above result is similar to one obtained by Goldman et al.,[78] which is based upon a general method by Gilat and Kam,[79] but differs in that Goldman et al. performed only a single grid cell integration, requiring that deviations of the other cell's wavevector be correlated in a certain way to those of the first.

Figure G3 displays the general features of S(z), for various (arbitrary) values of ω_1^0 and ω_2^0.

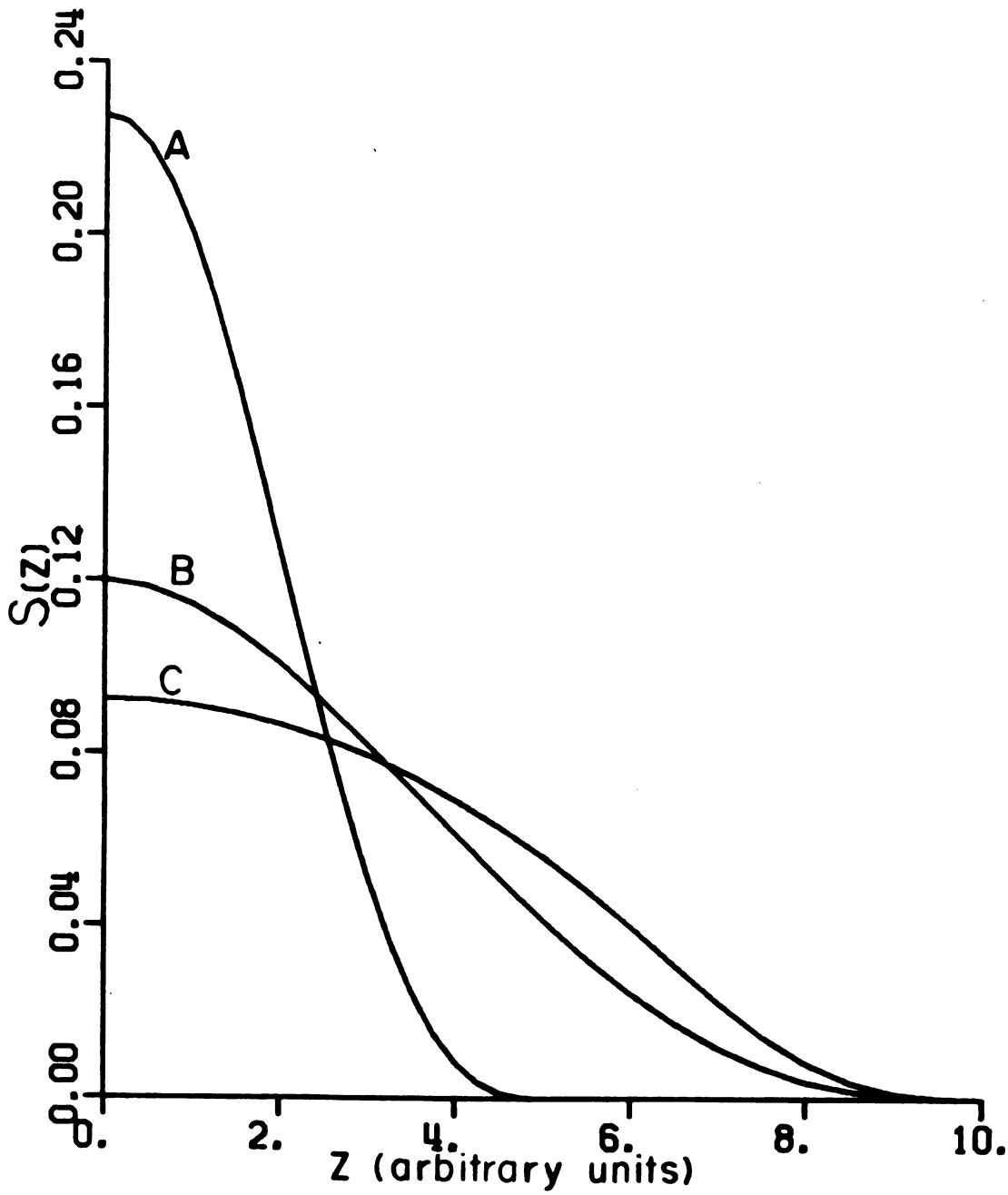

Figure G3: A plot of the function S(z) vs z.
Curve A: $\omega_1^0 = 3.0$ $\omega_2^0 = 2.0$
Curve B: $\omega_1^0 = 5.0$ $\omega_2^0 = 5.0$
Curve C: $\omega_1^0 = 8.0$ $\omega_2^0 = 2.0$

APPENDIX H: DERIVATIVES OF THE INTERATOMIC POTENTIAL

Presented here are analytical expressions for the first, second, and third derivatives of the pair potential $\phi(r)$ with respect to the interatomic spacing, obtained from the models of M-L-J (6-12) and B-P. These results derive from directly performing the algebra of differentiating the analytic form of the given model potential:

Mie--Lennard-Jones (6-12) potential:

$$\phi(r) = \varepsilon[(\sigma/r)^{12} - 2(\sigma/r)^{6}] \tag{H1a}$$

$$\phi'(r) = -12\varepsilon/r\ [(\sigma/r)^{12} - (\sigma/r)^{6}] \tag{H1b}$$

$$\phi''(r) = -\phi'/r + 72\varepsilon/r^2\ [2(\sigma/r)^{12} - (\sigma/r)^{6}] \tag{H1c}$$

$$\phi'''(r) = -\phi'/r^2 - 3\phi''/r - 432/r^3\ [4(\sigma/r)^{12} - (\sigma/r)^{6}]\varepsilon \tag{H1d}$$

Barker-Pompe potential:

$$\phi(r) = \varepsilon[e^{\alpha(1-r/\sigma)} \sum_{i=0}^{L} A_i\ (r/\sigma - 1)^i - \sum_{i=0}^{2} \frac{C_{2i+6}}{\delta+(r/\sigma)^{2i+6}}] \tag{H2a}$$

$$\phi'(r) = \varepsilon/\sigma\ [e^{\alpha(1-r/\sigma)} \sum_{i=0}^{L} A_i (r/\sigma - 1)^i (\frac{i}{(r/\sigma - 1)} - \alpha) + \sum_{i=0}^{2} \frac{C_{2i+6}(r/\sigma)^{2i+5}}{(\delta+(r/\sigma)^{2i+6})^2}] \tag{H2b}$$

$$\phi''(r) = \frac{\varepsilon}{\sigma^2}\{e^{\alpha(1-\frac{r}{\sigma})} \sum_{i=0}^{L} A_i (\frac{r}{\sigma}-1)^i [\alpha^2 - \frac{2i\alpha}{(\frac{r}{\sigma}-1)} + \frac{i(i-1)}{(\frac{r}{\sigma}-1)^2}] + \sum_{i=0}^{L} \frac{C_{2i+6}(2i+6)}{(\delta+(r/\sigma)^{2i+6})^2}[(2i+5)(\frac{r}{\sigma})^{2i+4} - \frac{2(2i+6)(r/\sigma)^{4i+10}}{\delta+(r/\sigma)^{2i+6}}]\} \tag{H2c}$$

$$\phi'''(r) = \frac{\varepsilon}{\sigma^3}\{e^{\alpha(1-\frac{r}{\sigma})} \sum_{i=0}^{L} A_i (\frac{r}{\sigma}-1)^i [-\alpha^3 + \frac{3i\alpha^2}{(\frac{r}{\sigma}-1)} - \frac{3i\alpha(i-1)}{(\frac{r}{\sigma}-1)^2} + \frac{i(i-1)(i-2)}{(r/\sigma-1)^3} + \sum_{i=0}^{2} \frac{C_{2i+6}(2i+6)}{(\delta+(r/\sigma)^{2i+6})^3}[\frac{6(2i+6)^2(r/\sigma)^{6i+15}}{\delta+(r/\sigma)^{2i+6}} - 6(2i+5)(2i+6)(\frac{r}{\sigma})^{4i+9} + (2i+5)(2i+4)(r/\sigma)^{2i+3}(\delta+(r/\sigma)^{2i+6})]\} \tag{H2d}$$

The triple-dipole potential function is written,

$$\phi_3(r_1,r_2,r_3) = \nu[z_1z_2z_3 + 3/8\ Z_1Z_2Z_3](z_1z_2z_3)^{-5/2} ,$$

where, for convenience, we have labeled the squares of the sides of the atomic triangle by z_1, z_2, and z_3. Here, the quantities Z_1, Z_2 and Z_3 are given by,

$$Z_1 = z_1 + z_2 - z_3$$

$$Z_2 = z_2 + z_3 - z_1$$

$$Z_3 = z_3 + z_1 - z_2$$

The analytic forms for the derivatives of ϕ_3 , to second order, are,

$$\phi_3^{(i)} \equiv \partial\phi_3/\partial z_i = -5/2\ \phi_3/z_i + \nu[z_jz_k+3/8\ (Z_i(Z_j-Z_k)+Z_jZ_k)](z_iz_jz_k)^{-5/2} ,$$

$$\phi_3^{(ij)} \equiv \partial^2\phi_3/\partial z_i\partial z_j = -5/2\ \phi_3^{(i)}/z_j - 5/2\ \phi_3^{(j)}/z_i - (5/2)^2\ \phi_3/z_iz_j + \nu[z_k + 3/4\ Z_i](z_iz_jz_k)^{-5/2} ,$$

and,

$$\phi_3^{(ii)} \equiv \partial^2\phi_3/\partial z_i^2 = -1/4\{\ 15\ \phi_3/z_i^2 + 20\ \phi_3^{(i)}/z_i - \nu 3[Z_j-Z_k-Z_i](z_iz_jz_k)^{-5/2}\}$$

In the above, i, j, and k each take on values 1, 2, or 3, and are in cyclic order.

LIST OF REFERENCES

LIST OF REFERENCES

1. R. J. Havlik in Ar, He and the Rare Gases, Gerhard Albert Cook ed., (Interscience Publishers, New York, 1961).

2. G. Boato, Cryogenics 4, 65 (1964).

3. B. L. Smith, Contemp. Phys. 11, 125 (1970).

4. G. L. Pollack, Rev. Mod. Phys. 41, 48 (1969).

5. G. L. Pollack, E. N. Farabaugh, J. Appl. Phys. 36, 513 (1965).

6. I. Lefkowitz, K. Kramer, M. A. Shields, G. L. Pollack, J. Appl. Phys. 38, 4867 (1967).

7. O. G. Peterson, D. N. Batchelder, R. O. Simmons, Phys. Rev. 150, 703 (1966).

8. W. B. Daniels, G. Shirane, B. C. Frazer, H. Umebayashi, J. A. Leake, Phys. Rev. Letters 18, 548 (1967).

9. D. J. Ball, J. A. Venables, Proc. Roy. Soc. Lond. 322, 331 (1971).

10. V. I. Grushko, D. N. Bol'shutkin, G. N. Shcherbakov, N. F. Shevchenko, Soviet Phys.-Crystallography 15, 536 (1970).

11. M. Gsänger, H. Egger, G. Fritsch, E. Lüscher, Z. Angew, Phys. 26, 334 (1969).

12. M. Beltrami, J. Appl. Phys. 33, 975 (1962).

13. E. R. Dobbs, G. O. Jones, Repts. Progr. Phys. 20, 516 (1957).

14. G. K. White and S. B. Woods, Phil. Mag. 3, 785 (1958).

15. I. N. Krupskii, V. G. Manzhelii, Phys. Stat. Sol. 24, K53 (1967) and Soviet Phys. JETP, 28, 1097 (1969).

16. A. Bernè, G. Boato, M. De Paz, Nuovo Cimen to 46, 182 (1969).

17. N. R. Werthamer, Am. J. Phys. 37, 763 (1969).

18. C. Kittel, Introduction to Solid State Physics, (John Wiley and Sons, Inc., New York, 1967).

19. R. E. Peierls, Quantum Theory of Solids, (Oxford University Press, New York, 1964).

20. P. Carruthers, Rev. Mod. Phys. 33, 92 (1961).

21. M. V. Bobetic, J. A. Barker, Phys. Rev. B2, 4169 (1970).

22. J. A. Barker, D. Henderson, W. R. Smith, Mol. Phys. 17, 579 (1969).

23. F. Clayton, D. N. Batchelder, J. Phys. C: Solid State Phys. 6, 1213 (1973).

24. W. R. Wheeler, Physics Today 25, 52 (1972).

25. C. S. Barrett, L. Meyer, J. Wasserman, J. Chem. Phys. 44, 998 (1966).

26. R. L. Parker, Solid State Physics, 25, page 152 (Academic Press, Inc., New York, 1970).

27. David Turnbull, Solid State Physics 3, page 225 (Academic Press, Inc. New York, 1956).

28. G. L. Pollack, H. P. Broida, J. Chem. Phys. 38, 2012 (1963).

29. H. G. van Bueren, Imperfections in Crystals, (North-Holland Publishing Co., Amsterdam, 1961).

30. C. W. Leming, Sublimation Pressures of Solid Argon, Krypton, and Xenon, Ph.D. Thesis, Michigan State University (1970).

31. Yu. S. Stroilov, A. V. Leonteva, D. N. Bolshutkin, et al., Sov. Phys. Solid State 15, 208 (1973).

32. D. Stansfield, Phil. Mag. 1, 934, (1956).

33. N. H. Macmillan, A. Kelly, Proc. R. Soc. Long. A330, 291 (1972).

34. A. J. Chapman, Heat Transfer (MacMillan Co., New York,

35. A. C. Rose-Innes, Low Temperature Techniques, (English University Press L.T.D., London, 1964).

36. R. E. Peterson, A. C. Anderson, Sol St. Comm. 10, 891 (1972).

37. R. E. Peierls, Ann. Phys. Leipzig 3, 1055, 1101 (1929).

38. P. G. Klemens in Thermal Conductivity 1, page 2, (Academic Press, New York, 1969).

39. G. Leibfried, E. Schlomann, Nachr. Akad. Wiss. Gottingen Math. Physik. Kl. 29, 71 (1954).

40. J. M. Ziman, Electrons and Phonons (Clarendon Press, Oxford, 1960).

41. I. Pomeranchuk, Zh. Eksp. Teor. Fiz. 11, 246 (1941) and Phys. Rev. 60, 820 (1941)

42. R. Berman, Contemp. Phys. 14, 101 (1973).

43. P. G. Klemens, Proc. Roy. Soc. Lond. A68, 1113 (1955).

44. K. Ohasi, J. Phys. Soc. Japan 24, 437 (1968).

45. R. L. Sproull, M. Moss, H. Weinstock, J. Appl. Phys. 30, 334 (1959).

46. M. Moss, J. Appl. Phys. 36, 3308 (1965).

47. A. Taylor, H. R. Alberts, R. O. Pohl, J. Appl. Phys. 36, 2270 (1965).

48. D. E. Daney, Cryogenics 11, 290 (1971).

50. P. G. Klemens in Solid State Physics 7 (Academic Press, New York, 1958).

51. A. Haug, Theoretical Solid State Physics 1 (Permagon Press, Oxford, New York, 1972), and others.

52. C. L. Julian, Phys. Rev. 137, A128 (1963).

53. B. I. Bennett, Sol. State Comm. 8, 65 (1970).

54. G. Niklasson, Phys. Kondens. Materie. 14, 138 (1972).

55. Yu. A. Logachev, B. Ya. Moizhes, A. S. Skal, Sov. Phys. Solid State 12, 2251 (1971).

56. D. B. Benin, Phys. Rev. Lett. 20, 1352, (1968).

57. J. A. Barker, A. Pompe, Australian J. Chem. 21, 1683 (1968).

58. J. A. Barker, R. A. Fisher, R. O. Watts, Mol. Phys. 21, 1803 (1971).

59. J. Ranninger, Ann. Phys. 45, 452 (1967).

60. J. A. Krumhansl, Proc. Phys. Soc. Lond. 85, 921 (1965).

61. G. K. Horton, Am. J. Phys. 36, 93 (1968).

62. B. M. Axilrod, E. Teller, J. Chem. Phys. 17, 1349 (1949).

63. J. Callaway, Phys. Rev. 113, 1046 (1959).

64. R. A. Guyer, J. A. Krumhansl, Phy. Rev. 148, 766 (1966).

65. M. Born, K. Huang, Dynamical Theory of Crystal Lattices, (Oxford University Press, New York, 1954).

66. R. J. Hardy, Phys. Rev. 132, 168 (1963).

67. A. A. Maradudin, Scientific Paper 63-129-103-P1 Westinghouse Research Lab., 1963 (unpublished).

68. L. M. Magid, Technical Report No. 3, Department of Electrical Engineering M.I.T., 1963 (unpublished).

69. C. Herring, Phys. Solid State 14, 2826 (1973).

70. G. L. Guthrie, Phys. Rev. 152, 801 (1966).

71. Yu. A. Logachev, M. S. Yur'ev, Sov. Phys. Solid State 14, 2826 (1973).

72. P. D. Thacher, Phys. Rev. 156, 975 (1967).

73. P. G. Klemens, Encyclopedia of Physics 14 S. Flügge, ed. (Springer-Verlag, Berline, 1956).

74. A. A. Maradudin, P. A. Flinn, R. A. Coldwell-Horsfall, Ann. Phys. 15, 360 (1961).

75. G. Leibfried, Handbuch der Physik 7 (Springer-Verlag, Berlin, 1955).

76. G. Gilat, G. Dolling, Phys. Lett. 8, 304 (1964).

77. W. M. Hartmann, FCC and BCC Lattices, Dept. of Phys. Michigan State University, (unpublished)

78. V. V. Goldman, G. K. Horton, T. H. Keil, M. L. Klein, J. Phys. C: Solid State Phys. 3, L33 (1970).

79. G. Gilat, Z. Kam, Phys. Rev. Lett. 22, 715 (1969).

80. F. W. De Wette, L. H. Fowler, B.R.A. Nijboer, Physica 54, 292 (1971).

81. N. R. Werthamer, Am. J. Phys. 37, 763 (1969).

82. R. W. Weir, L. Wynn Jones, J. S. Rowlinson, G. Saville, Trans. Faraday Soc. 63, 1320 (1967).

83. E. A. Guggenheim, M. L. McGlashan, Proc. Roy. Soc. Lond. A255, 456 (1960).

84. B. M. Axilrod, E. Teller, J. Chem. Phys. 11, 299 (1943).

85. M. E. Malinowski, A. C. Anderson, Phys. Letters 37A, 291 (1971).

86. This condition was originally stated in terms of $\tau^{-1} \propto T^n$, rather than $\tau^{-1} \propto q^n$. At low T, these are equivalent since expression of τ^{-1} in terms of the dimensionless variable $x=\hbar\omega/k_B T$ (which is integrated to essentially infinity at low T) results in $\tau^{-1} \propto x^n T^n$.

87. A. Granato, K. Lucke, J. Appl. Phys. 27, 583 (1956).

88. S. Ishioka, H. Suzuki, J. Phys. Soc. Japan 18, Suppl. II, 93 (1963).

89. A. Granato, Phys. Rev. 111, 740 (1958).

90. F.R.N. Nabarro, Proc. Roy. Soc. A209, 278 (1951).

91. H.G.G. Casimir, Physica 5, 495 (1938).

92. R. Berman, F. Simon, J. Ziman, Proc. Roy. Soc. Lond. A220, 171 (1953).

93. R. Berman, E. Foster, J. Ziman, Proc. Roy, Soc. Long. A231 130 (1955).

94. The computer gradient search routine used for this procedure was graciously provided by Dr. Peter Signell, Dept. of Phys., Michigan State University.

95. G. J. Keeler, D. N. Batchelder, J. Phys. C: Solid State Phys. 3, 510 (1970).

96. L. Finegold, N. E. Phillips, Phys. Rev. 177, 1383 (1969).

MICHIGAN STATE UNIVERSITY LIBRARIES
3 1293 03046 3560